

DYNAMIC ANALYSIS AND
MODELING OF AC/AC POWER
CONVERTERS FOR APPLICATIONS
TO SMART-GRID SOLUTIONS

ALEXANDROS KORDONIS

2015

**DYNAMIC ANALYSIS AND
MODELING OF AC/AC POWER
CONVERTERS FOR APPLICATIONS
TO SMART-GRID SOLUTIONS**

ALEXANDROS KORDONIS

MARCH 2015

Dedicated to my beloved parents and family

Σας αγαπώ πολύ

Scope and abstract

POWER electronics field is adapting rapidly to the needs of the new era of power systems which include smart-grid applications, renewable resources and so on. It is important for the consumer to be provided with different types of energy as for example alternate current or direct current ones. Therefore, energy conversion is one of the fundamental functions power system needs and it is mostly succeeded with the help of power transformers. The latter ones are mainly constituted by passive elements which are generally oversized but also inactive materials, therefore they can't provide active information for a better regulation. On the other hand, converters use power semiconductors which are controllable devices and as a result they can regulate voltage and current in a more efficient way. The major part of the power systems is controlled by AC voltage and so are the transformers throughout them. The motivation of this work is the replacement of these transformers by power electronics converters which are called AC/AC converters. As a result, we would like to show the potential and the advantages of these apparatuses for the future power systems through dynamic analysis, simulations, experiments, and prototype applications. Nonlinear techniques are also going to be used in our analysis in order to explain the benefits of operating in the edge of stability. An insight look at the contents of this dissertation follows.

Chapter 1 gives a small introduction about the main ideas that are going to be analyzed in this dissertation, those are AC/AC conversion, nonlinear dynamics, and power routers. Power router is a prototype device which can distribute on-demand power from the desired source to the desired load. By this way, we can achieve maximum operation of the renewable resources, constant power supply of the critical loads, and control localisation.

In the following Chapter 2, the fundamentals of a 1-phase buck type

AC/AC converter are analyzed. An open-loop control is confirmed both in simulations and experiments. One key factor of the converter operation is the switching frequency and one of the most important issues covered in this chapter would be the advantage of switching frequency. More specifically, operating in higher switching frequency makes the passive components be smaller in size. In addition, the harmonics tend to have smaller amplitudes so that it is easier to attenuate them. Moreover, during transient response the higher the switching frequency is the faster the decay time becomes and also there exist smaller in amplitude overshoots.

Closed-loop feedback control is considered in Chapter 3 by deriving a discrete time iterative map. The novelty lies on the applications of nonlinear dynamics through this model and the results cover a whole range of new operation regimes, which include period doubling operation and chaotic oscillations besides the conventional steady state. By this way, the switching harmonics are not gathering into high peaks as in the conventional steady state but instead, they are distributed into a wider area with smaller amplitudes (as the electromagnetic regulations also recommend). As a result, their elimination is an easy task. It will be shown that even during the chaotic operation the fundamental harmonic is maintained and it is the main responsible one for the power flow. The performance improvement of the converter operation is discussed again with simulated and experimental approach.

Three phase power systems are widespread and quite well established in the real world of power systems. Therefore, we were motivated to continue our research with a 3-phase AC/AC converter in Chapter 4. A matrix converter is chosen because it is quite a new converter but it is very promising for the actual realisation since it is a very compact device, with low harmonic content, without DC link since the direct topology is used and so on. Some fundamental control modulations are presented in the beginning and of course a dynamic model of it, too. The experimental and simulation results have good agreement and show the advantages of its operation. Efficiency can be increased if we exploit the resonances that are proven through the dynamic model. Transient behavior is also tested showing how the converter can respond to sudden scenarios such as voltage sags and frequency changes. Some drawbacks are also presented such as the inability of the control to reach the ideal voltage ratio limits. Finally, the switching frequency

has undesired effect on the efficiency since as the former is increasing the latter one is decreasing. These topics are left for future research since the final scope of this work is to present a possible application of the matrix converter.

Chapter 5 presents this application mentioned before. It is the combination of a matrix converter with a power router attached to its output. Different switching scenarios are tested and the experimental results show good agreement with the simulation ones. The purpose of this application is to show that there is great potential in the smart on-demand power supply by switching on and off the equivalent power sources according to the power the loads require.

Chapter 6 concludes this dissertation by summarizing the major points and achievements but also highlighting the future work and obstacles that should generate the motivation for further research.

Acknowledgements

IT wouldn't have been possible to complete this dissertation if it wasn't for the help, support and encouragement of many people around me all these years . All of them are equally important to me no matter how big or small their contribution was.

Let me start by thanking the one who accepted my ignorance, trusted me through time, accepted the cultural difference and supported me until the end of my Ph.D. diploma. My deepest gratitude to Professor Takashi Hikihara which has also given me the chance in the first place to join Kyoto University Ph.D. program, welcome me in the Hikihara-laboratory and last but not least gave me the chance to experience the magnificent Kyoto and Japanese culture. I wouldn't have reached until this point if there wasn't his wise guidance and careful supervision.

My sub-supervisors, Professor Tsunenobu Kimoto and Professor Tetsuji Matsuo who with their careful reading of my reports and their valuable comments throughout our conversations also supported me a lot for this work and helped it to be a more scientific and progressive one.

I would also like to thank all the laboratory members that have passed from my lab, especially Dr. Suketu Naik, Dr. Tsuguhiko Takuno, Dr. Masataka Minami, Mr. Takuro Oku, Mr. Tatsuya Yanagi, Mr. Keiji Tashiro, Mr. So Miyatake, Mr. Takashi Fumino, Mr. Yutaro Kitamori, Mr. Takuya Kajiyama, Mr. Hikaru Hoshino, Mr. Shinya Nawata, Mr. Kohei Nagaoka, Mr. Naoaki Fujii, and Mr. Daichi Nishihara for all their help in so many sectors such as research, theoretical or experimental suggestions, support, adaptation in Japan and so on.

Ms. Yoshiko Deguchi, Dr. Yoshihiko Susuki, Dr. Ryo Takahashi and Dr. Nobuo Satoh are the rest of the team to who I would like to give many thanks for their support and help. Furthermore, as for the financial sup-

port I should thank the Global CEO program of Kyoto University (GCOE), the Monbukagakusho scholarship of Ministry of Education, Culture, Science and Technology of Japan (MEXT), the financial support directly from the laboratory, and finally Rohm Co. Ltd. for the semiconductor providing.

Friends or lab-mates the following persons have undoubtedly earned a special place for this part of my life in Japan. Madoka Kubota has always been there from the beginning until the end helping and trying to answer whatever question I had. Atsushi Yao has also helped me a lot with various comments about research and has given me unforgettable experiences, too. Eileen Lu was the first foreigner coming in our lab after me and became a very good friend. Last but not least, I could not forget Yanzi Zhou and Fredrik Raak which made my life more colorful and spent much free time with me. To all the above I would like to say one big thank you and I hope we can once again meet each other.

My parents, Tasos and Sofia, have my cordial gratitude for supporting me to my crazy decisions, such as coming to a country right after a big natural disaster. I am very sorry for all the concerns and worries I have put you through. Words are not enough to describe my love towards you. My sister Maria and her family follow the list of my beloved persons which I would like to thank and also my older brother, Vassilis, along with my older sister Katerina and her family.

Last but not least, I would like to thank all the rest of my family, friends in Greece but also my new friends in Kyoto! May the God bless you and keep you always in good health and may all of your dreams come true. Many of my dreams came true here in Kyoto and that is why I thank all of you.

*Sincerely yours,
Alexandros Kordonis*

List of publications

THIS dissertation is partially fulfilling the requirements of Ph.D. diploma of the Department of Electrical Engineering of Kyoto University. Major divisions have been reproduced throughout this work from the following publication list. The author wishes no claim of copyrights from each and every one publication.

Journal articles

- Alexandros Kordonis, and Takashi Hikihara. "Harmonic Reduction and Chaotic Operation towards Application of AC/AC Converter with Feedback Control." *IEICE Transactions on Fundamentals of Electronics, Communications and Computer Sciences* 97, no. 3 (2014): 840-847.
- Alexandros Kordonis, and Takashi Hikihara. "Dynamic model of direct matrix converter and its experimental validation." *International Journal of Circuit Theory and Applications*, Wiley (under 2nd revision), 2014.
- Alexandros Kordonis, Ryo Takahashi, Daichi Nishihara, and Takashi Hikihara. "Three-Phase Power Router and its Operation with Matrix Converter toward Smart-Grid Applications." *Energies*, (submitted), 2014.

International conference proceedings

- Alexandros Kordonis, Ryo Takahashi, and Takashi Hikihara. "AC/AC converter towards power routing systems in smart-grids: Advantage on operation by nonlinear dynamics." *In Consumer Electronics (GCCE)*,

2013 IEEE 2nd Global Conference on, pp. 158-159. IEEE, Tokyo, Japan, October 2013.

- Alexandros Kordonis, and Takashi Hikiyara. "Direct Matrix Converter Space Vector Modulation and Dynamical Model Analysis towards Steady State Operation." *In Information Science, Electronics and Electrical Engineering (ISEE), 2014 IEEE 1st International Conference on*, vol.3, pp. 1629-1632, IEEE, Sapporo city, Japan, April 2014.
- Alexandros Kordonis, and Takashi Hikiyara. "Bifurcations and parameter sensitiveness during chaotic operation of ac/ac converter." *8th European Nonlinear Oscillations (ENOC)*, Vienna, Austria, July 2014.

Unarchived proceedings or technical reports

- Alexandros Kordonis, and Takashi Hikiyara. "High frequency switching ac/ac converter analysis towards application of SiC devices." *IEE-Japan Industry Applications Society Conference*, IEEJ, Tokyo, Japan, August 2012.
- Alexandros Kordonis, and Takashi Hikiyara. "Anomalous Oscillations in the Closed-Loop Feedback Control AC/AC converter." *Annual meeting of institute of electrical engineers of Japan*, IEEJ, Nagoya, Japan, March 2013.

Nomenclature

a^u :	voltage angle in dq0 reference frame
a^i :	current angle in dq0 reference frame
a_s :	output voltage angle
a_p :	input voltage angle
d :	instantaneous duty ratio
D :	steady state duty ratio
i_i :	input current
\dot{I}, \dot{V} :	phasors for equivalent currents and voltages
I_{sp} :	space vector for current
k :	feedback gain
n :	natural positive integers
N^+ :	set of all positive natural numbers
p, s :	index referring to the primary (secondary) side
q :	voltage ratio
s :	switching variable
t :	continuous time
T_s :	switching period
u_{in} :	input voltage
u_{im} :	amplitude of input voltage
u_1 :	voltage before output filter
u_o :	output voltage, capacitance voltage, voltage after the output filter
u_L :	voltage across the inductance
u, i, d :	state variables for nonlinear model
V_{ref} :	reference voltage
$V_{A,B,C}$:	idealistic input voltages
$V_{a,b,c}$:	idealistic output voltages
V_{sp} :	space vector for voltage
Z :	total impedance

Z_o :	combined impedance of capacitance and load
Λ :	Park transformation
ϕ :	power factor
ψ_{dq0} :	variable in dq0 reference frame
ω :	angular frequency of input voltage
ω_s :	angular switching frequency

Abbreviations

<i>A/D:</i>	analogue to digital
<i>BDS:</i>	bidirectional switch (or just SW)
<i>DPG:</i>	decentralized power generator
<i>EMC:</i>	electromagnetic compatibility
<i>FPGA:</i>	field programmable gate array
<i>LLE:</i>	largest Lyapunov exponent
<i>PCC:</i>	point of common coupling
<i>PET:</i>	power electronic transformer
<i>PLC:</i>	power line communication
<i>Si:</i>	Silicon
<i>SiC:</i>	Silicon Carbide
<i>SVM:</i>	space vector modulation
<i>THD:</i>	total harmonic distortion
<i>TISEAN:</i>	time series analysis
<i>VHDL:</i>	VHSIC hardware description language
<i>VHSIC:</i>	very high speed integrated circuit

Contents

List of Figures	xix
List of Tables	xxiii
1 Introduction	1
1.1 AC/AC conversion	1
1.2 Nonlinear dynamics	4
1.3 Power router	5
1.4 Purpose and outline	7
2 1-ϕ AC/AC Converter - Open Loop Control	11
2.1 Prologue	11
2.2 Fundamentals	11
2.2.1 Open-loop control	12
2.2.2 Equivalent circuit and harmonics	15
2.2.3 Phasor analysis	17
2.3 Simulation and experimental results	19
2.4 Switching frequency on transient response	23
2.5 Summary	26
3 1-ϕ AC/AC Converter - Closed Loop Control	29
3.1 Prologue	29
3.2 Output voltage feedback control	29
3.3 Nonlinear dynamic model	31
3.3.1 Off-state interval	32
3.3.2 On-state interval	32
3.4 Results and discussion	33
3.5 Summary	46

4	3-ϕ Matrix Converter	47
4.1	Prologue	47
4.2	Control modulations	47
4.2.1	Venturini modulation	48
4.2.2	Space vector modulation	49
4.3	Dynamic model	55
4.4	Results and discussion	59
4.5	Summary	66
5	Power Router 3-ϕ Switching	67
5.1	Prologue	67
5.2	Experimental layout	68
5.3	Experimental and simulation results	71
5.4	Summary and discussion	76
6	Conclusion	79
6.1	Attainments	79
6.2	Future work	80
	Appendix A Open loop 1-phase AC/AC converter	83
	Appendix B Pulses dead-time	85
	Appendix C Closed-loop feedback control	87
	Appendix D Iterative map	89
	Appendix E Space vector modulation	93
	Appendix F Matrix converter control	97
	Bibliography	101

List of Figures

1.1	Power density roadmap	2
1.2	Smart-grid layout	6
2.1	Bidirectional switch topology	12
2.2	1-phase AC/AC converter	13
2.3	Pulses generation with analogue circuit	14
2.4	Pulses generation simulation result	15
2.5	Equivalent circuit of AC/AC converter	17
2.6	Phasor diagram	18
2.7	Voltages and currents before and after the filter	20
2.8	Experimental result for voltages	21
2.9	Experimental result for voltages in R and RL	21
2.10	Experimental pulses	22
2.11	Experimental pulses detail	22
2.12	Harmonic content comparison	23
2.13	Transient topology	25
2.14	Transient response	25
2.15	Experimental transient during start-up	26
2.16	Experimental transient envelopes	26
3.1	Converter topology with ideal bidirectional switches	30
3.2	Control configuration of feedback regulator	31
3.3	Simulation result for steady state	34
3.4	Duty cycle comparison	34
3.5	Bifurcation diagram for gain	35
3.6	Bifurcation diagram details	36
3.7	Bifurcation diagram for duty cycle	37
3.8	Voltage and current iterative plots	37

3.9	Power spectrum	38
3.10	Nonlinearity density parameter space	39
3.11	Initial conditions test	40
3.12	Lyapunov exponent test	40
3.13	Experimental setup of 1-phase AC/AC converter	41
3.14	Experimental phase portraits	42
3.15	Experimental semi-periodic random oscillations	43
3.16	Duty cycle saturation	44
3.17	Semi-periodic oscillations spectrums	45
4.1	Matrix converter topology	48
4.2	Matrix converter switch topology	49
4.3	SVM space vector diagram	50
4.4	18 states graphically illustrated	53
4.5	Typical switching pattern	54
4.6	Simulation result for matrix converter steady state	59
4.7	Voltage ratio simulation comparison	60
4.8	Output voltage envelope	60
4.9	Efficiency versus voltage ratio	61
4.10	Efficiency versus line frequency	62
4.11	Voltage ratio versus line frequencies ratio	62
4.12	Phase plane during voltage sag	63
4.13	Transient during frequency change	63
4.14	Experimental pulses from FPGA and A/D converter	64
4.15	Voltage ratio comparison	65
4.16	Experimental result for efficiency	65
5.1	Generalized idea of matrix converter and power routers	68
5.2	Simplified circuit topology of matrix convert and power router	69
5.3	Experimental prototype power router	70
5.4	Experimental 3-phase source	71
5.5	Experimental 3-phase switching	72
5.6	Simulation verification of Fig. 5.5	72
5.7	Experimental switching with critical load	73
5.8	Simulation verification of Fig. 5.7	73
5.9	Experimental switching with two line switchings	74
5.10	Simulation verification of Fig. 5.9	74

5.11	Experimental switching for unbalanced sources	75
5.12	Experimental unified apparatus	76
6.1	Stability through chaos	80
6.2	Assembly of power electronic transformer	81
A.1	Open-loop experimental layout	84
B.1	Dead-time experimental implementation	86
B.2	Dead-time output result	86
C.1	Closed-loop feedback topologies	88
E.1	Three-dimensional representation	93
E.2	Switching state example 1	94
E.3	Switching state example 2	95
F.1	Low voltage 3-phase source implementation	98
F.2	Current sensor schematic	98
F.3	Signal multiplier	99
F.4	Optocoupler	99

List of Tables

2.1	Switching sequence for safe commutation	14
3.1	Experimental harmonic content	44
4.1	Matrix converter switching states	51
4.2	Switching sequences for SVM	52
4.3	21 switching states	54
4.4	Suffixes description for the dynamic model	57
5.1	Basic 3-phase switching scenario	69
A.1	Measurement instruments	84

1

Introduction

‘ Ἀγεωμέτρητος μηδεὶς εἰσὶτω — *Let no one destitute of geometry enter my doors* ’

– Plato (427 B.C. – 347 B.C.)

1.1 AC/AC conversion

Power electronics [1] is a field of electrical engineering which specializes in power conversion, control and reliability issues. This field combines control methods with power in order to achieve better power management and active control in the power-grid. The latter can undoubtedly be considered as one of the most complex systems humanity has ever created. Historically the first power device which could be controlled was the mercury-arc device [2] in the 30s, but the much more efficient thyristor appeared later on 60s [3]. The importance of power electronics wasn't very obvious; even three decades ago [4] the significance of power electronics was kept on emphasizing.

After the decade of 60s much research was done in the field of power electronics for DC and AC applications. Famous converters cover DC/DC [5, 6, 7], AC/AC [8, 9, 10], DC/AC [11, 12, 13], and AC/DC [14, 15, 16] conversion. In this work, AC conversion is studied both in 1-phase and 3-phase systems.

During the last decade, research on power electronics have been shifted towards high frequency switching [17]. Power electronics request high performance power devices as active switches. Nowadays, as Silicon has reached

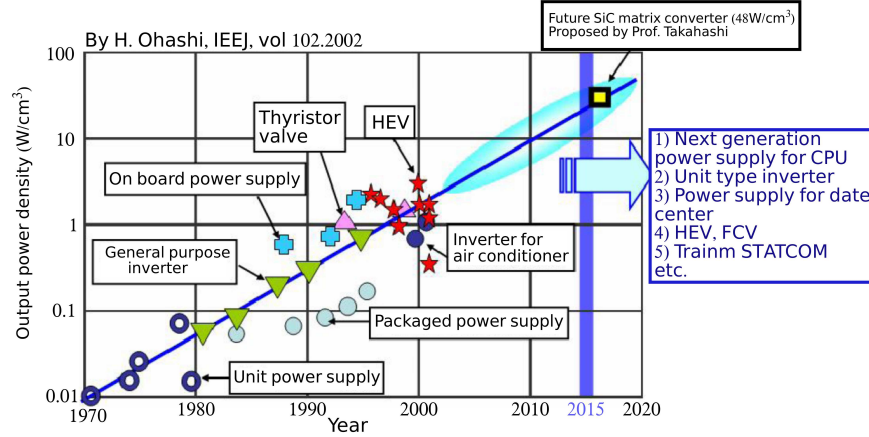


Figure 1.1: Roadmap of power density as presented in [18].

its theoretical limits, new wide-band gap semiconductors are strongly expected in the application phase. These new semiconductors bring attributes such as increased switching frequency, reliability, efficiency and so on. Silicon Carbide (SiC) MOSFET and JFET are such promising devices. An output power density roadmap for various power electronics converters is summarized in Fig. 1.1 as presented in [18]. It is obvious that the new power converters implemented with SiC devices will outdate the older ones by introducing new higher levels of power density.

As is often the case, several discussions have been made to compare the pros and cons of SiC devices, as in [19]. Up to now, extensive research has been made where the superiority of SiC has been variously proved [20, 21, 22]. Except of theoretical work, applications have been reported, as for example in [23] where it was shown that the inverter efficiency could be increased and still it would be cost-beneficial.

Increasing switching frequency will bring advantages as easy harmonic cancellation, decrease of the passive element volume, and smaller perturbation in output current. In addition, it will bring faster response in transient effects. On the other hand, the main disadvantage is that the device losses increase at high frequency. This is one of the reasons why SiC is introduced [20, 24, 25]. The advantages of SiC are plenty. Due to fast rise and fall times during switching and low on resistance, there is improved efficiency and inherent capability of high switching frequency. Lower capacitances and smaller packages are the results of high current density chips and smaller

die sizes. Large band gap energy improves radiation hardness, thermal conductivity, high temperature operation, and heat-sink miniaturization [26]. Advantages such as low chemical inertness, thermal stability, and ease of adaptation to hostile environments strengthen the opinion that SiC will actively contribute to the future low and medium voltage applications and will probably bring a new dimension to power conversion.

Disadvantages of SiC devices are also presented in [27] such as the base material costs which are more than 10 times bigger compared to Si ones. This fact results to higher chip costs at a given on-resistance. The compatibility is also limited in the chip manufacturing processes as far the wafer diameter and high temperature furnace are concerned.

This dissertation deals with AC/AC conversion and in particular with a 1-phase buck type converter as well as with a 3-phase direct matrix converter. The 1-phase converter is also known as PWM AC voltage converter and it is already known that this type of converter has superior characteristics compared to the lower quality phase-controlled one [28]. It can be used in static AC switches, soft starters, wind-turbine systems, lighting control, industrial heating systems, compensation of unbalanced supplies, and so on. From the view point of applications, it is obvious that its research field becomes wider and hasn't yet been fully investigated. Therefore, the dynamic model of this converter will be derived and the impact of high switching frequency will be investigated. To that end, SiC devices will be used in the equivalent experimental apparatus. Moreover, new operation regimes will be analyzed based on the nonlinear theory and the advantages such an operation could bring will be discussed.

On the other hand, more practical systems are the 3-phase ones. Therefore, the author considers the investigation of a 3-phase system is necessary. Such system should be the so called matrix converter. The basic configurations of a matrix converter are the direct and indirect one [29, 30]. The former will be investigated in this work because this configuration has no DC link making the overall system more simple and compact [29]. Moreover, a matrix converter can utilize four-quadrant bidirectional switches fact that allows high-frequency operation and bidirectional power flow. Operation with unity power factor for any load and energy regeneration is also possible. It can produce sinusoidal input/output currents and it can have a controllable power factor.

The literature topics around this converter are endless from the time it was introduced by M. Venturini and A. Alesina [31] until nowadays in applications for smart-grids [32] and photovoltaic power systems in remote areas [33] for better performance and lower harmonic distortion. Other research sides of this converter such as stability analysis [34], control design [35] and other issues [36, 37] have also been discussed. In this converter the superiority of SiC semiconductors makes also these converters to outperform the Si-based ones such as Silicon Carbide FET-based matrix converter [38] or Gallium Nitride-based one [39].

1.2 Nonlinear dynamics

Nonlinear phenomena exist all around us and they are actually the most predominant in the real world [40]. “In a chaotic system, using the laws of physics to make precise long-term predictions is impossible, even in theory. Making long-term predictions to any degree of precision at all would require giving the initial conditions to infinite precision” is characteristically mentioned in [41]. Nonlinear theory deals with such problems where uncertainty exists to an extent that the prediction of the trajectory is a difficult or impossible task. Quantitative and qualitative tools can be used instead for the description and partial solutions of these problems.

Nonlinear studies have already been done such as in simple RLC circuits with a nonlinear inductor whose core displays hysteresis and saturation [42, 43], sub-harmonic generation in a driven an-harmonic oscillator [44], of course in DC/DC converters [45, 46, 47, 48], in Chua’s nonlinear circuit [49, 50] and other experimental or numerical investigations [51, 52, 53].

Power electronics is also a field rich in nonlinear dynamics [54]. For many years researchers have also dealt with the problem of harmonic elimination as for example in [55, 56, 57, 58]. When designing a converter, the switching frequency, semiconductor choice, and control design must be well adjusted [35, 59, 60, 61]. All these parameters are creating nonlinear phenomena and they have to be taken into consideration, otherwise they may lead to fatal errors in the converter operation. Such phenomena are analyzed for various converters such as bifurcations in buck converters [62], nonlinear inductor modeling [63], and different applications during chaotic operation [64]. Complexity and diversity of the different regimes is outstanding in

this field of dynamics. Such complexity appears in strange attractors and Poincaré sections as in the DC/DC buck type converter analyzed in [54].

In the last decades the wide-spread frequency spectrums have been explored at specific operational regimes of system with switching, for example when it operates chaotically [65]. The power converter also has a possibility of the noise reduction by this method. Such behavior brings results with better EMC (Electro-Magnetic Compatibility) and improved agility [64, 66]. The EMC regulations request wide-band noise than narrow-band. Therefore it is of great importance if, for example, the switching harmonics could be spread in a wide frequency range with small amplitudes rather than having distinctive high peaks. By deriving discrete time models we are exploiting the advantages of this method in order to show the behavior of switching dynamics for AC/AC converters. Moreover, all the nonlinearities such as period doubling and chaotic operation are described through bifurcation diagrams and Lyapunov exponents. In other words, the qualitative and quantitative description of the nonlinear dynamics of the converter will help us explore and understand all these new operation regimes.

1.3 Power router

Nowadays, the target of power control tends to be decentralized [67, 68] and that is why we will consider a localized area where various power routers can be installed in every house or industry [69]. The main layout for a smart-grid community is shown in Fig. 1.2. The utility-grid is linked with the smart-grid through the point of common coupling (PCC). Various loads and decentralized power generators (DPG) are distributed throughout the smart-grid. Localized power management is desired and the introduction of power routers can succeed this smart-grid partitioning into smaller segments which will be named micro-grids. The red blocks represent these power routers which are scattered throughout the smart-grid. These power routers can distribute electrical power from the desired sources to the desired loads according to the power demand.

The initial stage of a power router has already been developed for DC applications [70] where the power is transferred on-demand from the desired source to the desired load. This is now expanded to include AC applications [67, 69] with circuit switching of two power lines and multiple routers in

both parallel and series configurations, i.e. an AC power routing network system can be created. The purpose of this project is to create a power network that can be readily adapted to the existing one, and can ultimately provide better regulation, distribution, and transmission of power. Power packet dispatching systems [71] and intelligent power switches [72, 73] have also been investigated for the purpose of improved power delivery. The feasibility of the power router requires further testing for practical applications; however, this study is aimed at demonstrating the feasibility of power router switching in 3-phase systems. Such a system is investigated in this work because 3-phase systems are commonly used in most of the power-grids.

The PCC is conventionally one bulk transformer which can transform

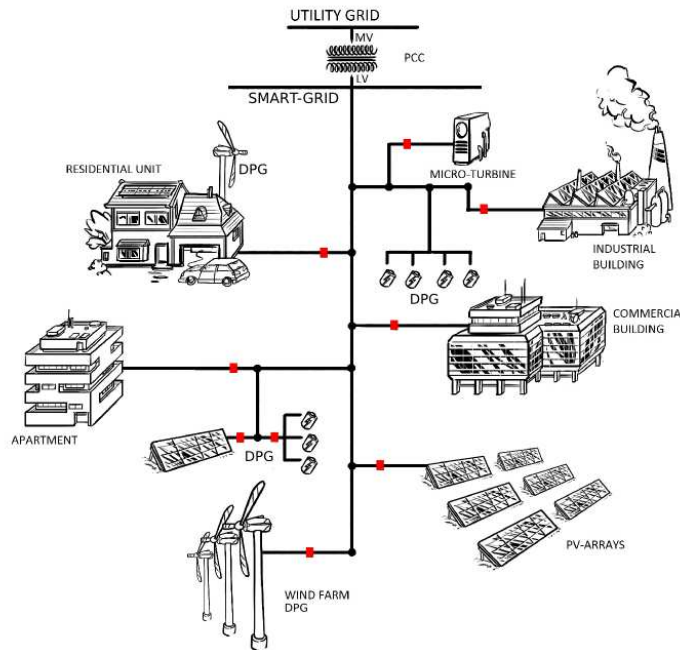


Figure 1.2: Power routers are distributed throughout the smart-grid (red blocks) partitioning it into smaller parts called micro-grids. The connection with the utility-grid is achieved in the point of common coupling (PCC). The conventional PCC (bulk transformer) will be replaced by power electronic transformer (PET) which is smaller and more effective than the conventional one. DPG refers to decentralized power generators and they can be wind generators, solar cells, batteries, electric vehicles etc.

the medium level voltage into low level one. This way is outdated since the introduction of power electronic transformer (PET) [74, 75]. PET can contribute to better regulation and control of bidirectional power flow between the utility and smart-grid. In particular, a possible PET assembly is two AC/AC matrix converters which create a high frequency link between them, where a compact electronic transformer is installed.

Matrix converter has the potential to be an essential part of the PET [76, 77]. One of the “great challenges” of the power systems as mentioned in [68] is the coordination between centralized and decentralized control. PET has the possibility of achieving this challenge since it implements power electronics devices that can easily function under control. Other great advantages of PET include reduction of the overall size and cost [78] by implementing high frequency operation.

1.4 Purpose and outline

Power electronics field is adapting rapidly to the needs of the new era of power systems which include smart-grid applications, renewable resources and so on. It is important for the consumer to be provided with different types of energy as for example alternate current or direct current ones. Therefore, energy conversion is one of the fundamental functions power system needs and it is mostly succeeded with the help of power transformers. The latter ones are mainly constituted by passive elements which are generally oversized but also inactive materials, therefore they can't provide active information for a better regulation. On the other hand, converters use power semiconductors which are controllable devices and as a result they can regulate voltage and current in a more efficient way. The major part of the power systems is controlled by AC voltage and so are the transformers throughout them. The motivation of this work is the replacement of these transformers by power electronics converters which are called AC/AC converters. As a result, we would like to show the potential and the advantages of these apparatuses for the future power systems through dynamical analysis, simulations, experiments, and prototype applications. Nonlinear techniques are also going to be used in our analysis in order to explain the benefits of operating in the edge of stability. An insight look at the contents of this dissertation follows.

Chapter 1 gave a small introduction about the main ideas that are going to be analyzed in this dissertation, those are AC/AC conversion, nonlinear dynamics, and power routers. Power router is a prototype device which can distribute on-demand power from the desired source to the desired load. By this way, we can achieve maximum operation of the renewable resources, constant power supply of the critical loads, and control localisation.

In the following Chapter 2, the fundamentals of a 1-phase buck type AC/AC converter are analyzed. An open-loop control is confirmed both in simulations and experiments. One key factor of the converter operation is the switching frequency and one of the most important issues covered in this chapter would be the advantage of switching frequency. More specifically, operating in higher switching frequency makes the passive components be smaller in size. In addition, the harmonics tend to have smaller amplitudes so that it is easier to attenuate them. Moreover, during transient response the higher the switching frequency is the faster the decay time becomes and also there exist smaller in amplitude overshoots.

Closed-loop feedback control is considered in Chapter 3 by deriving a discrete time iterative map. The novelty lies on the applications of nonlinear dynamics through this model and the results cover a whole range of new operation regimes, which include period doubling operation and chaotic oscillations besides the conventional steady state. By this way, the switching harmonics are not gathering into high peaks as in the conventional steady state but instead, they are distributed into a wider area with smaller amplitudes (as the electromagnetic regulations also recommend). As a result, their elimination is an easy task. It will be shown that even during the chaotic operation the fundamental harmonic is maintained and it is the main responsible one for the power flow. The performance improvement of the converter operation is discussed again with simulated and experimental approach.

Three phase power systems are widespread and quite well established in the real world of power systems. Therefore, we were motivated to continue our research with a 3-phase AC/AC converter in Chapter 4. A matrix converter is chosen because it is quite a new converter but it is very promising for the actual realisation since it is a very compact device, with low harmonic content, without DC link since the direct topology is used and so on. Some fundamental control modulations are presented in the beginning

and of course a dynamic model of it, too. The experimental and simulation results have good agreement and show the advantages of its operation. Efficiency can be increased if we exploit the resonances that are proven through the dynamic model. Transient behavior is also tested showing how the converter can respond to sudden scenarios such as voltage sags and frequency changes. Some drawbacks are also presented such as the inability of the control to reach the ideal voltage ratio limits. Finally, the switching frequency has undesired effect on the efficiency since as the former is increasing the latter one is decreasing. These topics are left for future research since the final scope of this work is to present a possible application of the matrix converter.

Chapter 5 presents this application mentioned before. It is the combination of a matrix converter with a power router attached to its output. Different switching scenarios are tested and the experimental results show good agreement with the simulation ones. The purpose of this application is to show that there is great potential in the smart on-demand power supply by switching on and off the equivalent power sources according to the power the loads require.

Chapter 6 concludes this dissertation by summarizing the major points and achievements but also highlighting the future work and obstacles that should generate the motivation for further research.

2

1- ϕ AC/AC Converter - Open Loop Control

‘ Ἐν οἷδα ὅτι οὐδὲν οἷδα — What I do not know I do not think I know ’

– Socrates (470 B.C. – 399 B.C.)

2.1 Prologue

Open-loop control and the fundamentals of a 1-phase AC/AC converter will give us the primary knowledge and motivations for further research in this dissertation. Simulation and experimental results will validate its operation and one of the most important parameters, the switching frequency, will be analyzed. The advantages and the converter potential will be discussed based on the results and a small conclusion will be given in the end of this chapter.

2.2 Fundamentals

In this section the fundamentals of the open-loop control 1- ϕ converter will be covered such as the control topology, bidirectional switch, equivalent circuit, harmonics, and phasor analysis.

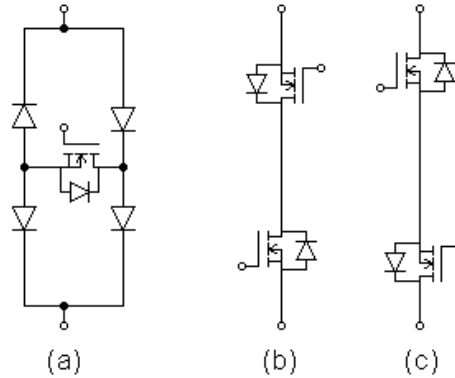


Figure 2.1: Bidirectional switch topology: (a) diode bridge topology, (b) common drain topology, (c) common source topology. The common source topology will be used due to its superiority to the other two ones.

2.2.1 Open-loop control

First of all, a bidirectional switch realisation is necessary in order to proceed with the converter construction. In simulations ideal switches are used; these switches can allow current to flow in both directions. On the other hand, the combination of more than one device can make a practical bidirectional switch. In Fig. 2.1 three typical types of such a switch are shown. Fig. 2.1 (a) shows the diode bridge bidirectional switch in which the overall device losses are relatively high since at every moment there are three conducting semiconductors. In Fig. 2.1 (b), the common drain topology is presented. Here, the problem is that two independent auxiliary power sources are necessary but in contrary Fig. 2.1 (c), shows the common source topology which requires just one auxiliary power source as it is confirmed in [79].

Since we are using the Fig. 2.1 (c) switch topology, the converter layout is shown in Fig. 2.2. It is a buck type converter with an LC filter in the output and an RL load. The input source V_{in} is a sinusoidal voltage source. The first bidirectional switch (BDS1) is used to allow the power flow to the load and vice versa in case our load is regenerative. BDS2 is responsible for the freewheeling current. A four-step switching strategy will be used as presented in [79] and is summarized in Table 2.1. The difference with the literature is that the output current detection is not needed but only the input voltage detection. That means, the switching sequence can be deduced

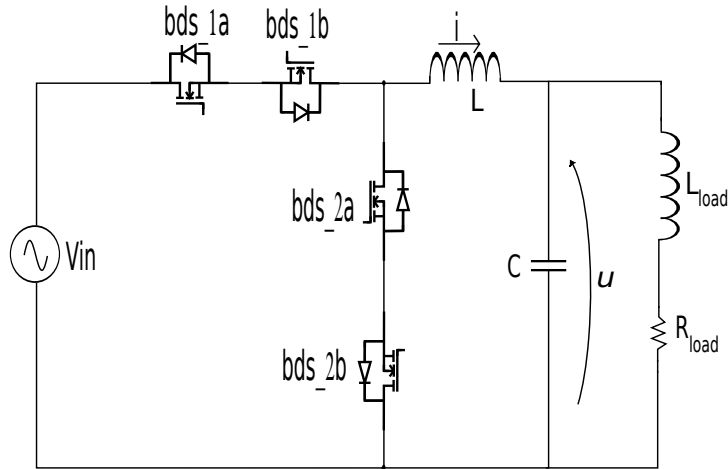


Figure 2.2: 1-phase AC/AC buck type converter topology. It consists of an ideal voltage source, two bidirectional switches, second order LC filter, and a generalized RL load.

only by the sign of input voltage. In each mode of the table, it is assumed that BDS2 is OFF and BDS1 is ON and opposite commutation is desired. When $V_{in} > 0$ it is assumed that the sign of the input voltage is positive and when $V_{in} < 0$ that it is negative.

By this switching sequence a safe commutation between the two switches can be succeeded. The triggering pulses lag each other by a minimum time difference Δt . This Δt has to be as minimum as possible in order to maximize the switching frequency but on the other hand it has to be long enough so to avoid overlapping which fact leads to short circuit effects and undesirable results. SiC MOSFET has almost perfect characteristics during its turn-off transient but during turn-on a high peak current transient effect takes place because of the diode reverse recovery. In order to avoid this high peak current and overlapping in general after examining the rising and fall times given by the manufacturer the worst case transient during the turn-on requires almost 90 nsec. Therefore, a Δt value at 90nsec can be considered commutation safe. Because of this fact, switching frequencies up to MHz range can be theoretically used.

There are several ways to realise such a control sequence. A simple fundamental method is by analogue circuits. Fig. 2.3 presents such an analogue way. By comparing triangular with step voltages and with the appropriate logic design the sequences for triggering the switches are generated. Due

Table 2.1: Switching sequence for safe commutation by measuring the sign of input voltage.

Switching sequence	Mode $V_{in} > 0$	Mode $V_{in} < 0$
Positive or negative current	Turn on BDS2b	Turn on BDS2a
	Turn off BDS1a	Turn off BDS1b
	Turn on BDS2a	Turn on BDS2b
	Turn off BDS1b	Turn off BDS1a
In the next switching cycle	Turn on BDS1b	Turn on BDS1a
	Turn off BDS2a	Turn off BDS2b
	Turn on BDS1a	Turn on BDS1b
	Turn off BDS2b	Turn off BDS2a

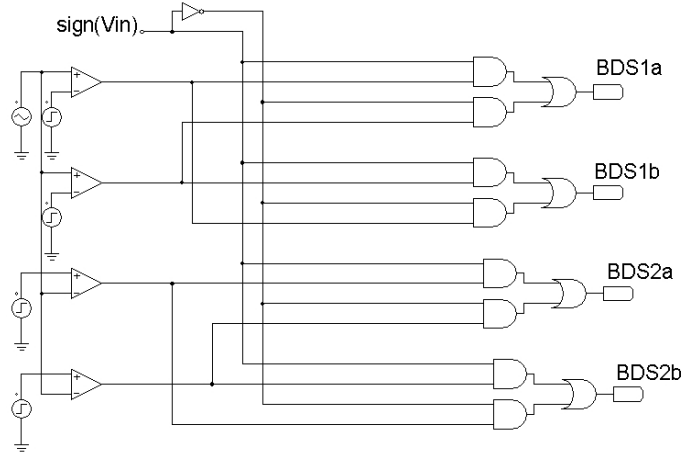


Figure 2.3: Pulses generation with analogue circuit. The triangular voltages can set the switching frequency as well as the duty cycle of the pulses.

to the fact that SiC MOSFET has a minimum Δt necessary for switching, increasing the frequency of the triangular voltage can increase the switching frequency of the two bidirectional switches. As a result, passive components energy storage requirement is getting reduced and the size of them, too. It should be noted that the converter is working as a classic buck type one. The output voltage will always be inferior to the input one. In this topology, a triangular voltage is compared with a step voltage and according to the offset of the triangular the duty cycle of the pulses is changing and the output voltage can be regulated, respectively.

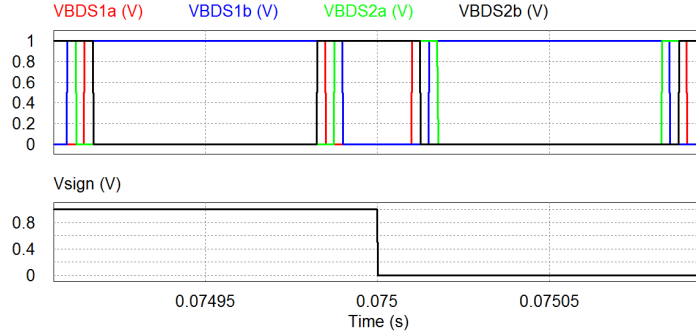


Figure 2.4: Simulation result for pulses based on Table 2.1. The sign of the input voltage is also shown at the moment it changes value.

Such an analogue approach is easy to be implemented in simulations but in the experiment is quite cumbersome. For that reason, digital methods are going to be implemented as we will see in later sections. The simulation result for the pulses can be shown in Fig. 2.4. The switching sequence of Table 2.1 can be confirmed.

2.2.2 Equivalent circuit and harmonics

We can assume the input voltage governed by Eq. (2.1) with u_{im} the maximum amplitude of the oscillation, and ω the input angular frequency. Right before the output filter the voltage, u_1 , takes the form of Eq. (2.2). Here it is considered that, when one bidirectional switch is ON, the other one is OFF and vice versa. If a switching pattern of the switches s is considered with duty ratio D and switching period T_s governed by Eq. (2.3), its Fourier transformation will have the form of Eq. (2.4), $n \in N^+$. Therefore the final result of u_1 will have the fundamental frequency and the upper sideband harmonics in multiples of switching frequency as in Eq. (2.5). ω_s refers to the angular switching frequency. In other words, it is proved that the harmonics exist on the switching frequency region and multiples of it. In Sec. 2.4 we will prove more advantages of high switching frequency.

$$u_{in} = u_{im} \sin(\omega t) \quad (2.1)$$

$$u_1 = \begin{cases} u_{\text{in}}, & \text{BDS1 is ON} \\ 0, & \text{BDS1 is OFF} \end{cases} \quad (2.2)$$

$$s(t) = \begin{cases} 1, & nT_s < t < (n+D)T_s \\ 0, & (n+D)T_s < t < (n+1)T_s \end{cases} \quad (2.3)$$

$$s(t) = D + \sum_{n=1}^{\infty} \frac{2 \sin(nD\pi)}{n\pi} \cos(n\omega_s t) \quad (2.4)$$

$$u_1 = s(t)u_{\text{in}}(t) = Du_{\text{in}} \sin(\omega t) + \sum_{n=1}^{\infty} \frac{u_{\text{in}} \sin(nD\pi)}{n\pi} \sin(n\omega_s \pm \omega)t \quad (2.5)$$

If we consider high switching frequency then it can be assumed that the inductance voltage u_L is constant in every switching cycle. In fact, it is either $u_{\text{in}} - u_o$ for $nT_s < t < (n+D)T_s$ or $-u_o$ for $(n+D)T_s < t < (n+1)T_s$, where u_o is the output voltage. Eq. (2.6) expresses the average equation of the inductance voltage. Also Eqs. (2.7) and (2.8) exist where i_i is the input current. Thus Eq. (2.9) which describes the equivalent circuit of Fig. 2.5 can be deduced. \dot{Z}_o is the parallel combination of the output load and filter capacitance. If we consider $Z = Z_o + j\omega L$ then $\dot{I}_L = D\dot{U}_{\text{in}}/\dot{Z}$.

$$u_L = D(u_{\text{in}} - u_o) - (1 - D)u_o = Du_{\text{in}} - u_o \quad (2.6)$$

$$u_L = L \frac{d}{dt} i_L(t) \quad (2.7)$$

$$i_i = D i_L \quad (2.8)$$

$$u_1 = Du_{\text{in}} \stackrel{(2.6)}{=} u_L + u_o \stackrel{(2.7)}{=} L \frac{d}{dt} i_L + u_o \quad (2.9)$$

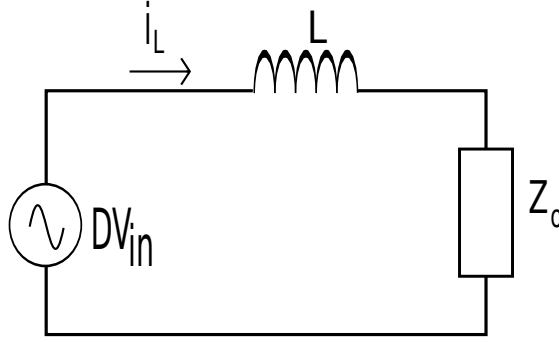


Figure 2.5: Equivalent circuit of AC/AC converter.

2.2.3 Phasor analysis

Phasor analysis will help us calculate the values of the passive elements. The input power factor can be calculated in Eq. (2.10) and also the output power factor by the Eq. (2.11). In Eq. (2.12) the angle of output voltage can be found if we assume as reference the input voltage. In our analysis we have assumed that there is no output capacitor in the beginning. This means that \dot{Z}_o consists only of R and L_o (assuming RL load) and \dot{Z} is found by adding the L of the filter. From the vector diagram we can find the output current angle with respect to the output voltage, output voltage angle with respect to input voltage and by assuming input power factor unity we can add the appropriate capacitance current. If we take as reference the angle of input voltage without harming the generality of the problem the vector diagram of Fig. 2.6 can be derived.

$$\phi_{\dot{I}_{in}} = \tan^{-1} \frac{\dot{I}_{in}}{\dot{V}_{in}} = \tan^{-1} \frac{D\dot{I}_1}{\frac{\dot{I}_1\dot{Z}}{D}} = \tan^{-1} \frac{D^2}{\dot{Z}} \quad (2.10)$$

$$\frac{\dot{I}_o}{\dot{V}_o} = \frac{1}{R + sL_o} \Rightarrow \phi_{\dot{I}_o} = -\tan^{-1} \omega \frac{L_o}{R} \quad (2.11)$$

$$\frac{\dot{V}_o}{\dot{V}_{in}} = \frac{D\dot{V}_o}{D\dot{V}_{in}} \iff \frac{D\dot{V}_o}{\dot{V}_L + \dot{Z}_o\dot{I}_L} = \frac{D(R + sL_o)}{R + s(L + L_o)} \quad (2.12)$$

$$\Rightarrow \phi_{\dot{V}_o} = \tan^{-1} \omega \frac{L_o}{R} - \tan^{-1} \omega \frac{L + L_o}{R}$$

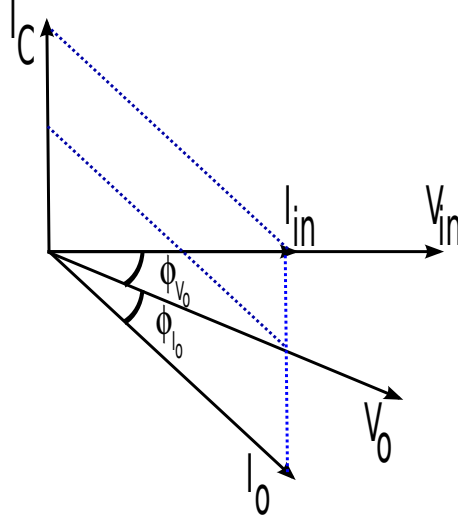


Figure 2.6: Phasor diagram. Capacitance value can be found from the phasor diagram and the equivalent power factors.

\dot{I}_{in} is the sum of \dot{I}_C and \dot{I}_o . But the inductance current is also governed by Eq. (2.8) which means there is a direct relation with the input current. By examining the phasors, C is found by current \dot{I}_C which is the sum of two imaginary smaller currents; there are two imaginary capacitances connected in parallel. In other words, by choosing the appropriate \dot{I}_C unity input power factor can be achieved. If the converter consumes active power P , the capacitance can be found as in Eq. (2.13). In addition, the inductance of the filter is derived by the desired ΔI_L and Eq. (2.14).

$$C = \frac{P(\tan(\phi_{I_o}) + \tan(\phi_{V_o}))}{\omega V_o^2} \quad (2.13)$$

$$L = \frac{(V_{in} - V_o)DT_s}{2\Delta I_L} \quad (2.14)$$

(a) Choosing the parameters :

If we are given a load of active power P and $\cos \phi$ is also known, R and

L can be found by the following substitutions:

$$\begin{aligned} R &= \frac{V_o^2 \cos \phi}{P} \\ L_o &= \frac{R \tan \phi}{2\pi 50}. \end{aligned} \quad (2.15)$$

As for the inductance of the filter it can be found assuming switching period T_s and desired ΔI_L as in Eq. (2.14). The next step would be to calculate the $\phi_{\dot{V}_o}$ from Eq. (2.12) and finally the capacitance C from Eq. (2.13).

(b) Numerical example :

Let's have a load 100 W with lagging power factor 0.9 which need output voltage 90 V at 50 Hz. The input voltage is 100 V and the switching frequency is 25 kHz:

From Eq. (2.15) $R= 72.9 \Omega$ and $L_o= 112 \text{ mH}$.

From Eq. (2.14) it can be found that $L= 18 \text{ mH}$.

Then from Eq. (2.12) the angle $\phi_{\dot{V}_o} = -0.7^\circ$, and finally Eq. (2.13) gives $C= 118 \mu\text{F}$.

In this example the load is 100 W with lagging power factor 0.9 at 90 V. The input voltage is 100 V so $D= 0.9$. That means that the load current is equal to 1.23 A. This current will pass through the bidirectional switch which consists of two semiconductors connected in series. Thus, semiconductors should withstand at least three times the values of input voltage and output currents, respectively. In other words, semiconductors with nominal values at 300 V and 4.5 A will fit for this converter. As far the dissipation power is concerned, the semiconductor should have more than 100 W in order not to require oversized heat-sinks since as it is already known oversized heat-sinks may cause radiation emission and act like a patch antenna [80]. Such issues about equivalent circuits and power factor analysis are also discussed in previous literature as in [81, 82]. In this section the fundamental analysis for the basic understanding of the AC/AC converter was covered.

2.3 Simulation and experimental results

The simulation results are shown in Fig. 2.7. The voltages and currents before and after the output filter are presented. It is obvious that the filter is necessary for the voltage harmonic elimination. On the other hand, the current is almost sinusoidal even before the filter. This is achieved by using

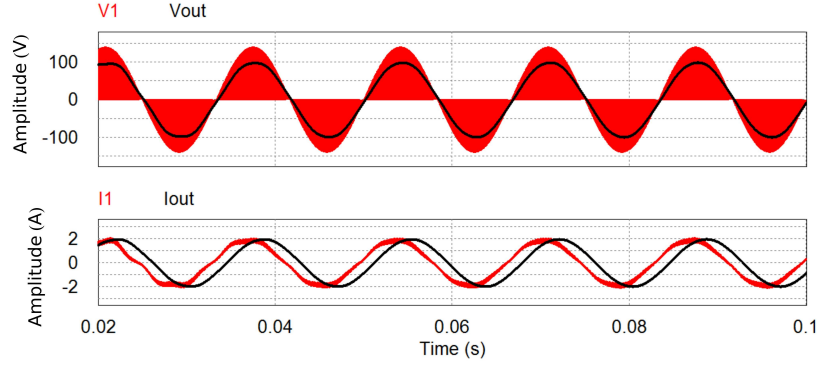


Figure 2.7: Simulation result for voltages and currents before and after the output filter.

high switching frequency as it will also be explained later.

As it was previously mentioned, the presented analogue approach is outdated and also cumbersome for the experimental realisation. Therefore, digital control with Field Programmable Gate Array (FPGA) is used. In the beginning, an isolation transformer is implemented in order to isolate the input voltage from the control part. Then the sign of the input voltage can be acquired through a voltage comparator (Appendix A). This signal with the appropriate voltage divider can produce the input signal for the FPGA. FPGA uses its internal clock to produce the four pulses for the Si N-MOSFETs (STW13NK100Z). But the output voltage levels of the FPGA are relatively low compared to the levels the semiconductors need. Therefore, drive circuits have to be used. ADuM1233 and Si8235 can make such operations (Appendix A).

The LC low pass filter has values of 0.45 mH and 33 μ F with a cutoff frequency at around 1.3 kHz. The load resistance is 100 W, 103 Ω . Two 20 mH, 5 A inductors connected in series have been used for a total inductance at 40 mH. The inductors were measured with the impedance analyzer and the result is that the total inductance varies from 40-80 mH. This variation is due to the magnetic flux saturation characteristics of the inductor core material [83]. Fig. 2.8 shows the equivalent result for the voltages before and after the output filter in the experiment. There is good agreement with the simulation results. Fig. 2.9 presents the output voltage measured only in the output resistance and in the whole RL, respectively. The lag because

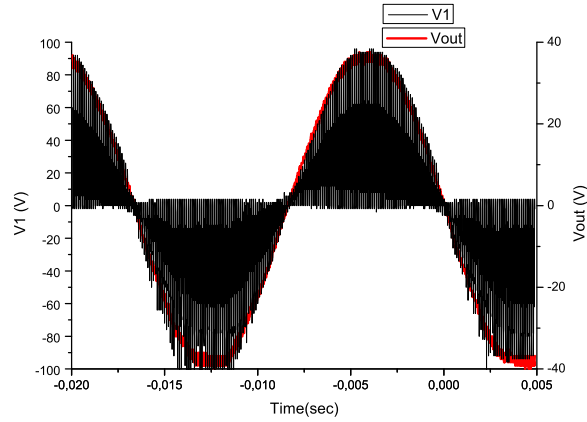


Figure 2.8: The voltage before the output filter contains several harmonics as it is also confirmed in this experimental measurement.

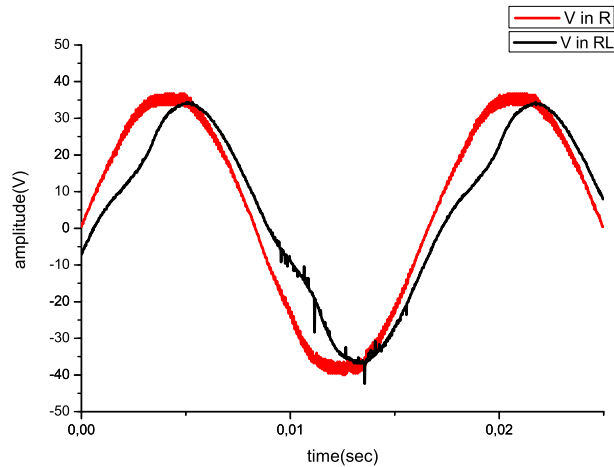


Figure 2.9: Experimental result for voltage measured only in R and in full RL load. When measured in full load the angle displacement is obvious as well as the harmonics due to the impedance fluctuation of the filter inductors.

of the inductance is obvious. It should be mentioned that the voltage in the whole RL carries some spikes and disturbance because the inductance has fluctuating value as it was previously noted. From these data the phase delay can be calculated between the two signals. The result is equal to 12.1° . We also can confirm this angle from Eq. (2.15). The equivalent result which

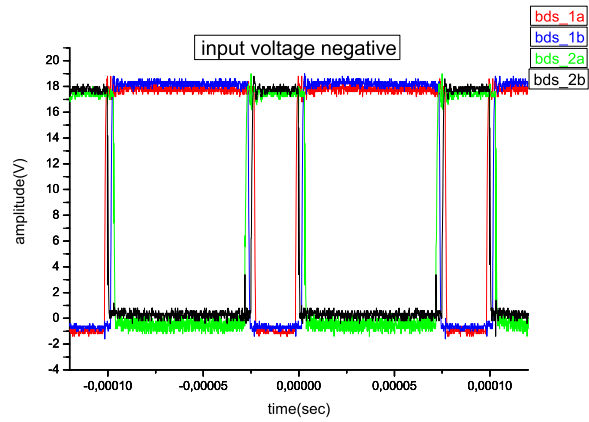


Figure 2.10: Four experimental pulses during negative sign of the input voltage. The sequence of Table 2.1 is obvious.

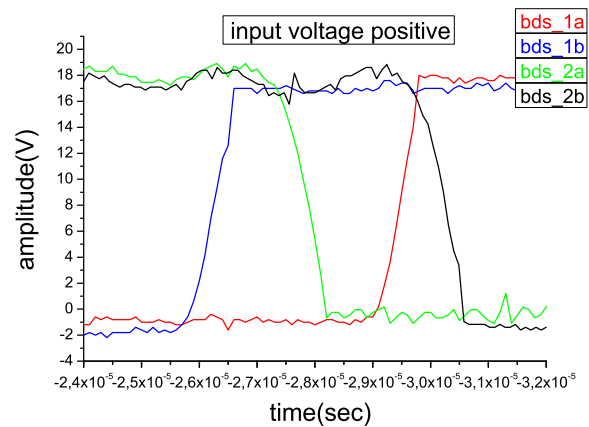


Figure 2.11: Detail of Fig. 2.10 commutation. The rise and fall times the semiconductors require for switching are also obvious in this time scale.

also shows good agreement with the experimental one is equal to 12.3° .

The experimental pulses of Fig. 2.10 are taken when the sign of the input voltage is negative. They follow the rules of Table 2.1 and they are in agreement with those of Fig. 2.4. The duty cycle in this particular test is 0.7. At every moment of switching every pulse lags from each other $1.6 \mu\text{sec}$ which is set easily by the FPGA VHDL code. A detail of the moment of switching is obvious on the following Fig. 2.11. This detail is during positive

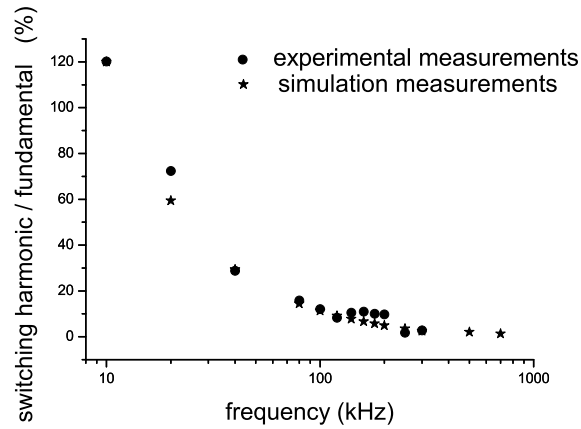


Figure 2.12: Switching harmonics are getting of smaller amplitude as switching frequency increases. Both experiment and simulation measurements show good agreement. The former ones are up to 250 kHz due to experimental limitations.

sign of the input voltage.

2.4 Switching frequency on transient response

The purpose of this section is to show how important the role of switching frequency is in the operation of the AC/AC converter during steady state but also in transient state. It is going to be proved that the elimination of harmonics is an easier task when operate in high switching frequency.

The overall result for the steady state is shown in Fig. 2.12. The vertical axis is the ratio of the biggest switching harmonic over the fundamental one. It is obvious that under this kind of operation the low switching frequencies offer big amplitude harmonics. Therefore, it will be of great importance if these harmonics could be spread to higher wide-band frequencies with lower amplitudes as we will see in the next chapter. It is worth mentioning here, that in the experimental results for switching frequencies higher of 80 kHz prototype Silicon Carbide T-MOSFETs are used since Silicon devices aren't capable to operate in these higher frequency regions.

Here, the case where the converter is without the LC filter is considered. This will make the calculations easier for this section but also it will show clearly the advantage of switching frequency. In this case the voltages and

currents before and after the output filter are the same. So we will refer only to the output voltage and current in this section. The voltage equation doesn't change and has the form of Eq. (2.5). If the dynamics of the circuit are considered we can easily find out that the output current is governed by Eq. (2.16). Solving for $g_1(t)$ will give the dominant harmonic in the line frequency. The solution $g_2(t)$ is the current harmonics which have the form of Eq. (2.17).

$$\frac{d}{dt}i_o + \frac{R}{L_o} = \frac{Du_{im} \sin(\omega t)}{L_o} + \sum_{n=1}^{\infty} \frac{u_{im} \sin(nD\pi)}{n\pi L_o} \sin(n\omega_s \pm \omega)t = g_1(t) + g_2(t) \quad (2.16)$$

$$i_o||_{g_2(t)} = \frac{\int \left\{ e^{\frac{R}{L_o}t} \left\{ \sum_{n=1}^{\infty} \frac{u_{im} \sin(nD\pi)}{n\pi L_o} \sin(n\omega_s \pm \omega)t \right\} \right\} dt}{e^{\frac{R}{L_o}t}} \quad (2.17)$$

$$i_o||_{g_2(t)} = \sum_{n=1}^{\infty} \frac{u_{im} \sin n\beta}{n\alpha\gamma} \frac{\sin(n\delta \pm \epsilon)t + \frac{1}{\alpha} \cos(n\delta \pm \epsilon)t}{1 + \frac{(n\delta \pm \epsilon)^2}{\alpha^2}} \quad (2.18)$$

If the following substitutions are performed: $\alpha = R/L_o$, $\beta = D\pi$, $\gamma = \pi L$, $\delta = \omega_s$, and $\epsilon = \omega$, the solution of Eq. (2.17) is Eq. (2.18). The amplitude of those signals is of the form $\frac{u_{im} \sin(n\beta)\alpha}{n\gamma(\alpha^2 + (n\delta)^2)}$ which requires the assumption $n\delta \gg \epsilon$ since the switching frequency is supposed to be much higher than the power line frequency. All the values are in a predictable value range since α and γ depend on the passive elements, β on the duty cycle, and δ on the switching frequency. Even by taking worst case scenarios for the RL load it is clear that as the switching frequency increases ($\omega_s = \delta$) the amplitude of the harmonic content is almost nullified. This is the theoretical proof of Fig. 2.12.

Figure 2.13 shows the simulation of a transient. The AC source has been replaced with an LC discharge and there is no output filter. In Fig. 2.14 the results for the output current are depicted for various switching frequencies. The red graph is for 20 kHz switching frequency while the blue one for 40 kHz and the black one for 80 kHz, respectively. It is clear that the transient decay time is much faster as the switching frequency increases. In the experimental approach, it is difficult to acquire two transients at the very same time in order to be compared to each other. Theoretically, we know that if these two transients happen at the same moment the one with the greater switching

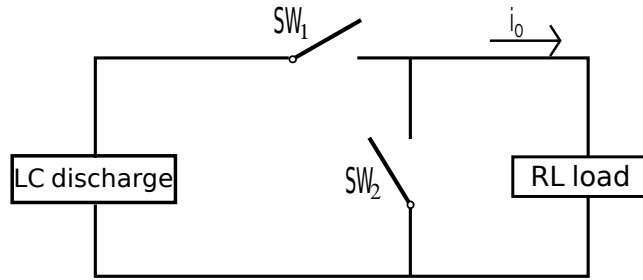


Figure 2.13: Transient topology. Instead of an AC source there is an LC discharge. The result of interest is the decay time of the measuring output current.

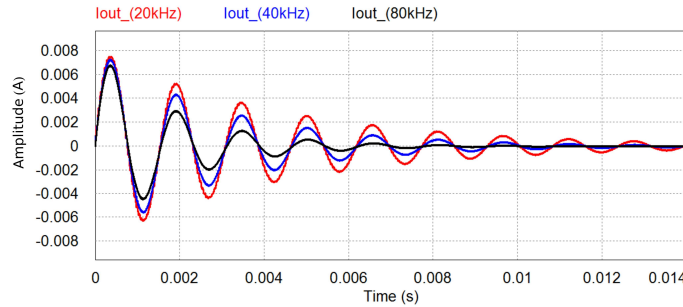


Figure 2.14: Transient response of LC discharge. As the switching frequency increases the decay time becomes smaller.

frequency would decay faster. In the experiment, the output current will be measured during the starting of the AC/AC converter. By this way, the transient response during the beginning of the converter operation will be investigated. An output filter has been used for the protection of the experimental parts. The current right before the output filter is measured. In Fig. 2.15 this current result is for 20 kHz and 10 kHz, respectively. The envelopes of the two transients are shown in the next Fig. 2.16. The two envelopes contain the impact of the sinus wave in them. But the transient of the lower switching frequency happens on a steeper region of the main sinus wave than the transient of the higher one. That means that the transient of the lower switching frequency contains already greater decay because of the sinus wave presence. But the two envelopes have almost the same decay. As a result it is obvious that the transient of the higher switching frequency would have succeeded greater decay if the two transients were at the same time.

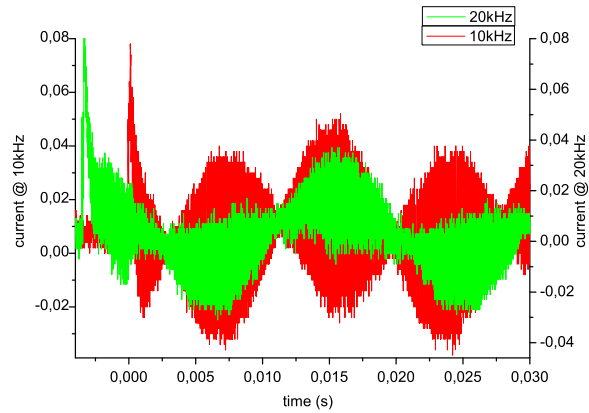


Figure 2.15: Experimental current measurement during transient of converter start-up.

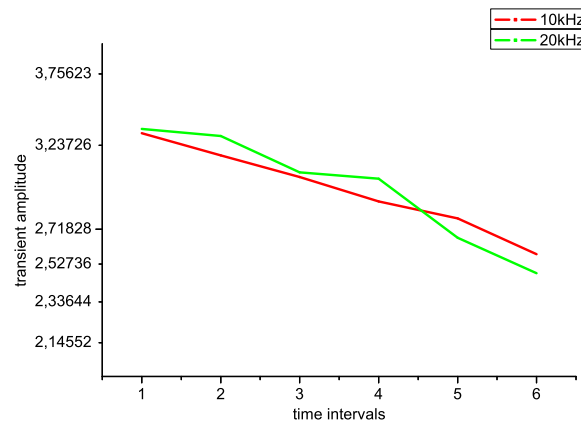


Figure 2.16: Envelopes of the two transients.

2.5 Summary

In this chapter the fundamentals about 1-phase AC/AC converter were covered. The open-loop control was explained both in simulations and experiments. The switching frequency was found to be one of the most important parameters including advantages as it increases such as faster transients, smaller in amplitude harmonics etc. Silicon devices on the other hand were unable to perform in high frequency regions because of their slow switching time capability. Therefore, Silicon Carbide devices were implemented. The

small-signal model of the AC/AC buck converter was found critically stable when it operates under open-loop control [84]. This was the motivation for us to proceed to a closed-loop control. In addition, the help of nonlinear dynamics will introduce new operation regimes in which the switching frequency harmonics can be spread into a wide range with lower amplitudes. That means, the novelty and the second motivation is how the harmonics could be decreased with the help of nonlinear dynamics, especially when these harmonics are of substantial amplitude as in the low frequency area of Fig. 2.12. All of the above will be analyzed in detail in the following chapter.

3

1- ϕ AC/AC Converter - Closed Loop Control

‘ Τῆς παιδείας αἱ μὲν ῥίζαι πικραί, οἱ δὲ καρποὶ γλυκεῖς — *The roots of education are bitter, but its fruits are sweet* ’

– Isocrates (436 B.C. – 338 B.C.)

3.1 Prologue

A nonlinear discrete time model of the AC/AC converter will be derived in this chapter. In order to achieve this goal, closed-loop feedback control must be implemented and in particular the output voltage will be monitored for the correct calculation of duty cycle. Through the numerical and experimental consideration the converter can operate in a chaotic motion and the advantages of the performance improvement are also discussed. Finally, a small summary will be given.

3.2 Output voltage feedback control

Closed-loop control is essential for a more stabilized converter operation. Fig. 3.1 presents again the topology of the converter with some additional simplifications. Instead of an RL load, a resistive one is going to be used. Moreover, the sequence of Table 2.1 is not going to be implemented but instead the same pulse will reach both the semiconductors of the bidirectional switches in every switching period. This is done for simplification purposes

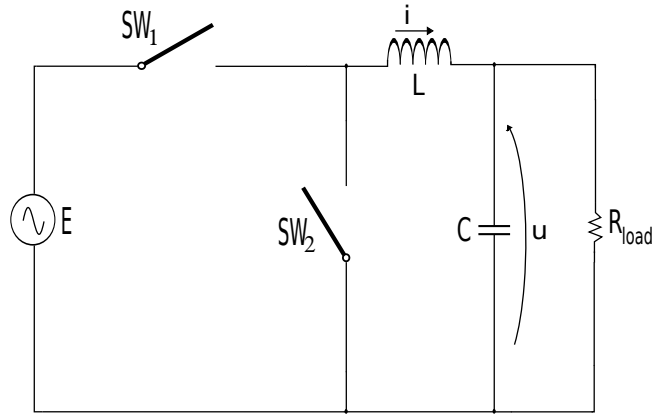


Figure 3.1: Converter topology with ideal bidirectional switches. The difference from the previous chapter is that here there is purely resistive load and dead-time has been implemented instead of the commutation of Table 2.1.

since attention should be paid to the feedback control. On the other hand, some dead-time has been added between the pulses for safety reasons and the equivalent circuit can be found in the Appendix B. We will refer only to the capacitance voltage, inductance current, and input voltage source which have the equivalent symbols (u , i , E).

The configuration of the proportional feedback control is illustrated at Fig. 3.2. D denotes the steady state duty cycle, k the feedback gain, V_{ref} the reference voltage and d the (instant) duty cycle. The output voltage is compared with the reference voltage and along with the feedback gain and steady state duty cycle, the instantaneous value of duty cycle can be decided. Then, this value should be limited between $[0, 1]$ so that the PWM pulses can be created which will be driven to the switches. Two experimental approaches have been tested, the analogue one and the dSpace-based one. These topologies are illustrated in Appendix C but they both follow the general rules of Fig. 3.2. Analogue approach is simple for implementation but not as flexible as the dSpace one. DSpace is an instrument that utilizes digital methods and cooperates with Matlab-Simulink models. Therefore, control modifications are faster and more precise. But since this method has frequency limitations due to its restricted internal clock the analogue approach is preferred.

In the next section, a discrete time iterative map is derived for the converter under investigation. This is an algebraically demanding process but

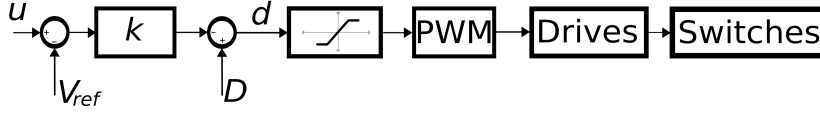


Figure 3.2: Control configuration of feedback regulator. The controllable parameters are the gain k and steady state duty cycle D .

the final iterative formula describes the cyclic operation between the different structural topologies of the converter (the on and off states of the switches create these different topologies) according to the equivalent duty cycle as described before. This repetition of the different circuit topologies is the main responsible factor that destroys the smoothness of the dynamics and causes nonlinear phenomena [85]. In other words, this structural change is the source of nonlinearity. Interesting phenomena and new operation regimes are discovered in the following but one section.

3.3 Nonlinear dynamic model

The converter presented in Fig. 3.1 obeys the unified differential equation system of Eq. (3.1). The state variables of the problem are the inductance current and capacitance voltage. The switching variable s represents the on-state at $s = 1$ and off-state at $s = 0$, respectively. The on-state represents the time duration when the source is feeding the load with power and the off-state when the freewheeling current flows through SW_2 . Based on the iterative map, the behavior from one to the next switching cycle will be described.

$$\begin{cases} L \frac{di}{dt} = sE - u \\ C \frac{du}{dt} = i - \frac{u}{R} \end{cases} \quad (3.1)$$

A complete switching period T_s happens every (t_n, t_{n+1}) , where $n \in \mathbb{N}^+$. Let $t_{n'}$ be the arbitrary moment the switching happens. Assume without harming the generality of the problem that SW_1 is off and SW_2 is on for $t_n \leq t < t_{n'}$ and vice versa for the rest of the switching period ($t_{n'} \leq t < t_{n+1}$). This equation system will be solved separately for both of the prementioned time intervals.

3.3.1 Off-state interval

- $s = 0, t_n \leq t < t_{n'}$:

This is called off-state. During this state, SW₁ is off and SW₂ is on. After solving the system of equations, for the $[t_n, t_{n'})$ interval, the result for the current and voltage will be:

$$\begin{cases} i_1(t) = f_1(u(t_n), i(t_n), (t - t_n)) \\ u_1(t) = f_2(u(t_n), i(t_n), (t - t_n)) \end{cases} \quad (3.2)$$

Now we set in the above equations:

$$t = t_{n'} \quad \& \quad t_{n'} - t_n = (1 - d)T_s$$

and the result becomes:

$$\begin{cases} i_1(t_{n'}) = f_1(u(t_n), i(t_n), ((1 - d)T_s)) \\ u_1(t_{n'}) = f_2(u(t_n), i(t_n), ((1 - d)T_s)) \end{cases} \quad (3.3)$$

The full equations for Eqs. (3.2) and (3.3) are presented analytically in the Appendix D.

3.3.2 On-state interval

- $s = 1, t_{n'} \leq t < t_{n+1}$:

This is called on-state. During this state, SW₁ is on and SW₂ is off. The system of equations, for the $[t_{n'}, t_{n+1})$ interval, results in:

$$\begin{cases} i_2(t) = g_1(u(t_{n'}), i(t_{n'}), (t - t_{n'})) \\ u_2(t) = g_2(u(t_{n'}), i(t_{n'}), (t - t_{n'})) \end{cases} \quad (3.4)$$

Now we set in the above equations:

$$t = t_{n+1} \quad \& \quad t_{n+1} - t_{n'} = dT_s$$

and the result becomes:

$$\begin{cases} i_2(t_{n+1}) = g_1(u(t_{n'}), i(t_{n'}), (dT_s)) \\ u_2(t_{n+1}) = g_2(u(t_{n'}), i(t_{n'}), (dT_s)) \end{cases} \quad (3.5)$$

The full equations for Eqs. (3.4) and (3.5) are presented analytically in the Appendix D.

The arbitrary switching time $t_{n'}$ is undesirable. Therefore, using Eq. (3.3) $t_{n'}$ can be eliminated in Eq. (3.5) and as a result the difference equation of the iterative map is created:

$$\begin{cases} i(t_{n+1}) = q_1(u(t_n), i(t_n), d) \\ u(t_{n+1}) = q_2(u(t_n), i(t_n), d) \end{cases} \quad (3.6)$$

The final iterative map is almost derived. In Eq. (3.6) the values of the next moment (t_{n+1}) are described according to the values of the previous moment (t_n) and the duty cycle d . The last equation needed is the one for the duty cycle itself and it is presented in Eq. 3.7 which can be derived directly from Fig. 3.2. In other words, d_n is not just a parameter but the third state of our problem. In the results section the change of the controllable parameters and what is their influence on the state variables of the problem will be discussed.

$$d_n = D - k(u_n - V_{\text{ref}}) \quad (3.7)$$

3.4 Results and discussion

As mentioned in the beginning, switching frequency is an important factor for every converter. Figure 3.3 shows the result of inductor's current in the steady state. The switching harmonics are multiples of the switching frequency with decaying amplitude as the order of switching frequency harmonic increases. The same behavior is observed in the experiment, too. It is also observed that, as the switching frequency increases, the current harmonics become smaller in amplitude. They can be easily attenuated since high frequency harmonics require smaller filters. But on the other hand, it would be of great importance if these harmonics could be spread to higher wide-band frequencies with lower amplitudes instead of using filters.

In addition, the duty cycle of the converter (d) follows the steady state duty cycle (D) with more accuracy when the switching frequency increases. In Fig. 3.4 the duty cycle is presented for two switching frequencies in the simulation and the experiment. It is clear that the deviation from the steady state duty cycle becomes smaller as the switching frequency increases. In detail, the steady state duty cycle was set to $D = 0.6$. The figure shows that at the lower switching frequency the duty cycle d follows D with greater

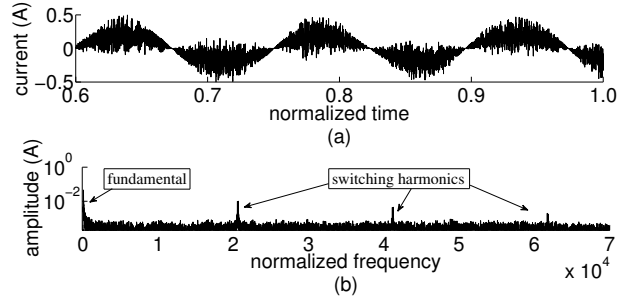


Figure 3.3: Current in steady state (a) and its frequency spectrum (b). Current contains the fundamental, switching harmonics and switching noise.

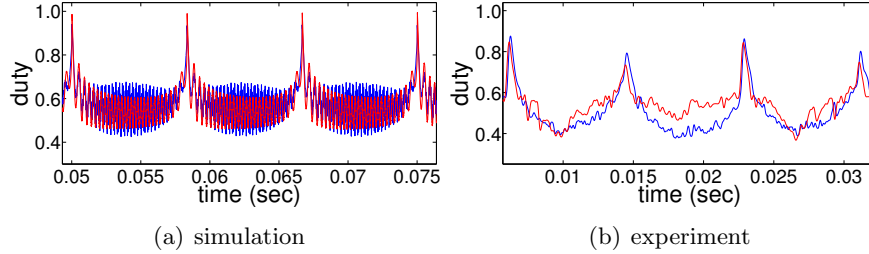


Figure 3.4: Duty cycle (d) follows more accurately the steady state duty cycle (D) in higher switching frequencies. Blue graph is for 15 kHz and the red one is for 50 kHz.

fluctuation. The two switching frequencies that were compared are 15 kHz and 50 kHz. They are denoted with the blue and red graph, respectively.

As the feedback of the converter is increasing interesting nonlinear phenomena appear. This operation is called chaotic operation and from now on it is going to be proved with qualitative and quantitative methods. This operation is desired in order to make sure that the output signal will follow the reference signal as precisely as possible [86]. It has already been proven [86] that high feedback operation brings advantages such as stability and performance agility. In this section, the particular points of high feedback operation in AC/AC conversion are going to be highlighted.

Figure 3.5 shows the dependence of one state variable versus the controllable parameter, which is the gain of the feedback control. Suppose that the steady state signal oscillates with the fundamental frequency within the interval $[-1, 1]$. A gain sweep is performed in order to make a bifurcation

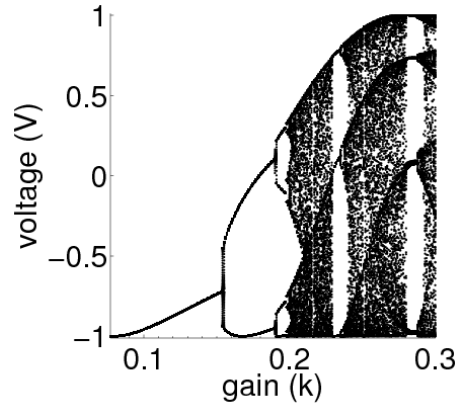


Figure 3.5: The dependence on the controllable parameter is qualitatively described by its bifurcation diagram. The complexity of dynamics is obvious in high gain regions.

diagram. In particular, each measurement in the bifurcation diagram is taken for every gain value from the equivalent time series around a very small time interval in the $n + 1$ switching cycle when the transient response remains until the n th cycle. In this data acquisition this small time interval corresponds to the condition that the signal has the maximum negative value -1 . For each gain value we gather the data at the peak. In the steady state all the data are almost near to -1 . This can be seen in the bifurcation diagram for the low gain values. As the diagram shows, increasing the gain value brings a period-1 solution until gain $k \approx 1.53E-1$. Then a series of period doubling bifurcations undergoes until gain reaches the value of around $2E-1$ where 4 chaotic bands exist which are merging into two and finally into one chaotic band bounded to the maximum limits. In fact, these bifurcations happen because of the topological sequence change in the converter. In every switching converter boundaries exist between continuous and discontinuous modes of operation as mentioned in [87]. In other words these non-smooth border-collision bifurcations occur because of the circuit structural alteration in every switching cycle. The gain sweep was selected between the region $[0.1, 0.3]$ because that is where the edge of stability exists. In low gain values, period-1 oscillation exists and at very high gain values instability occurs as it was expected.

Moreover, some windows of period-3 and period-4 periodicity are obvious. Some bifurcation veils are also visible declaring the regions where the

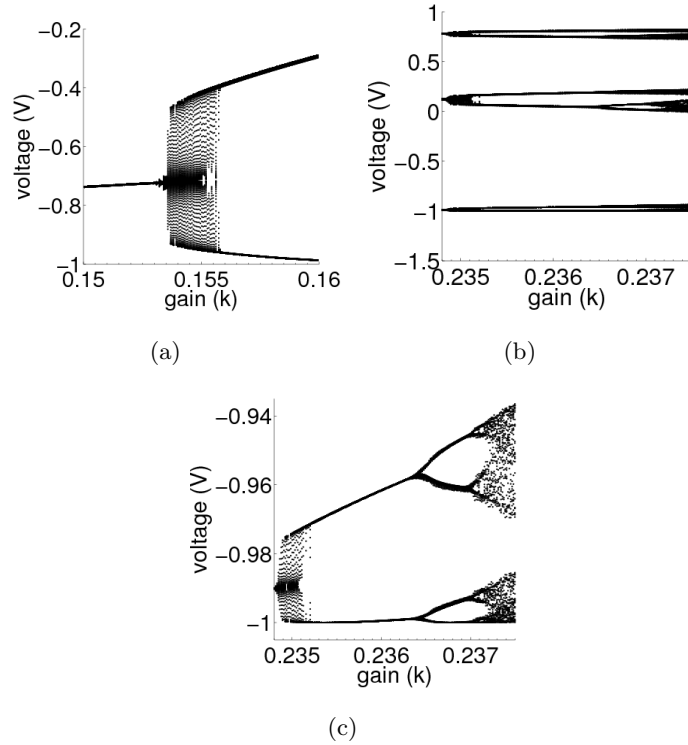


Figure 3.6: Bifurcation diagram details of Fig. 3.5. (a) is the detail from period-1 to period-2 oscillation. (b) is the period-3 window and (c) is the detail of its third branch. It is obvious that period doubling process takes place again here.

orbits are most probable. In other words, these solutions are more likely to happen during these particular operations. In Fig. 3.6 some details of Fig. 3.5 are presented. In Fig. 3.6 (a), the moment of change from period-1 to period-2 solution is zoomed. A quick small in amplitude turbulence is obvious during the transition between the two periodical orbits. Figure 3.6 (b) depicts the detail of the period-3 window of Fig. 3.5. One of the branches has been zoomed in order to depict the period doubling process better as in Fig. 3.6 (c). A bifurcation diagram if the gain is constant and the duty cycle (D) is changing is shown in Fig. 3.7. It is obvious that steady state period-1 oscillation appears periodically between the chaotic attractors as the duty cycle parameter is changing. By these diagrams, the mechanism that drives the operation of the converter from period-1 to multiple period operation to chaotic operation is isolated and described. In other words, here, the dy-

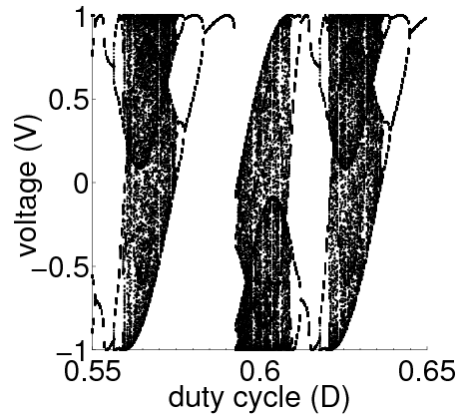


Figure 3.7: Bifurcation diagram for the other controllable parameter, steady state duty cycle (D).

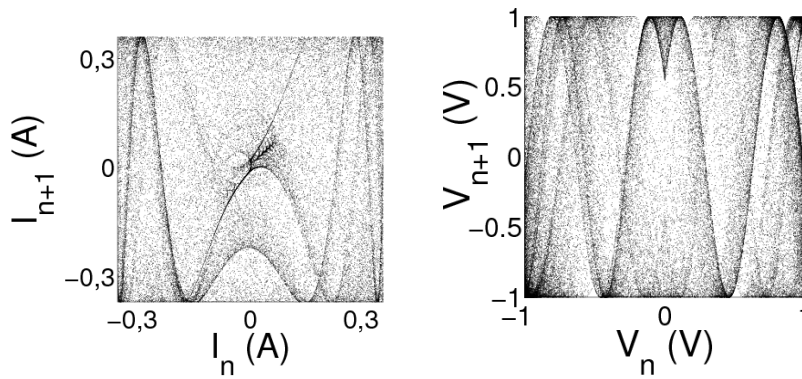


Figure 3.8: Iterative plots for current and voltage during the chaotic operation. The predominant frequencies form distinctive lines among the chaotic data.

dynamic system's dependence on the controllable parameters is qualitatively demonstrated. It should be mentioned that the RLC parameters used for the simulations are 50Ω , 0.45 mH , and $33 \mu\text{F}$ respectively. The qualitative description will not be enough when chaos has to be proven. Quantitative methods such as Lyapunov exponents and initial conditions tests have to be also performed as it will be shown in a few paragraphs.

In Fig. 3.8 the iterative plots of current and voltage are shown during these chaotic oscillations. The iterative plots cover all the area because of the random oscillations. They are unable to be connected into an orbit that

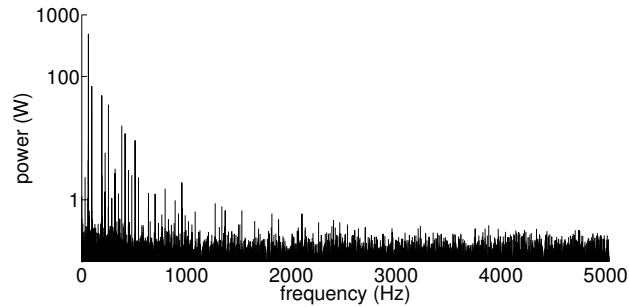


Figure 3.9: Responsible frequency for the power flow is mainly the fundamental one. Even the following biggest harmonic has five times smaller amplitude than the fundamental. Thus, it can be proved that even during the chaotic operation, a successful power flow can be possible.

closes itself but because of the predominant frequencies specific lines can be distinguished through these graphs. Despite the interesting demonstration of the iterative plots, they can't actually provide us with useful information about the converter operation. These lines of the iterative plots are formed mainly because of the fundamental frequency and this is proven by the power spectrum at Fig. 3.9. This spectrum is based on current and voltage of the prementioned iterative plots. It is clear that the level of wide-band noise is minimum compared to the fundamental and even the biggest harmonic is around five times smaller than the fundamental. Thus, an operation during which the fundamental frequency is responsible for the power flow is succeeded.

Steady state duty cycle (D) is also a controllable parameter which governs the change of steady state. Converters usually change their duty cycle when load is changing, some transient effect takes place etc. In Fig. 3.10 the different dynamical modes of the operation are geometrically plotted in the parameter space D and k . The "nonlinearity density" is presented via the coloring. It starts from the blue area which denotes the stable period-1 solution and goes until the brown one which is the chaotic region. The number of possible states is depicted via the discrete color-map. The middle stages, the period doubling process, aren't very clear since, as we described before, this is just a qualitative separation of the nonlinear regions. In detail, for every pair of (D , k) the simulation result is saved. Then, the higher number of periods the signal contains the closer to the brown color the equivalent area will be. Therefore, the most chaotic regions will have the brown color

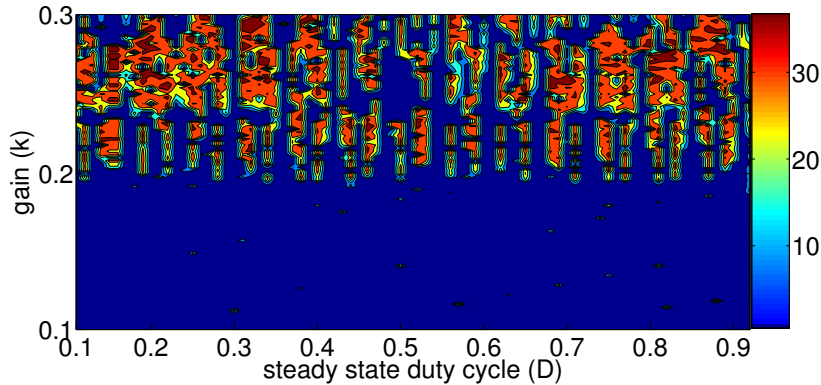


Figure 3.10: Nonlinearity effect into the parameter space. The most blue area is period-1 solution while the brown one is chaotic. Even at high gains, period-1 solution can be succeeded by fine-tuning D . These areas form stable period-1 “rivers” between the “islands” of chaotic operation.

and the period-1 solution will have the blue one. As a result this “nonlinearity density” can be determined. As it was expected in the low gain regions there are stable period operations and at high gains the complexity of the operation is increased dramatically. Another interesting observation is that although the high gain causes chaotic operation there are certain areas, let’s call them here “rivers”, where stable period operation can be succeeded. Even if the gain has to remain in high values, there is still possibility of stable operation along these “rivers”, meaning by fine adjustment of the steady state duty cycle. In addition, the period-3 window of Fig. 3.5 at gain $k \approx 0.24$ is also happening almost throughout the equivalent region of the parameter space. Figure 3.10 is a conspicuous description of the complex impact nonlinear dynamics can generate.

Fast and accurate control can switch appropriately to the optimised operation by moving along into the parameter space. This will bring tremendously great changes of the power converter concept. On one hand, moving along into the parameter space can bring a huge variety of operation regimes. On the other hand, even during the chaotic operation, the possibility to acquire the desired frequency exists within the chaotic data since the chaotic band contains a wide range of frequencies. This topic will be again discussed in the following paragraphs of this section.

One other test is the sensitiveness to the initial conditions. In Fig. 3.11 two time series are plotted together. The blue one is for zero initial condi-

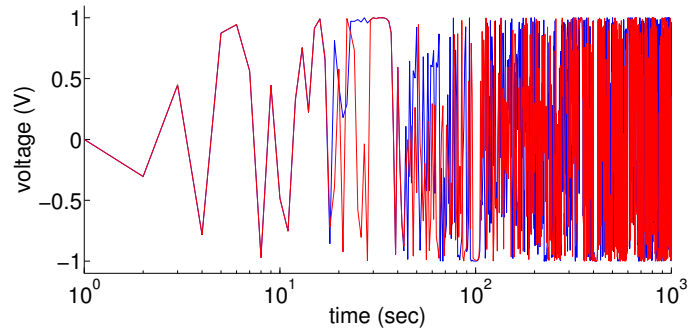


Figure 3.11: Voltage time series for two very close to each other initial conditions. After a short period of time the two trajectories are completely different.

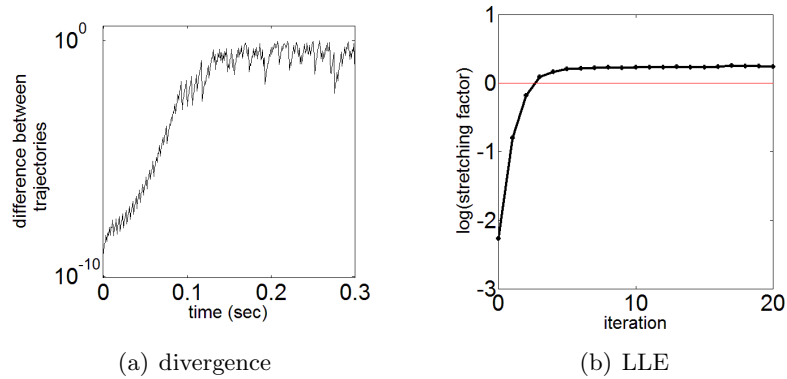


Figure 3.12: Left the exponential divergence from two initial conditions and right the calculation for the largest Lyapunov exponent. It can be found from the slope in the beginning of the figure.

tions and the red one is for slightly bigger ones ($1E-7$). The horizontal axis has a logarithmic scale in order to show the behavior more clearly. In the beginning, the two trajectories follow exactly the same path, soon one of them seems to lag the other. Finally, it is obvious that the trajectories are completely different, always bounded to the limits of the oscillation. This fact means that our system is sensitive to small differences of the initial conditions. This extreme “sensitivity to initial conditions” mathematically presented in various systems [41] has come to be called dynamical instability, or simply chaos. In Fig. 3.12 the divergence growth between those two trajectories is depicted on the left part of the figure. It can be noticed that

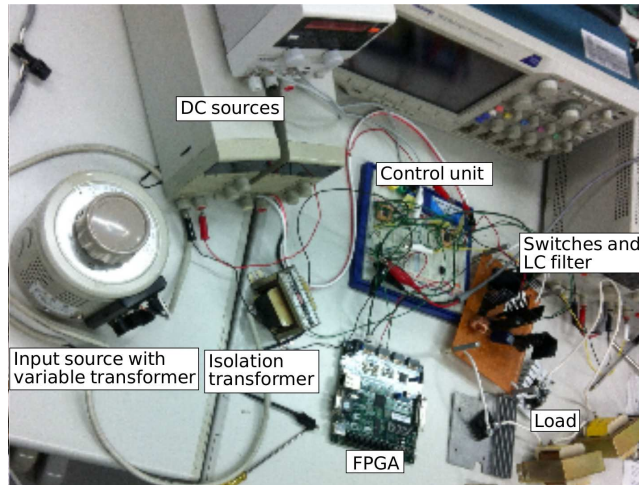


Figure 3.13: Experimental setup of 1-phase AC/AC converter.

the difference between the two orbits never converges to minimum again. The two time series, even bounded to the same limits, they are completely different to each other. The right part of Fig. 3.12 is the calculation of the largest Lyapunov exponent (LLE) of these chaotic time series. The first method to calculate the LLE is the Rosenstein algorithm [88] which is based on the reconstruction of the attractor dynamics from a single time series by embedding this time series into its embedded dimensional phase space, lagging a specific amount of time units. Only from the first few points we can take the LLE estimation since as the algorithm continues the data re-converge and the slope falls to zero. If the calculated slope is estimated in a least square sense the result for the LLE is 0.547. In order to verify more whether the result is chaotic or not the TISEAN [89] toolbox is used as well, giving a result of the LLE at 0.576. Although the two numbers are not exactly the same since different algorithms and procedures were implemented, it is verified that the LLE is a positive number giving the quantitative characteristics of our chaotic time series.

The practical side of all the above is that a converter can work in this chaotic region. With the proper control it will have a stable state and also the power flow will be concentrated to the fundamental frequency. In other words, the harmonic content will be at minimum levels. This will bring great advantages especially when the switching frequency should remain at low levels since according to Fig. 2.12 with the classical approach, the low

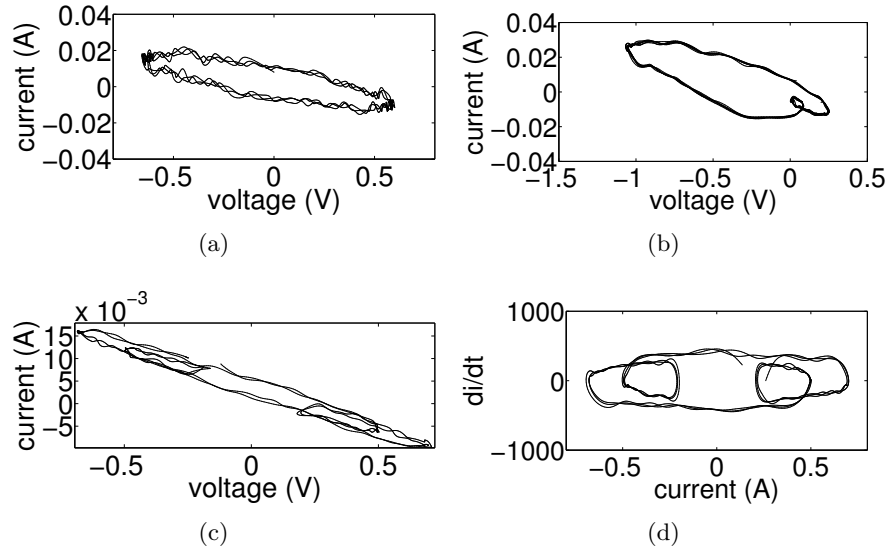


Figure 3.14: Experimental phase portraits. Steady state is observed in (a) with the main circle representing the base line frequency and the curly behavior because of the switching frequency. Period-2 solution at (b) and period-3 at (c). (d) shows clearly the period-3 by plotting the current versus its derivative. Period-3 has higher order harmonics and reduced overall amplitude than period-2.

switching frequencies bring great amount of harmonics. Instead, chaotic operation along with suitable control could fix the prementioned problem. Therefore, a wider range of operation arises for fast-response and more agile power AC/AC converters.

Figure 3.13 shows a photograph of the experimental setup. In this topology the isolation transformer is shown which is used for the measurement of input voltage in Chapter 1. In this chapter it is replaced by the measurement of output voltage. In Fig. 3.14 experimental phase portraits are presented. In Fig. 3.14(a) the circle depicts the base frequency (fundamental) and the curly behavior is caused by the switching impact. RLC parameters are the same as in simulations. The data have been averaged in order to have a better view but there is a small loss of amplitude information. The feedback gain was set at 0.1. In Fig. 3.14(b) there is a small extra circle in the phase portrait when the gain was increased at 0.13. From the data analysis it is found that there is also the 2nd harmonic except for the fundamental and switching harmonics. Thus, the converter is driven to

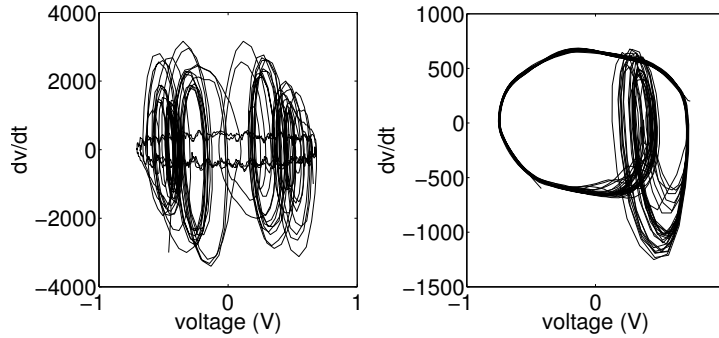


Figure 3.15: Semi-periodic random oscillations in experiment. The right one is called unilateral semi-periodic solution because the randomness happens in one side of the main circle path when the gain k was set at 0.25. The left one is called bilateral (or multilateral) because the extra periods are all over the fundamental circle ($k=0.3$).

a period-2 operation. Moreover at $k=0.17$ a period-3 operation appears as it is shown in Fig. 3.14(c). The graph for the current against the derivative of the current is also plotted in Fig. 3.14(d) in order to show more clearly this operation. The analogue control approach as described in Appendix C was implemented. There is a small discrepancy with the simulation results which may be due to the fact that in the simulations parasitic effects and resistances from the semiconductors haven't been taken under consideration.

Two important phase portraits are shown in Fig. 3.15. They were succeeded in higher gain regions and it was noticed that semi-periodic random oscillations occurred. The left subfigure presents bilateral random oscillations in unexpected moments while in the right one there is a specific time in every cycle during which there is a different period every time and therefore it makes a unilateral semi-periodicity. This might happen because of grazing phenomena [86] driving the operation to a multi-period solution. It is worth noting that in the bilateral solution, duty cycle saturation was noticed fact that origins from nonlinearity. This duty cycle saturating nonlinearity was observed in the simulations, too. This fact ensures the border collision case since such kind of nonlinearity is also one of the basic causes for border collision bifurcations. The example of duty cycle saturation is shown in Fig. 3.16. The duty cycle has a wide range of values and also it oscillates randomly at some moments. The steady state duty cycle (D) is different between the numerical (Fig. 3.16 (a)) and experimental (Fig.

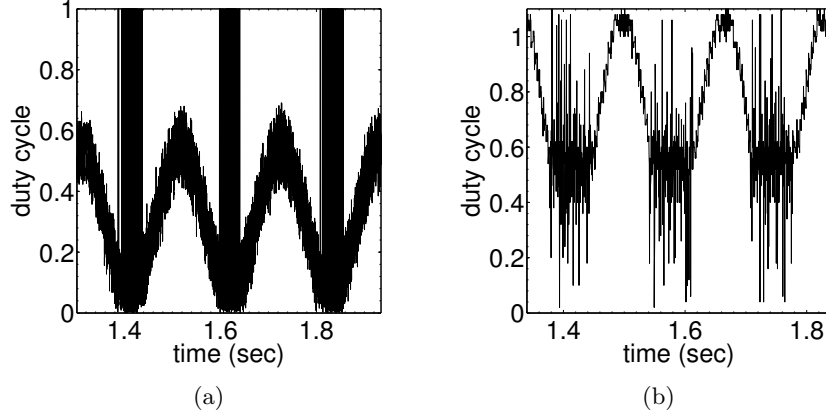


Figure 3.16: Duty cycle saturation for experiment and numerical trials. Duty cycle oscillates randomly and it also takes a wide range of values.

Table 3.1: Harmonics amplitudes during period-2 and 3 (% of the fundamental). Higher order semi-periodic solutions were also observed (unilateral and bilateral). At higher periods, shifting to higher harmonic orders and lower amplitudes is expected. The semi-periodic random solutions have smaller harmonic amplitudes except the third harmonic in the bilateral solution.

Period No.	2nd	3rd	4th	5th
2	52.7%	14.7%	11.6%	7.6%
3	0%	43%	0%	10%
unilateral	13.4%	11.1%	9.1%	8.1%
bilateral	9%	65.5%	11.1%	8.7%

3.16 (b)) results but the inability to keep a normal operation as well as the saturation can be confirmed in both trials.

At period-2 and 3 operations it is the lower harmonics that cause this behavior. In the chaotic oscillations of the numerical results there is a broadband spectrum. In other words there are many frequencies contained in the signal. In [64] there is a comparison of a comb-like spectrum and a broadband chaotic spectrum. It was concluded that the broadband spectrum brought a significant reduction of harmonics in the converter operation.

In our work, period-2 operation contains the 2nd harmonic with 52.7% the amplitude of the fundamental, 3rd one with 14.7%, 4th one with 11.6% and 5th one with 7.6%. These numbers along with period-3 orbit and the semi-periodic oscillations are summarized in Table 3.1. In just one higher

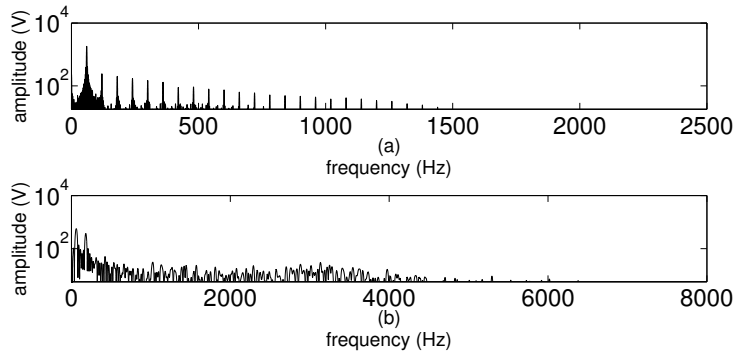


Figure 3.17: (a) Unilateral solution spectrum and (b) bilateral solution spectrum. In the bilateral solution there is a more wide and without spikes spectrum. Every harmonic greater than 1% of the fundamental amplitude is shown.

order of period- n operation, an amplitude reduction of the harmonics is achieved and also the main harmonics are shifted to higher orders. If the inverses of harmonic orders are used as weights a 64.22% harmonic reduction is estimated between period-2 and 3 operations. The unilateral semi-periodic solution appears a reduction of harmonics at 68.69% and the bilateral semi-periodic one is at 32.44% compared with period-2 solution. The double-sided semi-periodic one has an evenly distributed harmonic spectrum and only the third harmonic has quite increased amplitude. If this main harmonic is not considered, like in 3-phase circuits which will be discussed in the next chapter, the sum of all the others is estimated less than 10% of harmonic contribution compared always with the period-2 solution. Therefore, there is a tendency of suppressing the low order and switching harmonics into a wide frequency area. Another approach to understand more the semi-periodic solutions is the frequency spectrums presented in Fig. 3.17. Figure 3.17 (a) is for the unilateral solution and (b) for the bilateral one. The limits for the vertical axis have been set in such a way that only the greater harmonics of 1% of fundamental amplitude are shown. It is obvious that in the bilateral solution spectrum there is a much more broadband spectrum than the unilateral one and it is smoother, too. A final remark of the random oscillations is about their total harmonic distortion (THD). The unilateral solution has a THD equal to 4.9% while the bilateral's one is 4.3% without taking under consideration the third harmonic. These values meet the overall standards

set by IEEE std. 519 – 1992. Applications and simple examples of these standards can be found in [90].

The problems of analogue approach made the period doubling operation data acquisition more difficult. Extreme caution must be paid also to the controllable parameters since as it was described in the previous section, the outcome varies significantly with minor parameter changes. For example, digital control allows accurate and high precision parameter choice, therefore moving along the various modes of Fig. 3.10, which are neighboring close to each other, will be an easier task. Nonlinear phenomena in AC/AC conversion are quite a new research area. Chaos and other instabilities especially in matrix converters can also be found in [91, 92].

3.5 Summary

In this chapter, a nonlinear model of the AC/AC converter was analyzed. By deriving this model we are exploiting the advantages of discrete time methods in order to show the behavior of switching dynamics. The novelty lies on the fact that new operation regimes are discovered including period doubling oscillations and chaotic behavior. Moreover, these nonlinearities are described through bifurcation diagrams and Lyapunov exponents. Last but not least, the experimental approach and a discussion about it supported the validity of the mathematical model and will show the potential for application realisation. This kind of converter hasn't thoroughly been studied from the literature, especially from the nonlinear dynamics aspect, fact that motivated us to proceed with investigation. On the other hand, 3-phase systems are worldwide applied in the field of power systems, therefore from the next chapter a 3-phase AC/AC converter also known as matrix converter will be investigated.

4

3- ϕ Matrix Converter

‘ Πάντες ἄνθρωποι τοῦ εἰδέναι ὀρέγονται φύσει — *All men naturally desire knowledge* ’

– Aristotle (384 B.C. – 322 B.C.)

4.1 Prologue

In this chapter AC/AC conversion in the 3-phase systems will be studied. The particular converter under investigation is a 3-phase direct AC/AC matrix converter. In the beginning the basic control modulations will be described such as the Venturini modulation and Space Vector Modulation (SVM). A dynamic model will be derived which will be compared with the simulations and experimental apparatus. Finally, a small summary will be given.

4.2 Control modulations

Figure 4.1 shows the matrix converter topology. It consists of a 3-phase voltage source, input/output filters, line resistances and a resistive load. p and s refer to the primary and secondary sides of the converter, respectively. In the dynamic model and experiment results sections more description will be given about the circuit topology. The core of the converter is its switches as shown in Fig. 4.2. From this detailed layout it is obvious that 9 bidirectional switches are needed. This topology is called direct matrix converter and it differs from the indirect one mainly because it has no passive elements

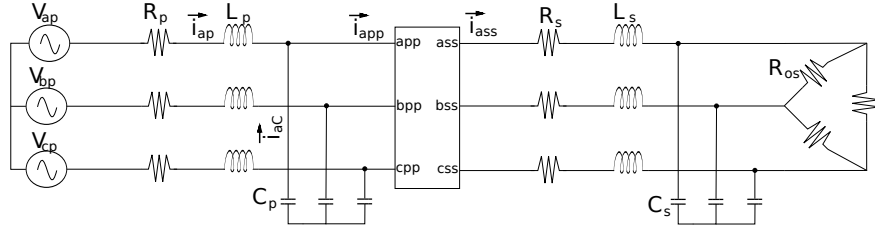


Figure 4.1: Matrix converter circuit topology.

and in particular there is no DC link. As far as the control is concerned, the basic constraints are that at any time there must be a path which connects each output phase with any input phase (to avoid open circuits) and also in every output phase there must always be only one input phase connected (to avoid short circuits). Other issues related to control, switching commutation, overvoltage protection etc. are discussed in [37].

4.2.1 Venturini modulation

The same notation as in Fig. 4.1 will not be used in the control descriptions because they refer to ideal situations. If a system of balanced input voltage sources is assumed with values $V_{A,B,C}$ and target output voltages $V_{a,b,c}$ then Eq. (4.1) describes the relationship between these voltages. The purpose of every modulation is to find a pattern for these duty cycles. The equivalent relationship for the currents is given at Eq. (4.2). T refers to the transpose matrix operation.

$$\begin{bmatrix} V_a \\ V_b \\ V_c \end{bmatrix} = \begin{bmatrix} d_{aA}d_{aB}d_{aC} \\ d_{bA}d_{bB}d_{bC} \\ d_{cA}d_{cB}d_{cC} \end{bmatrix} \begin{bmatrix} V_A \\ V_B \\ V_C \end{bmatrix} \quad (4.1)$$

$$\begin{bmatrix} I_A \\ I_B \\ I_C \end{bmatrix} = \begin{bmatrix} d_{aA}d_{aB}d_{aC} \\ d_{bA}d_{bB}d_{bC} \\ d_{cA}d_{cB}d_{cC} \end{bmatrix}^T \begin{bmatrix} I_a \\ I_b \\ I_c \end{bmatrix} \quad (4.2)$$

The Venturini modulation [31] is described in Eq. (4.3). It compares the input voltage (subscript i) with the target output voltages (subscript j) and produces the equivalent duty cycle (d) for every switch, respectively. It is a fundamental control modulation which can achieve theoretically voltage ratios up to 0.5. Voltage ratio (q) is the ratio between the output voltage and the input voltage.

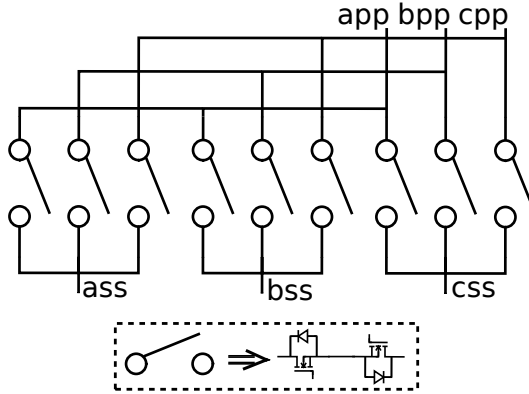


Figure 4.2: Matrix converter nine bidirectional switch topology. 18 semiconductors combined by 2 are needed for the experiment. The common source topology is again used for this converter switches.

$$d_{ij} = \frac{1}{3} \left(1 + \frac{2}{V_{pmax}^2} u_i u_j \right) \quad (4.3)$$

4.2.2 Space vector modulation

The SVM [93] is a more complex control modulation for matrix converters than the Venturini one. Let's start by supposing that the 3-phase input source has line to ground voltages as presented in Eq. (4.4). That means that the line to line voltages have the form of Eq. (4.5). V is the amplitude of the line to ground voltage and ω_i the angular velocity of the signal. Using the Clarke transformation the abc coordinates can be transferred into the dq0-plane obeying the following Eq. (4.6). V_0 is zero since a balanced 3-phase sinusoidal voltage source is considered.

$$\begin{cases} V_A = V \cos(\omega_i t) \\ V_B = V \cos(\omega_i t - \frac{2\pi}{3}) \\ V_C = V \cos(\omega_i t + \frac{2\pi}{3}) \end{cases} \quad (4.4)$$

$$\begin{cases} V_{AB} = \sqrt{3}V \cos(\omega_i t + \frac{\pi}{6}) \\ V_{BC} = \sqrt{3}V \cos(\omega_i t - \frac{\pi}{2}) \\ V_{CA} = \sqrt{3}V \cos(\omega_i t + \frac{5\pi}{6}) \end{cases} \quad (4.5)$$

$$\begin{bmatrix} V_d \\ V_q \\ V_0 \end{bmatrix} = \frac{2}{3} \begin{bmatrix} V_{AB} - \frac{1}{2}V_{BC} - \frac{1}{2}V_{CA} \\ \frac{\sqrt{3}}{2}V_{BC} - \frac{\sqrt{3}}{2}V_{CA} \\ 0 \end{bmatrix} \quad (4.6)$$

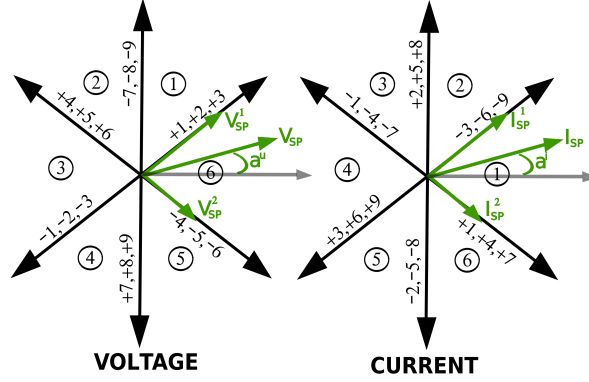


Figure 4.3: Output voltage and input current space vectors. Example for switching times when the voltage vector lies on sixth sector while the current vector lies on the first one.

The voltage angle in dq0-plane is $a_{dq0}^u = \tan^{-1} \frac{|v_q|}{|v_d|}$. The subscript dq0 will be omitted from now on and the terms a^u and a^i will be used. The equivalent equations are derived for the input current, too. Nine switches result in 512 switching combinations but there are certain restraints that have to be considered as we mentioned in the previous sections. These restraints lead to 27 possible states but 6 out of them are not going to be used since they create a rotating space vector which is not able to establish the reference vector. These rotating space vectors depend on angle frequencies ω , therefore there are not static in the vector space and as a result they are unable to be used as stationary references. Therefore, 18 active space vectors and 3 zero ones are going to be used. The basic 18 switching states are summarized in Table 4.1. The first 3 columns show which input is connected in every output each time. The dq quantities are also shown based on Eq. (4.6). According to the angle of the space vector, the 2π radian range is segmented into six sextants as in Fig. 4.3. Every active space vector takes as label a number for easier understanding and manipulation in further analysis. The zero states represent the states when all the three output phases are connected to a single input and have state names AAA, BBB, CCC or just 0 since they have no amplitude in the space vector diagram. In other words, they are all gathered in the origin of the vector space.

The next step should be the determination of switching sequence. In

Table 4.1: Basic 18 switching states and dq-plane quantities. Capital letters abc imply input and the lower case imply output signals.

a	b	c	V_{ab}	V_{bc}	V_{ca}	V_d	V_q	$ V_{dq} $	a_{dq}^i	I_A	I_B	I_C	I_d	I_q	$ I_{dq} $	a_{dq}^i	state name
A	A	B	0	V_{AB}	$-V_{AB}$	0	$\frac{2}{\sqrt{3}}V_{AB}$	$\frac{2}{\sqrt{3}}V_{AB}$	$\frac{\pi}{2}$	$-I_c$	I_c	0	$-I_c$	$\frac{1}{\sqrt{3}}I_c$	$\frac{2}{\sqrt{3}}I_c$	$\frac{5\pi}{6}$	-7 AAB
A	A	C	0	$-V_{CA}$	V_{CA}	0	$-\frac{2}{\sqrt{3}}V_{CA}$	$\frac{2}{\sqrt{3}}V_{CA}$	$-\frac{\pi}{2}$	$-I_c$	0	I_c	$-I_c$	$-\frac{1}{\sqrt{3}}I_c$	$\frac{2}{\sqrt{3}}I_c$	$\frac{7\pi}{6}$	+9 AAC
B	B	A	0	$-V_{AB}$	V_{AB}	0	$-\frac{2}{\sqrt{3}}V_{AB}$	$\frac{2}{\sqrt{3}}V_{AB}$	$-\frac{\pi}{2}$	I_c	$-I_c$	0	I_c	$-\frac{1}{\sqrt{3}}I_c$	$\frac{2}{\sqrt{3}}I_c$	$-\frac{\pi}{6}$	+7 BBA
B	B	C	0	V_{BC}	$-V_{BC}$	0	$\frac{2}{\sqrt{3}}V_{BC}$	$\frac{2}{\sqrt{3}}V_{BC}$	$\frac{\pi}{2}$	0	$-I_c$	I_c	0	$-\frac{2}{\sqrt{3}}I_c$	$\frac{2}{\sqrt{3}}I_c$	$-\frac{\pi}{2}$	-8 BBC
C	C	A	0	V_{CA}	$-V_{CA}$	0	$\frac{2}{\sqrt{3}}V_{CA}$	$\frac{2}{\sqrt{3}}V_{CA}$	$\frac{\pi}{2}$	I_c	0	$-I_c$	I_c	$\frac{1}{\sqrt{3}}I_c$	$\frac{2}{\sqrt{3}}I_c$	$\frac{\pi}{6}$	-9 CCA
C	C	B	0	$-V_{BC}$	V_{BC}	0	$-\frac{2}{\sqrt{3}}V_{BC}$	$\frac{2}{\sqrt{3}}V_{BC}$	$-\frac{\pi}{2}$	0	I_c	$-I_c$	0	$\frac{2}{\sqrt{3}}I_c$	$\frac{2}{\sqrt{3}}I_c$	$\frac{\pi}{2}$	+8 CCB
B	A	A	$-V_{AB}$	0	V_{AB}	$-V_{AB}$	$-\frac{1}{\sqrt{3}}V_{AB}$	$\frac{2}{\sqrt{3}}V_{AB}$	$\frac{7\pi}{6}$	$-I_a$	I_a	0	$-I_a$	$\frac{1}{\sqrt{3}}I_a$	$\frac{2}{\sqrt{3}}I_a$	$\frac{5\pi}{6}$	-1 BAA
C	A	A	V_{CA}	0	$-V_{CA}$	V_{CA}	$\frac{1}{\sqrt{3}}V_{CA}$	$\frac{2}{\sqrt{3}}V_{CA}$	$\frac{\pi}{6}$	$-I_a$	0	I_a	$-I_a$	$-\frac{1}{\sqrt{3}}I_a$	$\frac{2}{\sqrt{3}}I_a$	$\frac{7\pi}{6}$	+3 CAA
A	B	B	V_{AB}	0	$-V_{AB}$	V_{AB}	$\frac{1}{\sqrt{3}}V_{AB}$	$\frac{2}{\sqrt{3}}V_{AB}$	$\frac{\pi}{6}$	I_a	$-I_a$	0	I_a	$-\frac{1}{\sqrt{3}}I_a$	$\frac{2}{\sqrt{3}}I_a$	$-\frac{\pi}{6}$	+1 ABB
C	B	B	$-V_{BC}$	0	V_{BC}	$-V_{BC}$	$-\frac{1}{\sqrt{3}}V_{BC}$	$\frac{2}{\sqrt{3}}V_{BC}$	$\frac{7\pi}{6}$	0	$-I_a$	I_a	0	$-\frac{2}{\sqrt{3}}I_a$	$\frac{2}{\sqrt{3}}I_a$	$-\frac{\pi}{2}$	-2 CBB
A	C	C	$-V_{CA}$	0	V_{CA}	$-V_{CA}$	$-\frac{1}{\sqrt{3}}V_{CA}$	$\frac{2}{\sqrt{3}}V_{CA}$	$\frac{7\pi}{6}$	I_a	0	$-I_a$	I_a	$\frac{1}{\sqrt{3}}I_a$	$\frac{2}{\sqrt{3}}I_a$	$\frac{\pi}{6}$	-3 ACC
B	C	C	V_{BC}	0	$-V_{BC}$	V_{BC}	$\frac{1}{\sqrt{3}}V_{BC}$	$\frac{2}{\sqrt{3}}V_{BC}$	$\frac{\pi}{6}$	0	I_a	$-I_a$	0	$\frac{2}{\sqrt{3}}I_a$	$\frac{2}{\sqrt{3}}I_a$	$\frac{\pi}{2}$	+2 BCC
A	B	A	V_{AB}	$-V_{AB}$	0	V_{AB}	$-\frac{1}{\sqrt{3}}V_{AB}$	$\frac{2}{\sqrt{3}}V_{AB}$	$-\frac{\pi}{6}$	$-I_b$	I_b	0	$-I_b$	$\frac{1}{\sqrt{3}}I_b$	$\frac{2}{\sqrt{3}}I_b$	$\frac{5\pi}{6}$	-4 ABA
A	C	A	$-V_{CA}$	V_{CA}	0	$-V_{CA}$	$\frac{1}{\sqrt{3}}V_{CA}$	$\frac{2}{\sqrt{3}}V_{CA}$	$\frac{5\pi}{6}$	$-I_b$	0	I_b	$-I_b$	$-\frac{1}{\sqrt{3}}I_b$	$\frac{2}{\sqrt{3}}I_b$	$\frac{7\pi}{6}$	+6 ACA
B	A	B	$-V_{AB}$	V_{AB}	0	$-V_{AB}$	$\frac{1}{\sqrt{3}}V_{AB}$	$\frac{2}{\sqrt{3}}V_{AB}$	$\frac{5\pi}{6}$	I_b	$-I_b$	0	I_b	$-\frac{1}{\sqrt{3}}I_b$	$\frac{2}{\sqrt{3}}I_b$	$-\frac{\pi}{6}$	+4 BAB
B	C	B	V_{BC}	$-V_{BC}$	0	V_{BC}	$-\frac{1}{\sqrt{3}}V_{BC}$	$\frac{2}{\sqrt{3}}V_{BC}$	$-\frac{\pi}{6}$	0	$-I_b$	I_b	0	$-\frac{2}{\sqrt{3}}I_b$	$\frac{2}{\sqrt{3}}I_b$	$-\frac{\pi}{2}$	-5 BCB
C	A	C	V_{CA}	$-V_{CA}$	0	V_{CA}	$-\frac{1}{\sqrt{3}}V_{CA}$	$\frac{2}{\sqrt{3}}V_{CA}$	$-\frac{\pi}{6}$	I_b	0	$-I_b$	I_b	$\frac{1}{\sqrt{3}}I_b$	$\frac{2}{\sqrt{3}}I_b$	$\frac{\pi}{6}$	-6 CAC
C	B	C	$-V_{BC}$	V_{BC}	0	$-V_{BC}$	$\frac{1}{\sqrt{3}}V_{BC}$	$\frac{2}{\sqrt{3}}V_{BC}$	$\frac{5\pi}{6}$	0	I_b	$-I_b$	0	$\frac{2}{\sqrt{3}}I_b$	$\frac{2}{\sqrt{3}}I_b$	$\frac{\pi}{2}$	+5 CBC

Table 4.2: Switching sequences for SVM. Zero states are declared simply as 0 but there actually exist three of them (AAA, BBB, CCC). The one with the lower switchings is selected in each occasion.

$V \Rightarrow S_1, I \Rightarrow S_1$ or $V \Rightarrow S_4, I \Rightarrow S_4$ $\pm 1 \pm 3 \pm 7 \pm 9 \Rightarrow (-3 + 9 - 7 + 1)$ $0 \begin{matrix} CAA & AAC \\ \swarrow & \searrow \end{matrix} \begin{matrix} BBA & ABB \\ \swarrow & \searrow \end{matrix} \begin{matrix} AAB & BAA \\ \swarrow & \searrow \end{matrix} 0$	$V \Rightarrow S_2, I \Rightarrow S_1$ or $V \Rightarrow S_5, I \Rightarrow S_4$ $\pm 4 \pm 6 \pm 7 \pm 9 \Rightarrow (-6 + 9 - 7 + 4)$ $0 \begin{matrix} ACA & AAC \\ \swarrow & \searrow \end{matrix} \begin{matrix} BBA & BAB \\ \swarrow & \searrow \end{matrix} \begin{matrix} AAB & ABA \\ \swarrow & \searrow \end{matrix} 0$	$V \Rightarrow S_3, I \Rightarrow S_1$ or $V \Rightarrow S_6, I \Rightarrow S_4$ $\pm 1 \pm 3 \pm 4 \pm 6 \Rightarrow (-3 + 6 - 4 + 1)$ $0 \begin{matrix} CAA & ACA \\ \swarrow & \searrow \end{matrix} \begin{matrix} BAB & ABB \\ \swarrow & \searrow \end{matrix} \begin{matrix} ABA & BAA \\ \swarrow & \searrow \end{matrix} 0$
$V \Rightarrow S_1, I \Rightarrow S_2$ or $V \Rightarrow S_4, I \Rightarrow S_5$ $\pm 2 \pm 3 \pm 8 \pm 9 \Rightarrow (-8 + 2 - 3 + 9)$ $0 \begin{matrix} CCB & BCC \\ \swarrow & \searrow \end{matrix} \begin{matrix} CAA & AAC \\ \swarrow & \searrow \end{matrix} \begin{matrix} ACC & CCA \\ \swarrow & \searrow \end{matrix} 0$	$V \Rightarrow S_2, I \Rightarrow S_2$ or $V \Rightarrow S_5, I \Rightarrow S_5$ $\pm 5 \pm 6 \pm 8 \pm 9 \Rightarrow (-8 + 5 - 6 + 9)$ $0 \begin{matrix} CCB & CBC \\ \swarrow & \searrow \end{matrix} \begin{matrix} ACA & AAC \\ \swarrow & \searrow \end{matrix} \begin{matrix} CAC & CCA \\ \swarrow & \searrow \end{matrix} 0$	$V \Rightarrow S_3, I \Rightarrow S_2$ or $V \Rightarrow S_6, I \Rightarrow S_5$ $\pm 2 \pm 3 \pm 5 \pm 6 \Rightarrow (-2 + 5 - 6 + 3)$ $0 \begin{matrix} BCC & CBC \\ \swarrow & \searrow \end{matrix} \begin{matrix} ACA & CAA \\ \swarrow & \searrow \end{matrix} \begin{matrix} CAC & ACC \\ \swarrow & \searrow \end{matrix} 0$
$V \Rightarrow S_1, I \Rightarrow S_3$ or $V \Rightarrow S_4, I \Rightarrow S_6$ $\pm 1 \pm 2 \pm 7 \pm 8 \Rightarrow (-1 + 7 - 8 + 2)$ $0 \begin{matrix} ABB & BBA \\ \swarrow & \searrow \end{matrix} \begin{matrix} CCB & BCC \\ \swarrow & \searrow \end{matrix} \begin{matrix} BBC & CBB \\ \swarrow & \searrow \end{matrix} 0$	$V \Rightarrow S_2, I \Rightarrow S_3$ or $V \Rightarrow S_5, I \Rightarrow S_6$ $\pm 4 \pm 5 \pm 7 \pm 8 \Rightarrow (-4 + 7 - 8 + 5)$ $0 \begin{matrix} BAB & BBA \\ \swarrow & \searrow \end{matrix} \begin{matrix} CCB & CBC \\ \swarrow & \searrow \end{matrix} \begin{matrix} BBC & BCB \\ \swarrow & \searrow \end{matrix} 0$	$V \Rightarrow S_3, I \Rightarrow S_3$ or $V \Rightarrow S_6, I \Rightarrow S_6$ $\pm 1 \pm 2 \pm 4 \pm 5 \Rightarrow (-1 + 4 - 5 + 2)$ $0 \begin{matrix} ABB & BAB \\ \swarrow & \searrow \end{matrix} \begin{matrix} CBC & BCC \\ \swarrow & \searrow \end{matrix} \begin{matrix} BCB & CBB \\ \swarrow & \searrow \end{matrix} 0$
$V \Rightarrow S_1, I \Rightarrow S_4$ or $V \Rightarrow S_4, I \Rightarrow S_1$ $\pm 1 \pm 3 \pm 7 \pm 9 \Rightarrow (-9 + 3 - 1 + 7)$ $0 \begin{matrix} AAC & CAA \\ \swarrow & \searrow \end{matrix} \begin{matrix} ABB & BBA \\ \swarrow & \searrow \end{matrix} \begin{matrix} BAA & AAB \\ \swarrow & \searrow \end{matrix} 0$	$V \Rightarrow S_2, I \Rightarrow S_4$ or $V \Rightarrow S_5, I \Rightarrow S_1$ $\pm 4 \pm 6 \pm 7 \pm 9 \Rightarrow (-9 + 6 - 4 + 7)$ $0 \begin{matrix} AAC & ACA \\ \swarrow & \searrow \end{matrix} \begin{matrix} BAB & BBA \\ \swarrow & \searrow \end{matrix} \begin{matrix} ABA & AAB \\ \swarrow & \searrow \end{matrix} 0$	$V \Rightarrow S_3, I \Rightarrow S_4$ or $V \Rightarrow S_6, I \Rightarrow S_1$ $\pm 1 \pm 3 \pm 4 \pm 6 \Rightarrow (-6 + 3 - 1 + 4)$ $0 \begin{matrix} ACA & CAA \\ \swarrow & \searrow \end{matrix} \begin{matrix} ABB & BAB \\ \swarrow & \searrow \end{matrix} \begin{matrix} BAA & ABA \\ \swarrow & \searrow \end{matrix} 0$
$V \Rightarrow S_1, I \Rightarrow S_5$ or $V \Rightarrow S_4, I \Rightarrow S_2$ $\pm 2 \pm 3 \pm 8 \pm 9 \Rightarrow (-2 + 8 - 9 + 3)$ $0 \begin{matrix} BCC & CCB \\ \swarrow & \searrow \end{matrix} \begin{matrix} AAC & CAA \\ \swarrow & \searrow \end{matrix} \begin{matrix} CCA & ACC \\ \swarrow & \searrow \end{matrix} 0$	$V \Rightarrow S_2, I \Rightarrow S_5$ or $V \Rightarrow S_5, I \Rightarrow S_2$ $\pm 5 \pm 6 \pm 8 \pm 9 \Rightarrow (-5 + 8 - 9 + 6)$ $0 \begin{matrix} CBC & CCB \\ \swarrow & \searrow \end{matrix} \begin{matrix} AAC & ACA \\ \swarrow & \searrow \end{matrix} \begin{matrix} CCA & CAC \\ \swarrow & \searrow \end{matrix} 0$	$V \Rightarrow S_3, I \Rightarrow S_5$ or $V \Rightarrow S_6, I \Rightarrow S_2$ $\pm 2 \pm 3 \pm 5 \pm 6 \Rightarrow (-5 + 2 - 3 + 6)$ $0 \begin{matrix} CBC & BCC \\ \swarrow & \searrow \end{matrix} \begin{matrix} CAA & ACA \\ \swarrow & \searrow \end{matrix} \begin{matrix} ACC & CAC \\ \swarrow & \searrow \end{matrix} 0$
$V \Rightarrow S_1, I \Rightarrow S_6$ or $V \Rightarrow S_4, I \Rightarrow S_3$ $\pm 1 \pm 2 \pm 7 \pm 8 \Rightarrow (-7 + 1 - 2 + 8)$ $0 \begin{matrix} BBA & ABB \\ \swarrow & \searrow \end{matrix} \begin{matrix} BCC & CCB \\ \swarrow & \searrow \end{matrix} \begin{matrix} CBB & BBC \\ \swarrow & \searrow \end{matrix} 0$	$V \Rightarrow S_2, I \Rightarrow S_6$ or $V \Rightarrow S_5, I \Rightarrow S_3$ $\pm 4 \pm 5 \pm 7 \pm 8 \Rightarrow (-7 + 4 - 5 + 8)$ $0 \begin{matrix} BBA & BAB \\ \swarrow & \searrow \end{matrix} \begin{matrix} CBC & CCB \\ \swarrow & \searrow \end{matrix} \begin{matrix} BCB & BBC \\ \swarrow & \searrow \end{matrix} 0$	$V \Rightarrow S_3, I \Rightarrow S_6$ or $V \Rightarrow S_6, I \Rightarrow S_3$ $\pm 1 \pm 2 \pm 4 \pm 5 \Rightarrow (-4 + 1 - 2 + 5)$ $0 \begin{matrix} BAB & ABB \\ \swarrow & \searrow \end{matrix} \begin{matrix} BCC & CBC \\ \swarrow & \searrow \end{matrix} \begin{matrix} CBB & BCC \\ \swarrow & \searrow \end{matrix} 0$

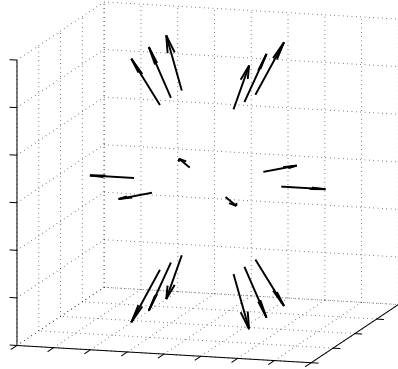


Figure 4.4: The 18 switching states unified in a single three-dimensional figure. Actually it is about a four dimensional figure but the projection of one plane loses one of its dimensions.

every moment the measured current and voltage will create a space vector which will be rotating in the vector space. Thus, the optimal switching combination should be decided according to which sextants the equivalent space vectors lie on. There are 36 possible switching combinations since there are 6 sextants for the voltage and another 6 for the current. The fact that every sector has another one vertically opposite to it makes the switching sequences half the amount. These 18 switching sequences are shown in Table 4.2. Let's explain this by giving an example when the voltage vector lies on the sixth sector and the current vector on the first one. There has to be 4 common states in both current and voltage sectors that could help on the partial structure of the space vectors from the reference ones. These states are $\pm 1, \pm 3, \pm 4, \pm 6$ by observing Fig. 4.3. Among these four double states the pattern that gives us minimum switching transition is $-6, +3, -1, +4$. The final result will be the algebraic sum of the equivalent vectors. There are also 3 zero states that complete the pattern. Every time the zero pattern is the state that also minimizes the switchings. In this example the three zero states are CCC, AAA, BBB so that the complete switching sequence will be CCC, CAC, CAA, AAA, BAA, BAB, BBB. Notice that in every switching only one letter is changing, fact that means minimum switching. These 18 possible states can be unified into a single Fig. 4.4. The horizontal six states are the same of the voltage space vector diagram. Once that is decided, we are moving perpendicular to the horizontal plane to find the

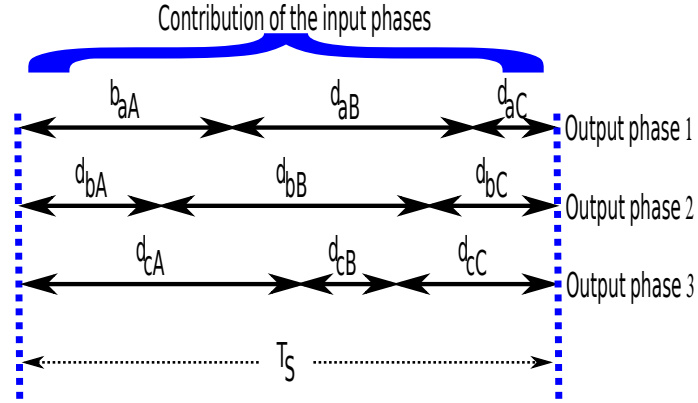


Figure 4.5: Typical switching pattern. All input phases occupy some of the switching period time.

Table 4.3: 21 switching states. Each state is described by which switches is on.

	S_1	S_2	S_3	S_4	S_5	S_6	S_7	S_8	S_9	index
AAB	1	1				1				-7
AAC	1	1							1	+9
BBA			1	1	1					+7
BBC				1	1				1	-8
CCA			1				1	1		-9
CCB						1	1	1		+8
BAA		1	1	1						-1
CAA		1	1				1			+3
ABB	1				1	1				+1
CBB					1	1	1			-2
ACC	1							1	1	-3
BCC				1				1	1	+2
ABA	1		1		1					-4
ACA	1		1					1		+6
BAB		1		1		1				+4
BCB				1		1		1		-5
CAC		1					1		1	-6
CBC					1		1		1	+5
AAA	1	1	1							
BBB				1	1	1				
CCC							1	1	1	

equivalent current space vector and also the final switching state. More about that issue is covered in Appendix E.

As for the switching times, again from our example, the sinus law gives Eq. (4.7) based on Fig. 4.3. In this figure the measured space vectors for the instantaneous values of current and voltage are shown with the subscript sp. Each one is decomposed in the neighboring static space vectors ($V_{sp}^{1,2}$ and $I_{sp}^{1,2}$). In this equation $V_{sp}^1 = V_{+3} + V_{-1} = \frac{2}{\sqrt{3}}V_{CA}d_{+3} + \frac{2}{\sqrt{3}}V_{AB}d_{-1}$, $I_{sp}^1 = \frac{2}{\sqrt{3}}I_a d_{+3}$, and $I_{sp}^2 = \frac{2}{\sqrt{3}}I_a d_{-1}$, respectively. From the system of Eq. (4.7) we can solve for d_{+3} and d_{-1} the result of which is shown in Eq. (4.8).

Accordingly, from V_{sp}^2 and the two other combinations the times for d_{+4} and d_{-6} can be derived. The zero states share a third of the remaining time ($d_0 = 1 - d_{-1} - d_{+3} - d_{+4} - d_{-6}$). In our previous example, the times will be $[\frac{d_0}{3}, d_{-6}, d_{+3}, \frac{d_0}{3}, d_{-1}, d_{+4}, \frac{d_0}{3}]$. There are many patterns for the switching sequences, especially how the zero states can be distributed with different result in operation and harmonics as in [93]. The one-third pattern was chosen here for its simplicity and low harmonic result. A typical switching pattern is presented in Fig. 4.5. Notice that in every output phase all the input phases occupy some of the time of the switching period. In addition, the switching between the phases shouldn't happen at the same time to avoid short circuits and components damage. Control strategies and such switching patterns are compared at [94]. The 18 switching states along with the three zero states are presented in Table 4.3 where it is also shown which switches are on at each time. In addition, a graphical representation of the decision of the switching patterns of Tables 4.1 and 4.2 is shown at the Appendix E.

$$\begin{cases} V_{sp}^1 \sin(\frac{2\pi}{3}) = V_{sp} \sin(\frac{\pi}{6} + \alpha^u) \\ I_{sp}^1 \sin(\frac{\pi}{6} - \alpha^i) = I_{sp}^2 \sin(\frac{\pi}{6} + \alpha^i) \end{cases} \quad (4.7)$$

$$\begin{cases} d_{+3} = \frac{\sin(\frac{\pi}{6} + \alpha^u)q}{\frac{\sin(\frac{\pi}{6} - \alpha^i)V_{AB}}{\sin(\frac{\pi}{6} + \alpha^i)} + V_{CA}} \\ d_{-1} = \frac{d_{+3} \sin(\frac{\pi}{6} - \alpha^i)}{\sin(\frac{\pi}{6} + \alpha^i)} \end{cases} \quad (4.8)$$

4.3 Dynamic model

In this section the dynamic model of the matrix converter is derived. It is assumed that u_{abcp} (or just u_p) are the input voltage sources for phases a, b, and c respectively. The subscript p refers to the primary side of the converter and s to the secondary one. An averaged model will be used based on the low frequency transfer matrix D [95] as also shown in Eq. (4.9). The low frequency transfer matrix is composed partially by two other matrices ($D_{1,2}$) each one participating in the final result by a percentage given by $\mu \in [0, 1]$. These matrices are given in Eqs. (4.10) and (4.11) where, $x_1(t) = \omega_p t - \omega_s t - \alpha_s$ and $x_2(t) = \omega_p t + \omega_s t + \alpha_s$. In the aforementioned equations $\omega_{p,s}$ represent the angular velocities of the primary and secondary sides of the matrix converter, α_s is the output voltage angle if the input

one is considered as reference ($\alpha_p = 0$), and q is the voltage ratio between the amplitudes of input voltage ($u_{abc_{pmax}}$) and output voltage ($u_{abc_{smax}}$). In fact, D_1 gives the same angle displacement between input and output, while D_2 gives an input angle displacement same in amplitude but opposite in sign to that of the output. By controlling μ the input angle displacement can be adjusted and also can be unity ($\mu = 0.5$) as it is proven in [95] and [96].

$$D = \frac{1}{3}(\mu(1 + D_1) + (1 - \mu)(1 + D_2)) \quad (4.9)$$

$$D_1 = \begin{bmatrix} 2q \cos(x_1(t)) & 2q \cos(x_1(t) - \frac{2\pi}{3}) & 2q \cos(x_1(t) + \frac{2\pi}{3}) \\ 2q \cos(x_1(t) + \frac{2\pi}{3}) & 2q \cos(x_1(t)) & 2q \cos(x_1(t) - \frac{2\pi}{3}) \\ 2q \cos(x_1(t) - \frac{2\pi}{3}) & 2q \cos(x_1(t) + \frac{2\pi}{3}) & 2q \cos(x_1(t)) \end{bmatrix} \quad (4.10)$$

$$D_2 = \begin{bmatrix} 2q \cos(x_2(t)) & 2q \cos(x_2(t) - \frac{2\pi}{3}) & 2q \cos(x_2(t) + \frac{2\pi}{3}) \\ 2q \cos(x_2(t) - \frac{2\pi}{3}) & 2q \cos(x_2(t) + \frac{2\pi}{3}) & 2q \cos(x_2(t)) \\ 2q \cos(x_2(t) + \frac{2\pi}{3}) & 2q \cos(x_2(t)) & 2q \cos(x_2(t) - \frac{2\pi}{3}) \end{bmatrix} \quad (4.11)$$

Analysis based on one phase can be performed, since the system is a balanced one. There are four state variables in this problem, i.e. input/output filter inductance currents and input/output filter capacitance voltages. Let i_p and i_{ss} be the primary and secondary inductance currents and u_{pp} and u_s the primary and secondary capacitance voltages. These suffixes are summarized in Table 4.4. The complete system is shown in Eq. (4.12). $R_{p,s,os}$ denote the primary line resistance, secondary line resistance, and output load resistance, respectively. The multiplication with D helps to represent a state variable from the primary side in terms of the secondary side and the opposite as showing in Eq. (4.13). This equation has already been adopted in Eq. (4.12) in order to show the dynamic model in terms of the four state variables.

$$\left\{ \begin{array}{l} L_p \frac{d}{dt}(i_p) = u_p - R_p i_p - u_{pp} \\ C_p \frac{d}{dt}(u_{pp}) = i_p - D^T i_{ss} \\ L_s \frac{d}{dt}(i_{ss}) = D u_{pp} - R_s i_{ss} - u_s \\ C_s \frac{d}{dt}(u_s) = i_{ss} - \frac{1}{R_{os}} u_s \end{array} \right. \quad (4.12)$$

Table 4.4: Suffixes description for the derivation of the matrix converter dynamic model.

Suffixes	Description
p	Primary values before the input filter
pp	Primary values after the input filter
s	Secondary values after the output filter
ss	Secondary values before the output filter

$$\begin{cases} u_{ss} = Du_{pp} \\ i_{pp} = D^T i_{ss} \end{cases} \quad (4.13)$$

Using Park transformation the analysis can be facilitated since the abc-coordinates can be transformed into the dq0-reference frame using the transformation matrix Λ shown in Eq. (4.14). Moreover, all the state variables should be transferred into one side of the converter and the secondary side is selected in this analysis. This is succeeded by using the transfer matrix D and Eq. (4.13). It can be easily noticed from Eq. (4.12) that the variables which have to be transferred into the secondary side are the i_p , u_p , and u_{pp} . Using the transfer matrix D the following substitutions $i_p^D = Di_p$, $u_p^D = Du_{ip}$, and $u_{ss} = Du_{pp}$ can be derived. The superscript D denotes that the variable is referred to the secondary side of the converter. Therefore, by using these substitutions and the formula $\psi_{abc} = \Lambda^{-1}\psi_{dq0}$, Eq. (4.12) can be represented as in Eq. (4.15).

$$\Lambda = \frac{2}{3} \begin{bmatrix} \cos(\omega_s t) & \cos(\omega_s t - \frac{2\pi}{3}) & \cos(\omega_s t + \frac{2\pi}{3}) \\ \sin(\omega_s t) & \sin(\omega_s t - \frac{2\pi}{3}) & \sin(\omega_s t + \frac{2\pi}{3}) \\ \frac{1}{2} & \frac{1}{2} & \frac{1}{2} \end{bmatrix}, \quad (4.14)$$

$$\frac{d}{dt}\vec{\mathbf{x}} = A\vec{\mathbf{x}} + B\vec{\mathbf{u}}, \quad (4.15)$$

where,

$$\vec{\mathbf{x}} = [i_{qp}^D \quad i_{dp}^D \quad u_{qss} \quad u_{dss} \quad i_{qss} \quad i_{dss} \quad u_{qs} \quad u_{ds}]^T,$$

$$A = \begin{bmatrix} 0 & 0 & -\frac{R_p}{L_p} - p_1 & -p_2 & -\frac{1}{L_p} & 0 & 0 & 0 \\ 0 & 0 & -p_3 & -\frac{R_p}{L_p} - p_4 & 0 & -\frac{1}{L_p} & 0 & 0 \\ -\frac{r_1}{C_p} & -\frac{r_2}{C_p} & \frac{1}{C_p} & 0 & -p_1 & -p_2 & 0 & 0 \\ -\frac{r_3}{C_p} & -\frac{r_4}{C_p} & 0 & \frac{1}{C_p} & -p_3 & -p_4 & 0 & 0 \\ -\frac{R_s}{L_s} & -\omega_s & 0 & 0 & \frac{1}{L_s} & 0 & -\frac{1}{L_s} & 0 \\ \omega_s & -\frac{R_s}{L_s} & 0 & 0 & 0 & \frac{1}{L_s} & 0 & -\frac{1}{L_s} \\ \frac{1}{C_s} & 0 & 0 & 0 & 0 & 0 & -\frac{1}{R_{os}C_s} & -\omega_s \\ 0 & \frac{1}{C_s} & 0 & 0 & 0 & 0 & \omega_s & -\frac{1}{R_{os}C_s} \end{bmatrix},$$

$$B = \begin{bmatrix} \frac{1}{L_p} & 0 & 0 & 0 & 0 & 0 & 0 & 0 \\ 0 & \frac{1}{L_p} & 0 & 0 & 0 & 0 & 0 & 0 \end{bmatrix}^T,$$

$$p_1 = \frac{(\omega_p - \omega_s)[- \mu \sin(2\alpha_s)(\mu - 1)]}{(2\mu - 1)} = -p_4,$$

$$p_2 = \frac{(\omega_p - \omega_s)[\mu(\mu + \cos(2\alpha_s) - \mu \cos(2\alpha_s))]}{(2\mu - 1)},$$

$$p_3 = \frac{(\omega_p - \omega_s)[- \mu(\mu - \cos(2\alpha_s) + \mu \cos(2\alpha_s))]}{(2\mu - 1)},$$

$$r_1 = q^2[(\mu - 1)^2 + \mu^2 - 2\mu \cos(2\alpha_s)(\mu - 1)],$$

$$r_2 = 2\mu q^2 \sin(2\alpha_s)(\mu - 1) = r_3,$$

and,

$$r_4 = q^2[(\mu - 1)^2 + \mu^2 + 2\mu \cos(2\alpha_s)(\mu - 1)].$$

Finally the vector $\vec{u} = [u_{qp}^D \ u_{dp}^D]^T$ consists of the input voltage dq quantities. Since the system is balanced, the third dq0-component is always zero. T represents the transpose operation and matrix algebraic simplifications are performed with Matlab toolbox. Finally similar dynamic models have also been studied in [96, 97, 98].

4.4 Results and discussion

Both steady and transient state should be studied for a normal matrix converter operation. For the dynamic model of Fig. 4.1 the parameters are set as $R_{p,s} = 6 \Omega$, $C_{p,s} = 330 \mu\text{F}$, $L_{p,s} = 47 \text{ mH}$, and $R_{os} = 12 \Omega$. Moreover, a balanced 3-phase sinusoidal voltage source is assumed with amplitude $V_{abc_{p_{\max}}} = 100 \text{ V}$ and the desired voltage ratio q is set at 0.25. The signals for the input and output voltages are shown in Fig. 4.6. After the start-up transient, steady state operation is clear. There is saturation in the voltage ratio and it is due to power losses in filter lines and efficiency reduction because of the control inability to maintain the efficiency in high voltage ratio levels as it is proven in Fig. 4.7. In this figure the comparison is also shown between the dynamic and Simulink model. The control modulations set a voltage ratio in the horizontal axis and the actual voltage ratio is measured from the outcome. Ideally these two values should be equal. But in reality, they both deviate from the ideal values. In fact due to higher harmonics the Simulink model has inferior results from the dynamic model. In addition, the Simulink model takes under consideration the switching frequency impact. For example, in Fig. 4.8 the envelope of one output phase of the matrix converter is shown. We can see the contribution of all the three input phases in this single output phase signal. The result for the output phase will be deducted by filtering out from this envelope its fundamental harmonic. On the other hand, the averaging dynamic model doesn't consider such issues but instead it exemplifies them. In the particular case of Fig.

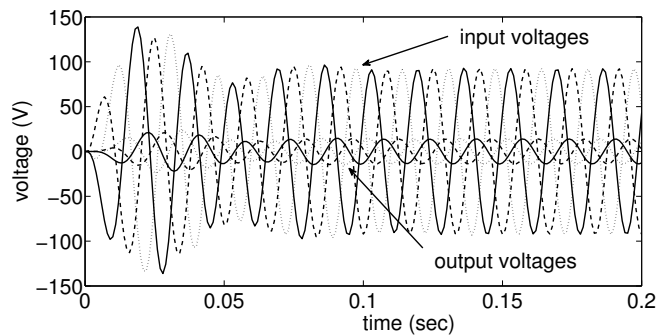


Figure 4.6: Input and output voltages during converter start-up when the ideal voltage ratio is set at 0.25. The measured voltage ratio is found to be lower than this value due to the voltage ratio limitations.

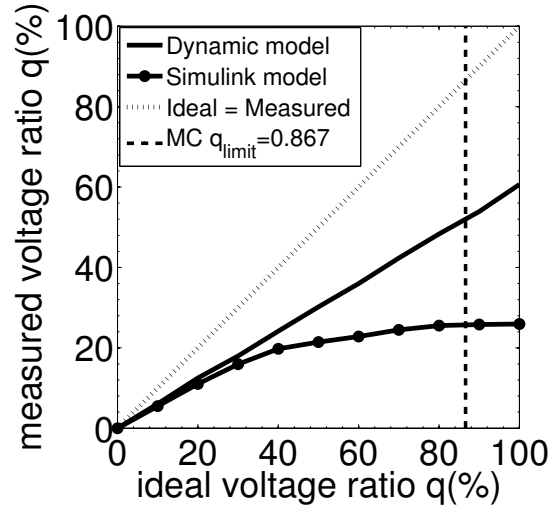


Figure 4.7: Comparison of the voltage ratio saturation between Simulink and dynamic model. They both deviate from the ideal values.

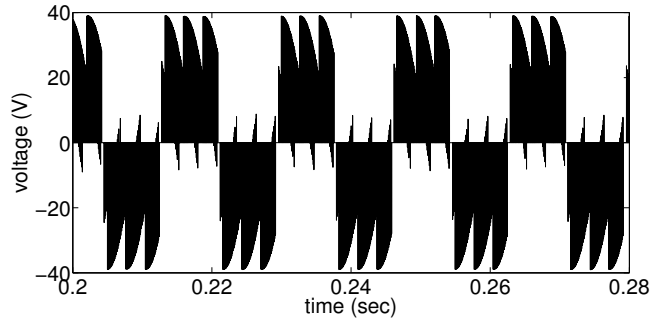


Figure 4.8: Output voltage envelope of matrix converter in the Simulink model. The contribution of all the three input phase are visible as well as the switching frequency impact.

4.6 the voltage ratio happens to be smaller than 0.25 as it is also confirmed by Fig. 4.7. The complete simulation results of the voltage ratio limitations will be compared with the experimental ones in the next paragraphs.

Efficiency is presented according to the change of voltage ratio in Fig. 4.9 for the dynamic model. In voltage ratios higher than 85% efficiency drops down to 73%. Interesting phenomena appear in the following Fig. 4.10. In this simulation, the input (output) frequency is kept constant at 50 Hz while the efficiency result is saved for various output (input) frequency values. The result is shown with the dashed (solid) line when the input (out-

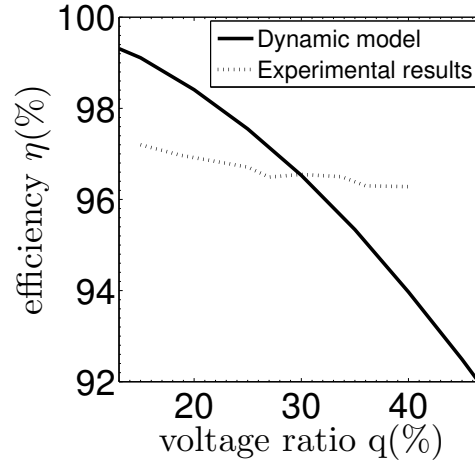


Figure 4.9: Efficiency drops as the voltage ratio increases.

put) frequency is constant. The desired voltage ratio is always set at 0.75. Both simulations express similar behavior as frequency increases. Efficiency decreases in higher frequency range and as a result the converter operation has increased power losses. However, a resonance appears at 165 Hz resulting in efficiency values that are unacceptable for the practical point of view. In other words, this operation should be strictly prohibited for actual realisation since it may result in instability or damage of the apparatus. Many fuses have been burned actually during experiments for high line frequencies tests showing this potential hazard. On the other hand, if the operation could be restricted to the sides of the resonance hill, then efficiency can reach better values at higher frequencies, too. By this way, both higher operating frequency and efficiency can be achieved.

The next step is to explain the origin of this resonance. The quality factor that RLC parameters create is responsible for any frequency resonances in the frequency response. Indeed, the resonance can be moved to higher frequencies by changing the parameters of the passive elements. In that case, the problem would be how far in the frequency axis can this resonance be placed and the solution lies on Fig. 4.11. In this figure, x-axis is the logarithmic value of the fraction between the secondary and primary operating frequencies. As this value increases, i.e. output frequency is higher than the input one, voltage ratio q starts decreasing fast around the value of 3 which

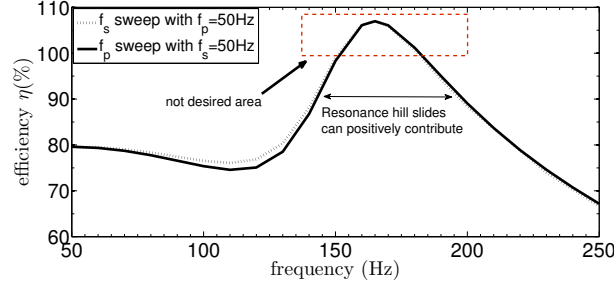


Figure 4.10: Input (output) frequency sweeps when the output (input) frequency is held constant. In the high frequency range efficiency dramatically decreases. Resonance hills can be used to increase the frequency and efficiency at the same time.

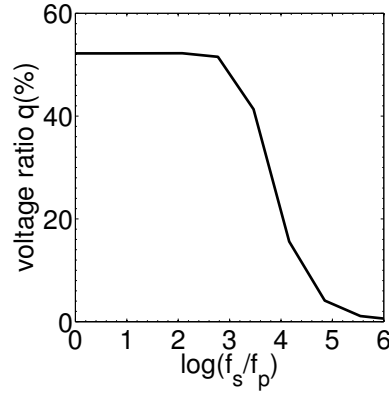


Figure 4.11: When the difference between f_p and f_s increases, the voltage ratio decreases, hence the optimum operating frequency can be decided.

means the output frequency is around 1000 times bigger than the input one. As a result, by inspecting Fig. 4.11, maximum frequency can be decided and if the RLC parameter restraints are also permitting (depending on the circuit design) then the decision of the resonance in Fig. 4.10 can be made.

Some transients are going to be examined in the following before the experimental results. In the beginning, a voltage sag occurred in the input voltage source is presented. Voltage sags are one of the most severe power quality problems appeared in the power-grid [99]. A voltage sag can be caused due to motor starting or even short circuits on the grid. The transient behavior is examined in the two-dimensional phase plane between active and reactive power as in Fig. 4.12. The operation converges in the

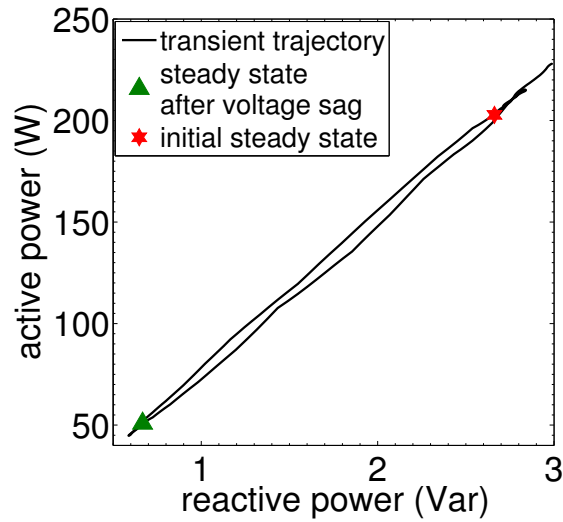


Figure 4.12: Phase plane between active and reactive power for 50% voltage sag. The first transient during starting is not shown in order to emphasize the voltage sag operation.

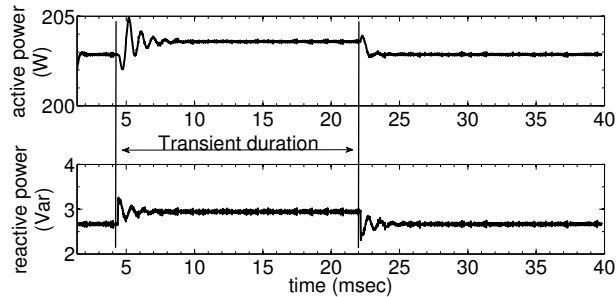


Figure 4.13: Frequency increases 10% and the result of active and reactive power is shown in the equivalent times series; minor changes occur.

initial steady state at around 200 W (red star). Voltage drops 50% at a certain moment and eventually the operation reconverges to the second steady state at around 50 W (green triangle). When the voltage is restored to the nominal values, the trajectory reconverges almost from the same path, back to the initial steady state. Thus, matrix converter coped satisfactorily enough with the voltage sag.

Another crucial problem of power-grids is the maintenance of the operating frequency. Figure 4.13 presents a frequency transient in the time domain. At approximately 0.05sec and for about one cycle the frequency is

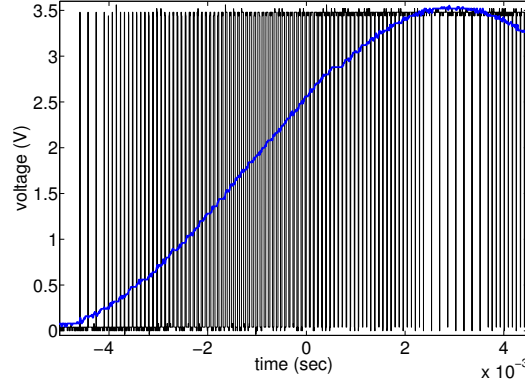


Figure 4.14: FPGA and A/D converters are used for the experimental pulses. Blue graph represents the required duty cycle as an analogue electrical signal and the black graph is the actual pulse of the FPGA output for one of the nine bidirectional switches.

increased by 10%. It is clear that minimal change takes place during this transient since an overshoot less than 1% appears. The nominal levels are restored once the frequency gets its normal value.

An experimental matrix converter is realised to confirm the operation. The dynamic model used in the simulation is an averaged model. Therefore it is unable to explain phenomena that switching frequency can create. As for the 3-phase input voltage source, two power amplifiers connected in series providing the third input voltage source by their common connection are used. That is exactly the reason how the balance is lost in the experiment. However, the 3-phase input source is created and for the purpose of this work is sufficient since we are aiming at the practical side of the matrix converter operation. In addition the bidirectional switches were implemented with SiC D-MOSFETs to cope with high switching frequencies. Moreover, the derivation of the switching times directly from Eqs. (4.10) and (4.11) is not an easy task for the experimental realisation so the duty cycles are found from Eq. (4.3) as described in [37]. The target output voltages are created and along with the measurement of the input ones, the duty cycles are created with the help also of FPGA. An example is given at Fig. 4.14. The blue graph is the signal that represents the duty cycle of one of the nine switches. This signal is manipulated according to FPGA and A/D converter so that the final result will be the rectangular pulse with the black color. It is clear that the duty cycle is increasing in high values of the equivalent

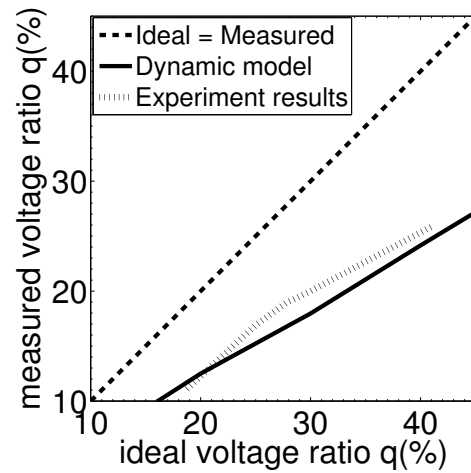


Figure 4.15: Ideal voltage ratio versus measured one. The experimental results of this work are compared with the dynamic model.

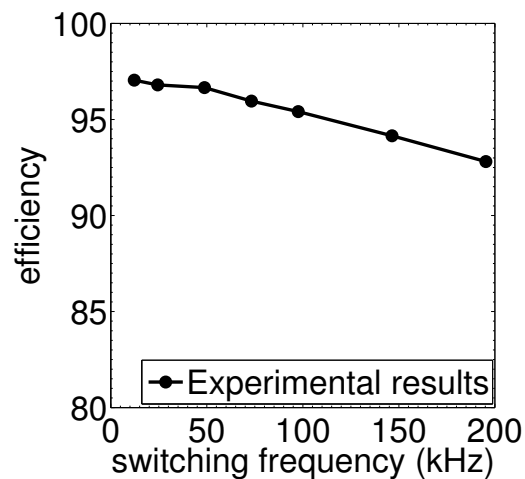


Figure 4.16: An important factor of the efficiency reduction is the switching frequency.

signal. This pulse is only 3.3 V amplitude which means that it is the output of the FPGA itself. This pulse is driven to the equivalent drive circuit to bring the voltage amplitude to the required values. A detailed diagram and explanation of the control is presented also at the Appendix F.

Figure 4.15 shows the voltage ratio limitations. The horizontal axis is the ideal q which is set by the control and the vertical axis is the actual

q measured between the input and output voltages. The dynamic model results have already been presented in Fig. 4.7 with the Simulink model and now the comparison between the former ones with the experimental ones is discussed. Both graphs almost coincide to each other and equally decline from the ideal trajectory in which the measured q is supposed to be equal with the ideal one. The modulation cannot provide correct results at the borders of voltage ratio ($q \in (0, 0.5)$) since the phase synchronization between the phases is difficult to be achieved. In particular, in low voltage ratios, signal processing is unable to make correct balanced 3-phase sinusoidal signals. On the other hand, in high voltage ratios, the current sensors are unable to measure higher current values, so that the result is incorrect. In Fig. 4.16 the impact of switching frequency on efficiency is presented. Power loss happens in high switching frequency but it is worth mentioning that the converter has no snubber circuits for further switching frequency loss reduction. Switching frequencies almost up to 200 kHz were tested.

4.5 Summary

Matrix converter pros and cons were analyzed and discussed in this chapter. The fundamental control modulations were presented and simulation results with Simulink and dynamic model equations were compared. The RLC parameters play a great role since they can produce various resonances which can be exploited to increase the efficiency of the converter. But on the other hand, voltage ratio can't be kept in high output line frequencies, therefore there is a restriction of the highest value the output frequency can take. Experimental results were also presented and the voltage ratio measurements showed good agreement with the dynamic model. Other issues were studied such as transient behavior and so on. After confirming the operation of the matrix converter the next goal would be to apply it with a power router and investigate the dynamics of the combined system. The next and final main chapter will deal with this application.

5

Power Router 3- ϕ Switching

‘ Ὠκεανός, ὡσπερ γένεσις πάντεσσι τέτυκται — *Ocean, the genesis of everything* ’

– Homer (8th century A.D.)

5.1 Prologue

This chapter is devoted to an application of matrix converter with power router. The direct matrix converter analyzed in previous chapters is creating a 3-phase output voltage which is used as an input for a power router. Various switching scenarios are tested both in simulations and experiments with good agreement on their results. Before these results, the experimental layout is presented. We summarize in the end of this chapter with a small conclusion section.

Power routers, which can be distributed according to the load-demand, can perform switching to connect particular loads with the desired input sources. We assume the routers and matrix converters to have m inputs and n outputs, as shown in Fig. 5.1. The matrix converter receives the input phases from the utility-grid and outputs them to the power routers installed on the smart-grid which may also receive power from decentralized power generators (DPGs). One or more routers together can form a micro-grid according to the localized control system needs. This study considers the most common case scenario of a 3-phase system. Therefore, we will scale down our experiments to only three phases. In fact, this figure is a similar representation, but only with the main electrical parts, of Fig. 1.2. One

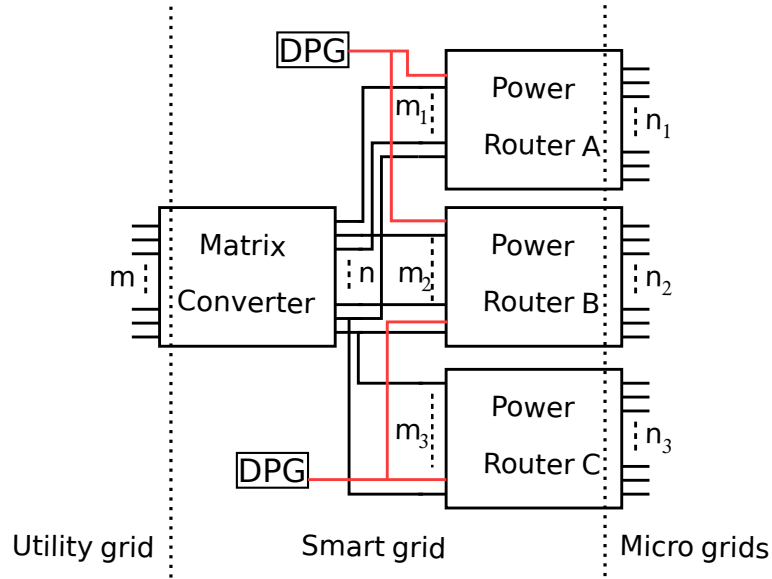


Figure 5.1: Generalized idea of matrix converter and power routers. All can have multiple input/output ports and various decentralized power generators (DPG) are distributed within the smart-grid.

may notice that the matrix converter has a similar function with the power router but this is untrue since the scope and target applications are completely different. Matrix converter is targeted to replace the transformers as for example in the point of common coupling. It utilizes high switching frequency and it can modulate the input phases. On the other hand, power routers are scattered throughout the grid and they have two main goals. They achieve localized control by partitioning the smart-grid into smaller micro-grids but also they ensure that distributed power generators are used to the maximum of their abilities.

5.2 Experimental layout

Figure 5.2 presents the schematic of the overall device. The matrix converter which was studied in the previous chapter is on the left part of the figure. It is a 3-phase to 3-phase converter but instead of the output load the power router is attached to its output. A switching scenario setting is also shown in this figure. When the purple switches are on (state 1) all the loads are connected to an input source but when the blue switches are on (state

Table 5.1: Basic 3-phase switching scenario. State 1 is the steady state before switching. Each load is fed with a different phase-to-phase voltage after switching (State 2). AB, BC, and CA refer to the phase-to-phase voltages.

Load No.	State 1	State 2
1	AB	CA
2	BC	AB
3	CA	BC

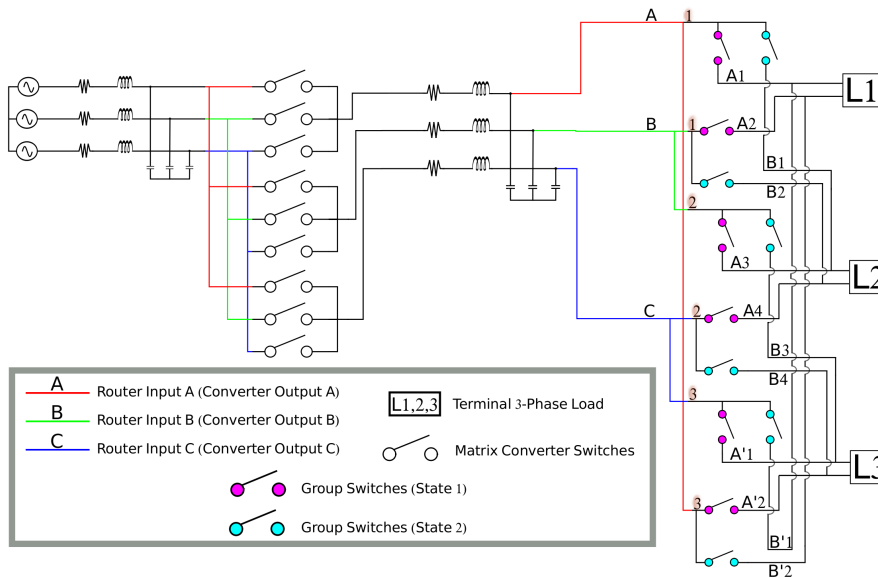


Figure 5.2: Simplified circuit topology of the direct matrix converter and the power router attached to its output. Both are 3-phase input/output systems. The switch groups for state 1 and 2 of Table 5.1 are also obvious.

2) the loads are connected to a different input source and they successfully continue to operate. Table 5.1 summarizes this scenario.

A photograph of the experimental prototype power router is shown in Fig 5.3. The line connections of the power cables are also schematically presented. Power router has 4 inputs and 8 outputs and each input can be programmed to be outputted at one of its equivalent two outputs. Power line communication (PLC), which is the black box in the photograph, is used for controlling the power router through a personal computer. As Fig. 5.3 shows, a power router input is considered to be a matrix converter output phase-to-phase voltage. When switching is performed such that a line is considered to fail, the equivalent phase-to-phase voltage is not reproduced at the output of the power router. The power router specifications are a

maximum operating voltage of 100–200 V_{rms} , continuous maximum power of 1 kW, and with Si-MOSFETs implemented as switches (450 V, 17 A). The following experimental results although performed in test level voltages, they can be scaled to higher voltage setup when the device ratings and power capacities are increased.

The matrix converter utilizes the Venturini control modulation described in previous chapter. This modulation creates an output voltage via the feedback of the input and target output voltages. As it was mentioned in the beginning, PET usually performs medium level voltage transformation into low level voltage (e.g. 1 kV to 100 V). In this thesis, since the limitation of facilities at high voltage in laboratory, test level voltages are applied. As a result for the sake of equivalency in the experimental setup, the input voltage is set to 10 V and the voltage ratio of the matrix converter is set to 0.1

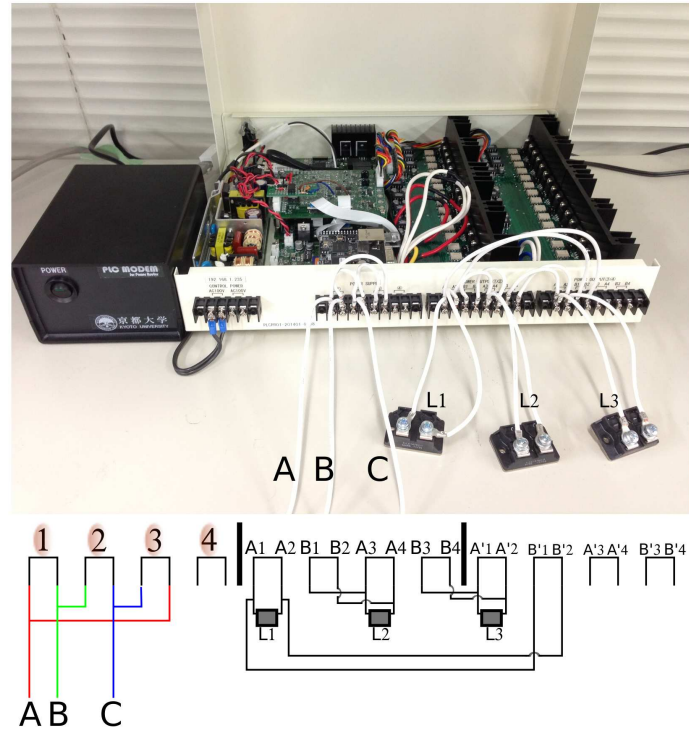


Figure 5.3: Experimental prototype power router and connection setup of input and output phases. This power router can be fed with up to 4 input sources and has 8 outputs. For example, input 1 can be outputted at port A1-A2 or B1-B2 by the equivalent control. The last input of the power router is unconnected since 3-phase switching is desired.

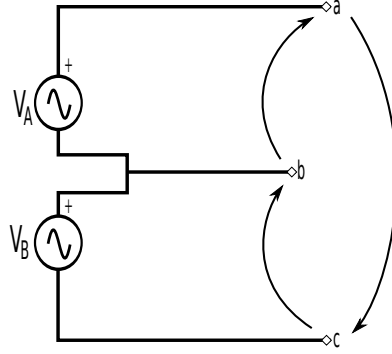


Figure 5.4: Experimental 3-phase source. It can be succeeded with the V-connection of two power sources. Power amplifiers driven by two function generators are used for the experiment.

so that the output voltage of the converter is 1 V. Keeping the generality of discussion, let us consider the system base for both experiment and simulation results represented in per unit quantities. The LC filters are included in order to cut off any high frequency harmonics and are set as follows: $L=33$ mH, $C=180$ μ F, $\text{Load}_{1,2,3}=15$ Ω with the line resistances of a few Ohms for the sake of device protection. The switching frequency is set to 24.4 kHz and the pulses are digitally created utilizing the FPGA digital board.

Last but not least, Fig. 5.4 presents how the 3-phase source is implemented in the experiment. As mentioned in previous chapter, only two voltage sources are used in V-connection as shown in the figure. If we assume that $V_A = V_{\max} \sin(\omega t)$ and $V_B = V_{\max} \sin(\omega t + \frac{2\pi}{3})$ then V_C can be calculated as in Eq. (5.1). The correct phase for a balanced sinusoidal voltage source as far as the phases are concerned can be proved.

$$\begin{aligned}
 V_{ca} &= -(V_{ab} + V_{bc}) = -V_{\max}(\sin(\omega t) + \sin(\omega t + \frac{2\pi}{3})) = \\
 &= -V_{\max}(\sin(\omega t) \sin \frac{\pi}{6} + \cos(\omega t) \cos \frac{\pi}{6}) = \\
 &= -V_{\max} \cos(\omega t - \frac{\pi}{6}) = V_{\max} \sin(\omega t - \frac{2\pi}{3})
 \end{aligned} \tag{5.1}$$

5.3 Experimental and simulation results

In the beginning, the scenario discussed in the previous section will be presented. It is a 3-phase switching during which all the loads are connected to different inputs. In particular, Table 5.1 shows load 1 which is initially

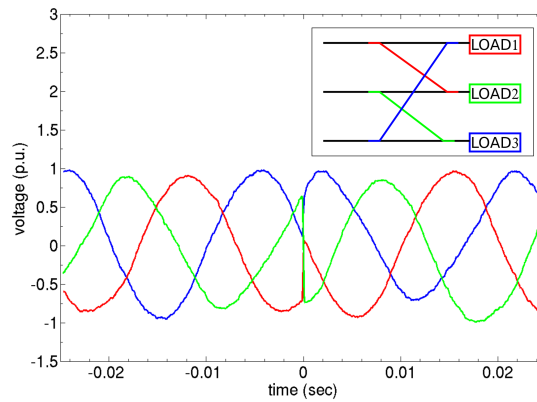


Figure 5.5: 3-phase switching based on Table 5.1. The loads are fed with power but from different sources after power routing.

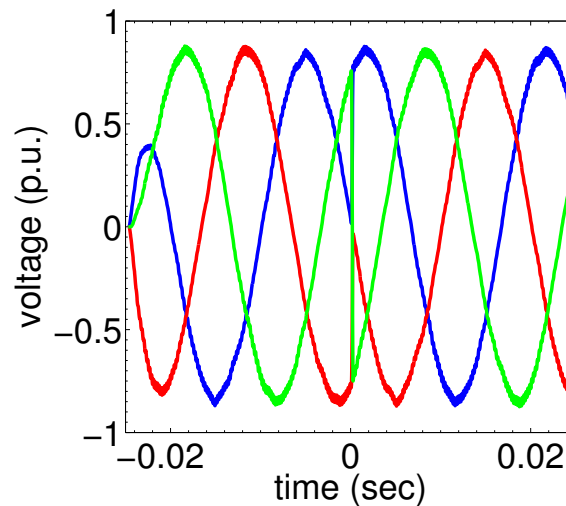


Figure 5.6: Simulation verification for the experimental result of Fig. 5.5. There is good correspondence between the two methods.

connected to phase AB, but after switching it is connected to phase CA. Load 2 switches from BC to AB, and load 3 switches from CA to BC. The experimental results are shown in Fig. 5.5. In the small circuit diagram, the colored lines indicate the line connections after switching and refer to the phase-to-phase voltages. The experimental result is also confirmed from the simulations in Fig. 5.6. If the practical system is considered (medium level voltage at 1 kV and low level voltage at 100 V) then 1 p.u. corresponds to 100 V. The simulations are generated from a Simulink Matlab model based

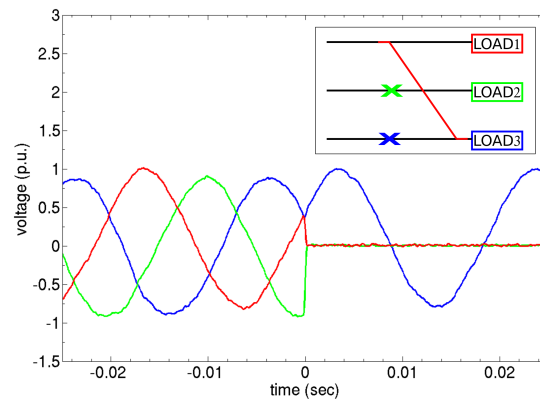


Figure 5.7: Switching with one critical load and failure in 2 power router outputs. The critical load is successfully fed with power.

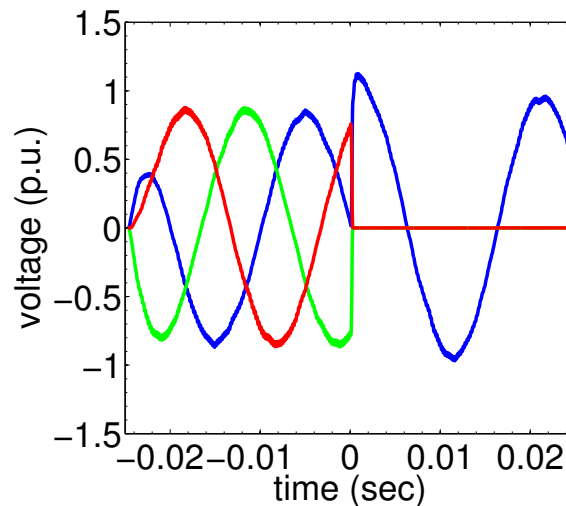


Figure 5.8: Simulation verification of Fig. 5.7. Small transients at the moment of switching caused by resonances between the power router and matrix converter output filter.

on Fig. 5.2.

Various switching scenarios were further tested. Instead of a phase-to-phase voltage from now on, we will just refer to phase A, B, and C for the sake of simplicity. For the case of a critical load in phase C (load 3), phases B and C are disconnected from the output representative of a system failure. In this case, switching between phases A and C should take place as shown in Fig. 5.7. The voltage has been maintained at output C as a result of

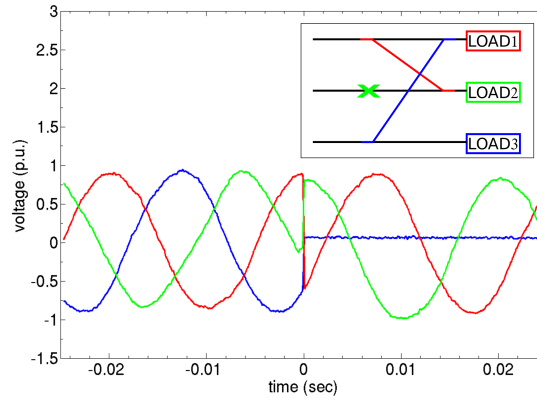


Figure 5.9: Experimental switching with two line switchings. This scenario describes the experimental power switching in a 3-phase load while there is one failure in a power router output and two line switchings.

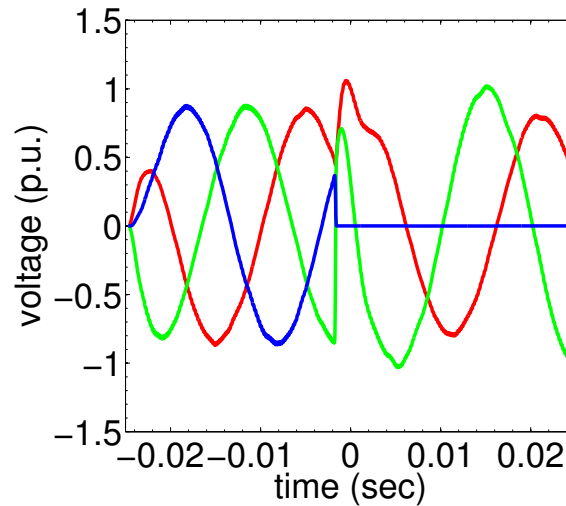


Figure 5.10: Simulation verification of Fig. 5.9. The transients become apparent at the moment of switching. Line resistances in the experimental power router inputs were implemented to ensure safe operation.

the successful power routing. Verification of the experiment is shown in the simulation of Fig. 5.8. There is a small overvoltage in the output of power router after the moment of switching, which is possibly due to a resonance between the power router and the output filter of the matrix converter. On the other hand, some line resistances have been installed in the experimental power router input for its protection and also for the suppression of such

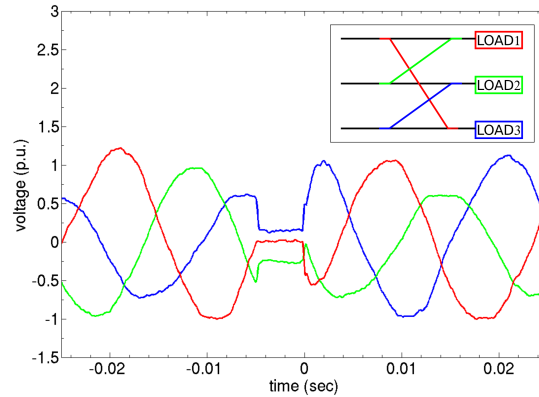


Figure 5.11: Experimental power routing for unbalanced sources. Power router can successfully make the switching but there is a characteristic delay between switching caused by this voltage imbalance.

kind of undesired transients.

The final switching scenario is as shown in Fig. 5.9. In this case, phase B fails but load 2 is successfully fed with power due to switching with phase A. On the other hand, phase C feeds load 1 in phase A after power switching. In this case, load 3 has no power but the other two loads are successfully functioning. The transients are more obvious here, as shown in Fig. 5.10 simulation results. Currents show similar behavior since we are experimenting with resistive loads.

In general, power router realises the switching between two input lines at the moment when the two powers of these lines are equal to achieve soft-switching techniques in order to reduce the power losses. During the above experiments however, several switchings are simultaneously performed so that hard-switching was also implemented. The Simulink model implements hard-switching techniques in all cases.

Future studies should include the investigation of new control methods with faster and lower power loss switching, as well as power routing with both DC and AC sources. Investigation of unbalanced input sources is also of great importance as the majority of loads throughout the grid is unbalanced. The matrix converter creates an unbalanced output supply and power routing is performed as shown in Fig. 5.11. There is also a characteristic delay between the switching due to the fact that the power router is unable to function properly for some msec due to the voltage imbalance (i.e.,

power imbalance), but in the end it performs the necessary switchings. We are currently working on such topics such as this delay reduction in order to reduce the switching losses. In addition, the control modulation should cooperate with the power router so that matrix converter can create the desired voltage amplitude and phase correction according to the power need of each load. The main next topic is the inclusion of a PET in this system and the investigation of dynamics of the overall system.

5.4 Summary and discussion

An experimental prototype power router was used with a direct AC/AC matrix converter in various testing conditions. The balanced voltage switching scenarios performed satisfactorily, but on the other hand the unbalanced ones showed inability for quick transition. Such issues should be further studied in future research. Figure 5.12 shows a photograph of the complete experimental apparatus. Two power amplifiers (NF4502) driven by

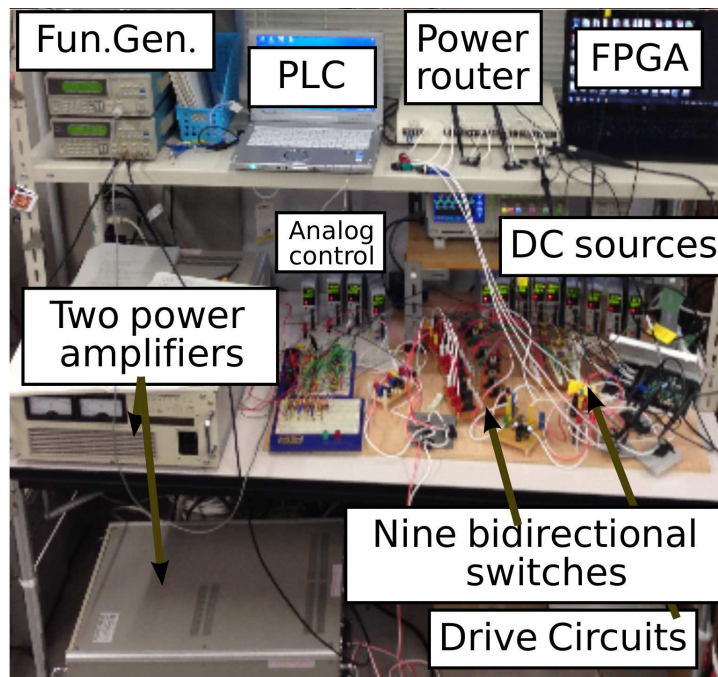


Figure 5.12: Experimental unified apparatus. Power router, matrix converter, power amplifiers for the input source, PCs for the control of PLC and FPGA are the major components of this experiment.

the function generators are shown on the left part of the figure. Two personal computers are needed for the PLC and FPGA, respectively but the second one can be omitted if the VHDL program is stored to the memory of the digital board. Nine DC sources are shown in the middle right part of the figure which are used for the nine bidirectional switches. The advantage of the common source bidirectional switch topology is clearly depicted here, since the common drain topology would have required double the amount of DC sources. The scale of the unified apparatus is relatively big but every part of it is composed by simple power and logic circuits. By using, however, new materials such as SiC semiconductors limitation like switching frequency and efficiency can be overcome. As a result, new state of the art devices are created.

6

Conclusion

‘ Πάντα κατ’ ἀριθμὸν γίνονται — *All is number* ’

– Pythagoras (570 B.C. – 495 B.C.)

6.1 Attainments

In this dissertation AC/AC conversion was variously studied with simulation and experimental methods. In the beginning some fundamentals of AC/AC conversion were studied. Special attention was paid to the harmonic content in steady state as well as in the transient behavior due to the switching frequency impact. It was shown that higher switching frequency can bring smaller amount of harmonics and create faster transients.

The primary achievement is the converter investigation in the nonlinear dynamics field by using nonlinear iterative maps. It was shown that besides the steady state, other operation regimes exist such as period doubling and chaotic oscillations. It was proven that these motions can bring great advantages such as harmonic elimination and performance improvement. To the best of author’s knowledge the nonlinear aspect of the AC/AC conversion hasn’t yet been studied thoroughly from the literature such as the DC/DC conversion.

A 3-phase AC/AC converter, also known as matrix converter, was tested in the following chapters. The dynamic model might be based on literature but on the other hand several results were presented, pointing new advantages of the matrix converter such as resonances that could bring higher efficiency but also disadvantages such as the inverse relationship between

switching frequency and efficiency. To this end, new devices such as the SiC ones can increase the switching frequency more and optimise the operation. In other words, simple circuits were investigated but with the implementation of new devices [100], new frontiers can be succeeded such as optimised control, smaller and compact sizes, agile functionality etc.

The last achievement of this work was the assembly of a matrix converter with a power router. Various switching scenarios proved that there is possibility for on-demand power supply and the realisation of a local power network system is possible. This application aimed towards a more efficient power delivery and a “smarter” smart-grid.

6.2 Future work

As for the nonlinear model, future work should include the study of the behavior on transient state and also the ability to control the chaotic regimes by driving them to stable operations. In other words, operating under specific control mechanisms, the converter could switch easily and faster to other frequencies since the chaotic regimes contain many periodic states. As it is shown at Fig. 6.1 through the randomness of the chaotic data the desired frequency can be acquired if the appropriate control is implemented. Thus,

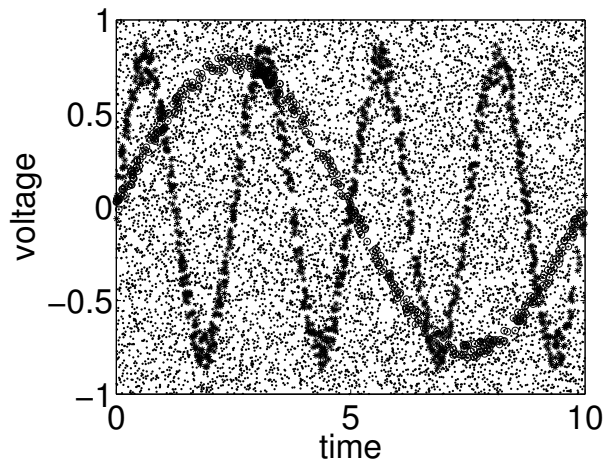


Figure 6.1: Stability through chaos. Representation of the desired frequency that can be acquired through the simulated chaotic data with the appropriate control. Circled dots represent a fundamental sinusoidal signal and the starred ones represent one signal with higher frequency.

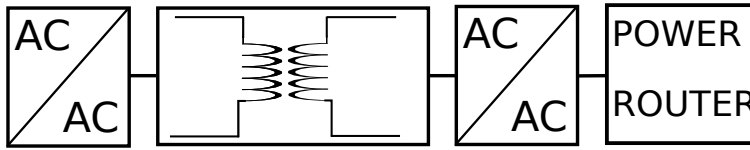


Figure 6.2: Assembly of future power electronic transformer. The AC/AC converters create a high frequency link wherein a compact transformer can be installed. Various power routers can be connected to the converters to achieve localized power control.

a multi-frequency converter could also be succeeded. This also would be beneficial if the future power-grids don't depend on a single line frequency but operate in a wide range of different frequencies. Special attention should be given to the control of the closed-loop feedback control. If all-digital control is implemented, the choice of the controllable parameters would be an easier task and also the accuracy will be increased. Thus, moving along the different operations of Fig. 3.10 will be successfully performed in detail.

Efficiency of the experimental matrix converter by introducing snubber circuits, more efficient drive circuits and control modulations should be increased in the future studies. In addition, operating the matrix converter with high output line frequency is the next step towards the realisation of the power electronic transformer.

The future works related to power router include faster switching times by introducing novel control modulations and SiC devices. Finally, the introduction of the power electronic transformer and the investigation of the complete overall system would be the final step of this interesting and rich research topic. Such a system is shown in Fig. 6.2. The AC/AC converters create a high frequency link wherein a PET can be installed. The experimental investigation of such an apparatus will be of great importance and interest. Power routers can also be attached to the converters as Fig. 6.2 shows in order to further modulate the converter outputs and distribute on-demand power.

Appendix A

Open loop 1-phase AC/AC converter

The experimental setup is shown in Fig. A.1. For safety reasons the power circuit is connected with a circuit breaker (Panasonic BS1110, AC 100 V, 5 A). A variable transformer (61-18136 Yamabishi, 100 V input, 0-130 V output, 3 A, 0.3 KVA, Type V-130-3, 50/60 Hz) is used which can regulate its output voltage. For the sign of the input voltage an isolation transformer (Osaka Koha, HF-10) is used in order to isolate the power circuit from the control circuit. A voltage comparator (OPA227P) can compare the input voltage with the ground and as a result a pulse can be created which shows when the input voltage is positive (high level voltage) or negative (low level voltage). This pulse is used by the field programmable gate array (FPGA) digital board (Digilent Nexys 3, Spartan 6 chip) in order to create the four pulses with the desired switching frequency. As it is shown in this figure the level of the output voltage is only 3.3 V. That is the reason we need to implement two drive circuits (ADuM1233 & Si8235 were tested). These drive circuits can increase the level of the voltage and also isolate their input from their output. Since the bidirectional switches have common source topology, their common source is used as the ground of the drive circuit pulses. That is the reason why we can use one drive circuit for two power MOSFETs (STW13NK100Z, n-channel, supermesh, 1000 V, 13 A) of the same bidirectional switch.

Other measurement instruments and equipment that have been used for this dissertation experiments are presented in Table A.1.

Table A.1: Measurement instruments.

Instrument	Description
Tektronix TPS2024	4 channel digital storage oscilloscope
Tektronix AFG320/310/3022B	arbitrary function generators
Tektronix TCPA300 Amplifier	AC/DC current probe
Lem Heme	20 A RMS, current probe
Matsusada P4K18-2	DC power supplies
Texio PA36-3B	DC power supplies
Agilent 4294A	40Hz-110MHz impedance analyzer
Iwatsu IE-1198	curve tracer
Hioki 3522	LCR HiTester

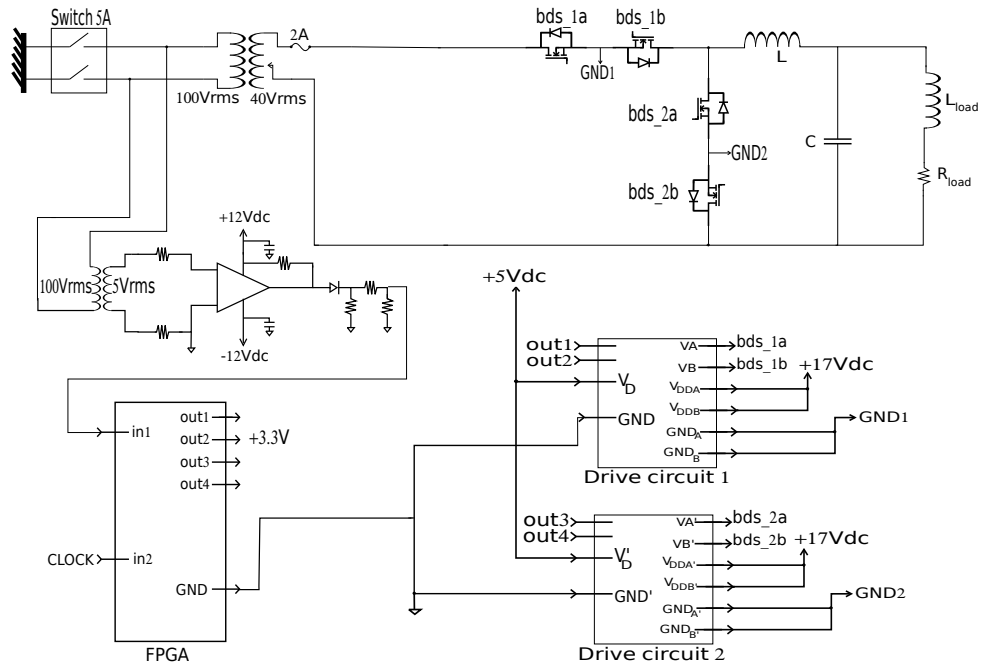


Figure A.1: Experimental layout for the 1-phase converter with open-loop control.

Appendix B

Pulses dead-time

For safety reasons dead-time has to be implemented between the two pulses of the two bidirectional switches. This is mainly achieved with the introduction of some logic devices and more specifically NOT and NAND gates (SN7404N & SN7400N integrated circuits).

As Fig. B.1 depicts with the implementation of the logic gates and a simple RC circuit the dead-time is achieved as shown in Fig. B.2. Actually the time constant is achieved by the product RC. In this work 20 k Ω and 200 pF were used giving as a result a time constant equal to 4 μ sec.

This is an important part of the control because short circuit phenomena could be avoided. Additionally a capacitor of 0.1 μ F has been implemented parallel with the DC sources to avoid ringing phenomena and achieve better stabilisation of the input source. The disadvantage of this method is that there is a small period of time where an open circuit is created and as a result we lose a small percentage of output power. Credit for the dead-time circuit implementation should be given to Dr. M. Minami [101].

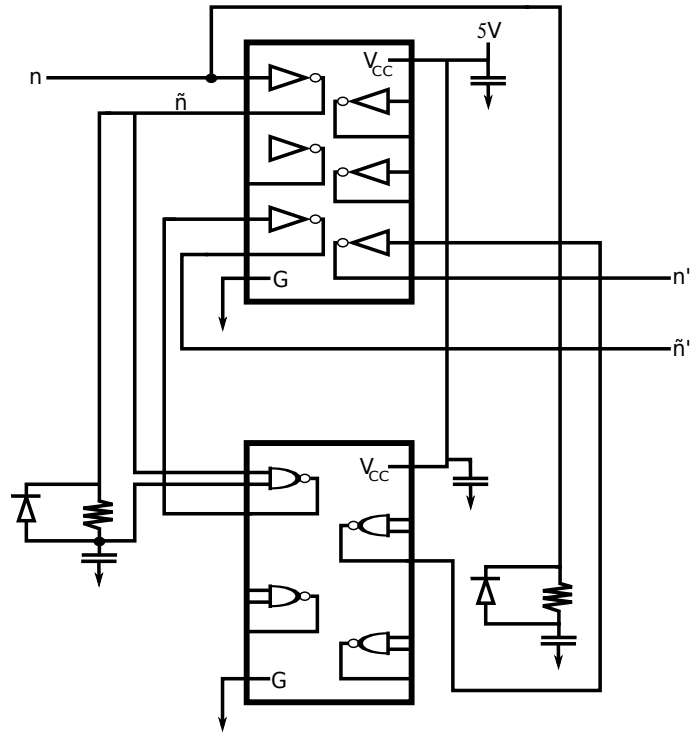


Figure B.1: Dead-time experimental implementation. It can be achieved with logic gates and the time constant for the delay can be given by the product RC .

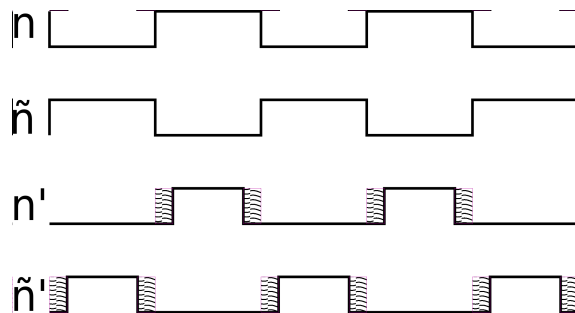


Figure B.2: Dead-time output result. n' and \tilde{n}' can be used directly to the switches.

Appendix C

Closed-loop feedback control

Chapter 3 implements output voltage feedback control. The proportional feedback control is illustrated at Fig. 3.2. Figure C.1 presents the various experimental topologies.

The first one is called the all analogue one. In this one we are using operation amplifiers and resistances to create Eq. (3.7). This equation can be represented as well as in Eq. (C.1). The first amplifiers can find the difference between the two voltages, the second one adds a dc voltage to the output and the third one compares the final duty cycle with a triangular voltage in order to create the PWM pulse which will be driven to the switches. This is an easy way to implement but the drawback is that the parameter accuracy is quite low due to the fixed values of the resistances.

$$d = -\left(-0.6 \frac{R}{R} + \frac{R}{R} \left(\frac{R_2}{R_1}(u - V_{\text{ref}})\right)\right) = 0.6 - \frac{R_2}{R_1}(u - V_{\text{ref}}) \quad (\text{C.1})$$

The next method that was implemented is the dSpace-based one. dSpace is a digital machine that is connected with a personal computer where the control model can be easily implemented with Simulink. On the other hand, the disadvantage of this method is that dSpace sampling time is not high enough. As a result, higher switching frequencies can't be implemented. The third one is a suggestion for future studies. It is an all-digital implementation based on the FPGA digital board. By this way, it is estimated that the change of the parameter values will be more accurate, faster, and also higher switching frequencies will be easily created.

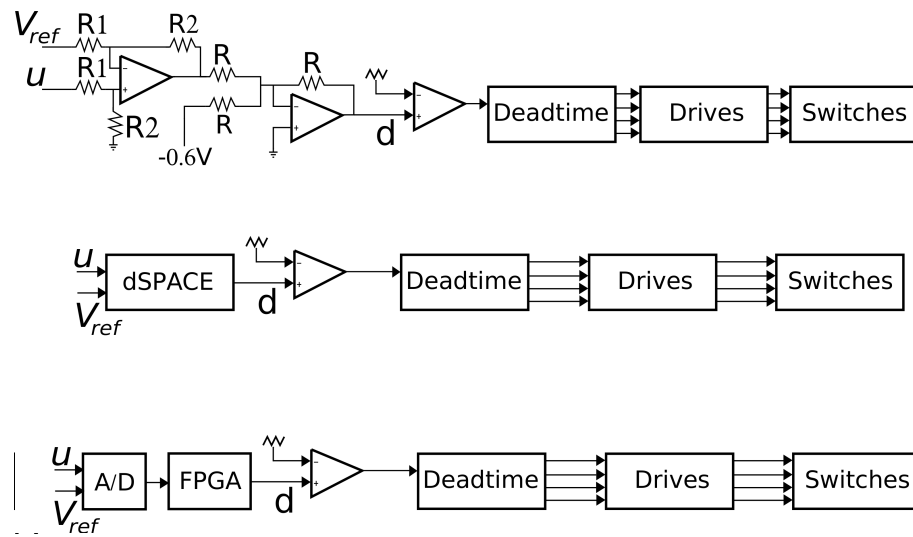


Figure C.1: Closed-loop feedback topologies. All analogue, dSpace-based, and all-digital are the three proposals in order to realise the experimental feedback control.

Appendix D

Iterative map

The analytical solutions of Eq. (3.1) will be given in detail in this Appendix. First of all the list of assignments follows:

- $\frac{1}{\omega RC} = 2\zeta$
- $\frac{1}{\omega\sqrt{LC}} = \omega_o$
- $\sqrt{\omega_o^2 - \zeta^2} = \rho$
- $A' = \frac{1}{\omega_o^2}$
- $B' = -\frac{1}{\omega_o^2}$
- $C' = -\frac{2\zeta}{\omega_o^2}$
- $A = \frac{-(1-\omega_o^2)}{(1-\omega_o^2)^2+4\zeta^2}$
- $B = \frac{A2\zeta}{1-\omega_o^2}$
- $C = 1 - A\omega_o^2$
- $D = -B$
- $M_1 = \frac{1}{\omega_o^2}$
- $M_2 = \frac{-2\zeta}{4\zeta^2+(\omega_o^2-1)^2}$
- $M_3 = \frac{-(\omega_o^2-1)}{4\zeta^2+(\omega_o^2-1)^2}$
- $M_4 = -2\zeta M_1 - \omega_o^2 M_2$
- $M_5 = -M_1 - M_3$

For the off-state of the converter the solution of Eq. (3.2) is given by Eq. (D.1) where x_1 and x_2 are the state variables for current and voltage, respectively.

$$\left\{ \begin{array}{l} x_1(t) = -\omega_o^2 x_1(t_n) \left[\frac{1}{\omega_o^2} - \frac{1}{\omega_o^2} \left(\frac{-\zeta}{\rho} e^{-\zeta t} \sin(\rho t) + e^{-\zeta t} \cos(\rho t) \right. \right. \\ \left. \left. - \frac{\omega_o^2}{2\zeta} \frac{1}{\rho} e^{-\zeta t} \sin(\rho t) \right) \right] - \frac{2\zeta}{\omega_o^2 \rho} x_2(t_n) e^{-\zeta t} \sin(\rho t) + x_1(t_n) \\ x_2(t) = 2\zeta x_1(t_n) \frac{1}{\rho} e^{-\zeta t} \sin(\rho t) + x_2(t_n) \left[-\frac{\zeta}{\rho} e^{-\zeta t} \sin(\rho t) + e^{-\zeta t} \cos(\rho t) \right] \end{array} \right. \quad (\text{D.1})$$

The substitutions of Eq. (3.3) are shown in Eq. (D.2).

$$\left\{ \begin{array}{l} x_1(t_{n'}) = -\omega_o^2 x_1(t_n) \left[\frac{1}{\omega_o^2} - \frac{1}{\omega_o^2} \left(\frac{-\zeta}{\rho} e^{-\zeta(1-d)T} \sin(\rho(1-d)T) \right. \right. \\ \left. \left. + e^{-\zeta(1-d)T} \cos(\rho(1-d)T) - \frac{\omega_o^2}{2\zeta} \frac{1}{\rho} e^{-\zeta(1-d)T} \sin(\rho(1-d)T) \right) \right] \\ \left. - \frac{2\zeta}{\omega_o^2 \rho} x_2(t_n) e^{-\zeta(1-d)T} \sin(\rho(1-d)T) + x_1(t_n) \right. \\ x_2(t_{n'}) = 2\zeta x_1(t_n) \frac{1}{\rho} e^{-\zeta(1-d)T} \sin(\rho(1-d)T) \\ \left. + x_2(t_n) \left[-\frac{\zeta}{\rho} e^{-\zeta(1-d)T} \sin(\rho(1-d)T) + e^{-\zeta(1-d)T} \cos(\rho(1-d)T) \right] \end{array} \right. \quad (\text{D.2})$$

$$\left\{ \begin{array}{l} x_1(t) = -\frac{\omega_o^2}{2\zeta} \left[\omega_o^2 \left(M_1 + M_2 \sin(t) + M_3 \cos(t) + M_4 \frac{1}{\rho} e^{-\zeta t} \sin(\rho t) \right. \right. \\ \left. \left. + M_5 \left(-\frac{\zeta}{\rho} e^{\zeta t} \sin(\rho t) + e^{-\zeta t} \cos(\rho t) \right) \right) \right. \\ \left. + 2\zeta x_1(t_{n'}) \left(A' + B' \left(-\frac{\zeta}{\rho} e^{-\zeta t} \sin(\rho t) + e^{-\zeta t} \cos(\rho t) \right) + C' \frac{1}{\rho} e^{-\zeta t} \sin(\rho t) \right) \right. \\ \left. + x_2(t_{n'}) \frac{1}{\rho} e^{-\zeta t} \sin(\rho t) \right] + \frac{\omega_o^2}{2\zeta} (1 - \cos(t)) + x_1(t_{n'}) \\ x_2(t) = \omega_o^2 \left[A \sin(t) + B \cos(t) + C \frac{1}{\rho} e^{-\zeta t} \sin(\rho t) + D \left(-\frac{\zeta}{\rho} e^{\zeta t} \sin(\rho t) \right. \right. \\ \left. \left. + e^{\zeta t} \cos(\rho t) \right) \right] + 2\zeta x_1(t_{n'}) \left(\frac{1}{\rho} e^{-\zeta t} \sin(\rho t) \right) \\ \left. + x_2(t_{n'}) \left(-\frac{\zeta}{\rho} e^{-\zeta t} \sin(\rho t) + e^{-\zeta t} \cos(\rho t) \right) \end{array} \right. \quad (\text{D.3})$$

The equations for the on-state of the converter follows. When the equation system of Eq. (3.1) is solved during the on-state the Eq. (3.4) takes the analytical form of Eq. (D.3). The substitutions of Eq. (3.5) are shown in Eq. (D.4).

$$\left\{ \begin{array}{l} x_1(t_{n+1}) = -\frac{\omega_o^2}{2\zeta} \left[\omega_o^2 \left(M_1 + M_2 \sin(dT) + M_3 \cos(dT) + M_4 \frac{1}{\rho} e^{-\zeta dT} \sin(\rho dT) \right. \right. \\ \quad \left. \left. + M_5 \left(-\frac{\zeta}{\rho} e^{\zeta dT} \sin(\rho dT) + e^{-\zeta dT} \cos(\rho dT) \right) \right) \right. \\ \quad \left. + 2\zeta x_1(t_{n'}) \left(A' + B' \left(-\frac{\zeta}{\rho} e^{-\zeta dT} \sin(\rho dT) + e^{-\zeta dT} \cos(\rho dT) \right) + C' \frac{1}{\rho} e^{-\zeta dT} \sin(\rho dT) \right) \right. \\ \quad \left. \left. + x_2(t_{n'}) \frac{1}{\rho} e^{-\zeta dT} \sin(\rho dT) \right] + \frac{\omega_o^2}{2\zeta} (1 - \cos(dT)) + x_1(t_{n'}) \right. \\ \\ x_2(t_{n+1}) = \omega_o^2 \left[A \sin(dT) + B \cos(dT) + C \frac{1}{\rho} e^{-\zeta dT} \sin(\rho dT) \right. \\ \quad \left. + D \left(-\frac{\zeta}{\rho} e^{\zeta dT} \sin(\rho dT) + e^{\zeta dT} \cos(\rho dT) \right) \right] + 2\zeta x_1(t_{n'}) \left(\frac{1}{\rho} e^{-\zeta dT} \sin(\rho dT) \right) \\ \quad \left. + x_2(t_{n'}) \left(-\frac{\zeta}{\rho} e^{-\zeta dT} \sin(\rho dT) + e^{-\zeta dT} \cos(\rho dT) \right) \right] \end{array} \right. \quad (\text{D.4})$$

The final iterative map of Eq. (3.6) can be derived by the use of Eqs. (D.2) and (D.4). Bare in mind that duty cycle has to be transferred into the discrete time domain which is not shown in the above equations in order to make them more compact. This duty cycle value can be found from Eq. (D.5), where E_m is the amplitude of the reference voltage.

$$d(t_n) = D - k(x_2(t_n) - E_m \sin(t_n)) \quad (\text{D.5})$$

Appendix E

Space vector modulation

An easy graphical representation of determining if two switching states are the same is presented in this Appendix. As it was shown in Chapter 4, the space vector for the current lies on six sextants and the voltage one to its equivalent sextants. Therefore, there are 36 possible switching states. However, only 18 states are available. If it is assumed that the voltage vector lies on the x-y horizontal plane and the current vector to an equivalent perpendicular plane, then the three-dimensional Fig. E.1 can be created. By moving amongst these vectors the final state of the converter can be determined.

Let's take for example the situation where the voltage space vector lies

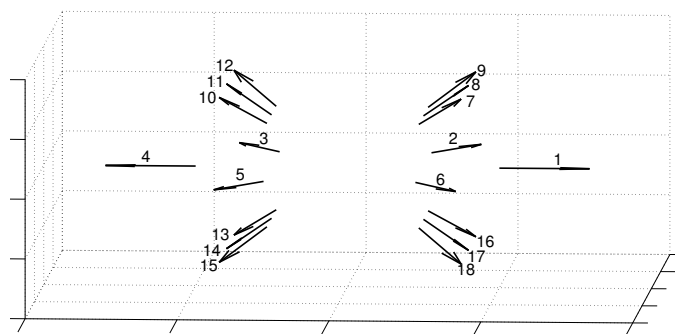


Figure E.1: Three-dimensional representation of the 18 switching states of the space vector modulation. The voltage space vector is moving in the horizontal plane, while the other states are decided by the current space vector.

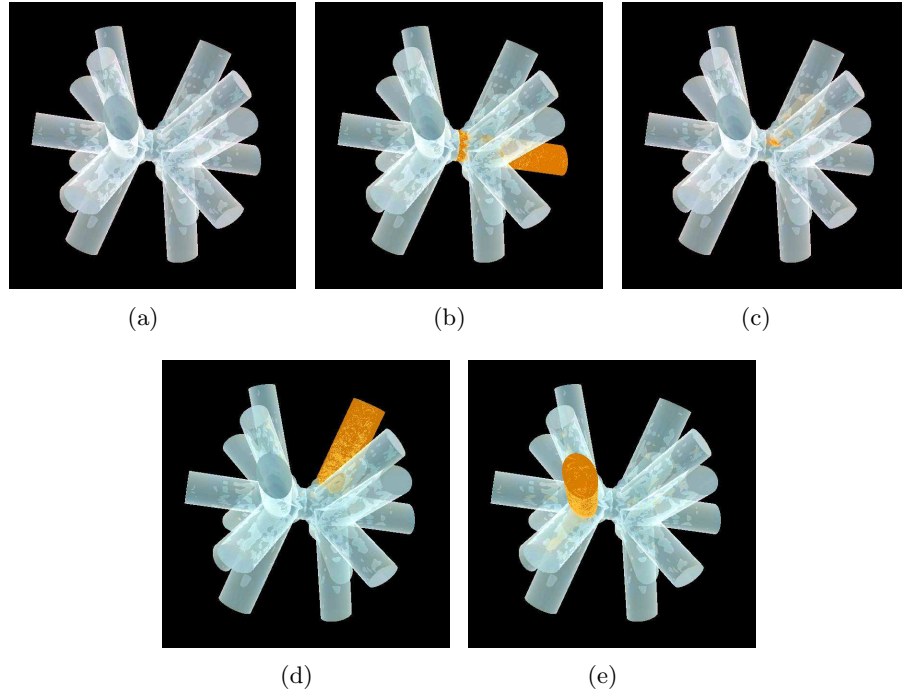


Figure E.2: Switching state example 1. The voltage space vector lies on the second sextant while the current space vector lies on the third sextant.

on the second sextant and the current space vector on the third sextant. In Fig. E.2 (a) to (c) the two steps for the voltage space vector are performed on the horizontal plane. By keeping this state as reference, three vectors are counted to the equivalent perpendicular plane as in Fig. E.2 (d) and (e). This is the final state in our 3-D diagram. If another state is chosen such as the voltage space vectors lies on the fifth sextant and the current space vector lies on the sixth sextant the equivalent procedure should take place as shown in Fig. E.3. We can see that this final state is the same as the one of the previous example (Fig. E.2 (e) & Fig. E.3 (k)). In other words, it can be concluded that these states have the same switching state and they are equivalent.

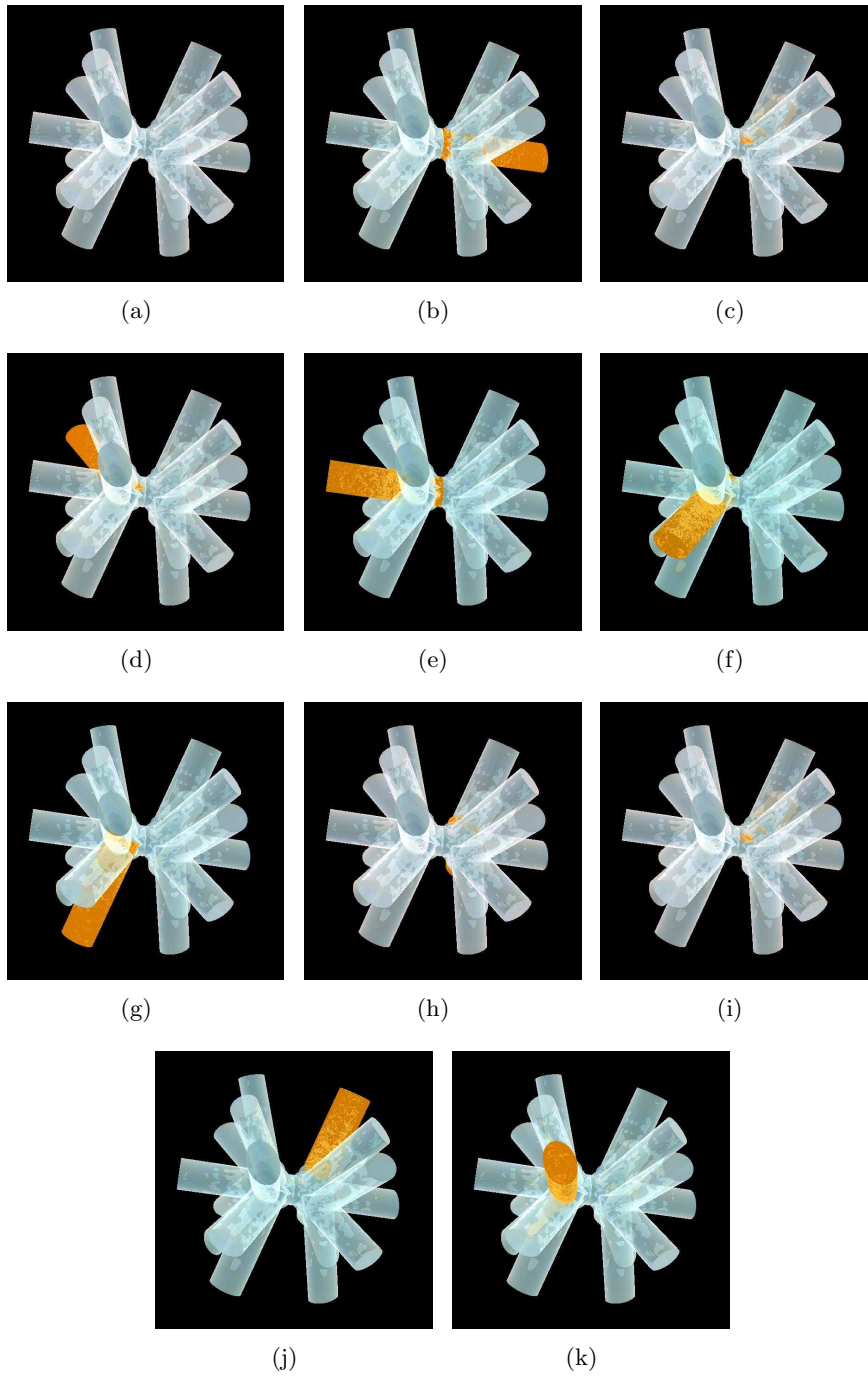


Figure E.3: Switching state example 1. The voltage space vector lies on the fifth sextant while the current space vector lies on the sixth sextant. The final state is the same with the switching example 1 of Fig. E.2, fact that means the two examples are equivalent.

Appendix F

Matrix converter control

Various parts of the matrix converter circuit will be explained in this Appendix. First of all, the output target 3-phase voltage is explained in Fig. F.1. The first and second amplifiers are inverting the input voltage. R_1 and C_1 create the phase difference and as a result we can create the 240 degrees phase. From the above two signals with the use of one more amplifier a voltage phase difference of 120 degrees can be achieved. In order to achieve 50 Hz of output signals the red resistance is set at 5.6 k Ω , capacitance at 1000 nF and all the other resistances at 10 k Ω .

The input voltage must be measured and we have used an LA25NP-SP14 current sensor for accurate measurement which is wired as Fig. F.2 shows. This current transducer provides galvanic isolation and it is quite easy to use. A resistance of 100 Ω is used parallel to its output. The output contains a DC harmonic which is undesired for our control modulation therefore a high pass RC filter is used (4 k Ω , 1 μ F).

The target output voltages and the measured input voltages should be multiplied in order to define the final duty cycle and achieve Eq. (4.3). For that reason, multipliers integrated circuits have been introduced such as ADS34JDZ as shown in Fig. F.3. In order to achieve scale 1 for the multiplication the red resistance is set at 90 k Ω , the black one at 10 k Ω , and the capacitance value at 200 pF.

The nine pulses for the bidirectional switches are created from the FPGA and are connected to nine optocouplers (TLP250). This is a simpler drive circuit than the Si8235 and its schematic is presented in Fig. F.4. From output 6 of the drive circuit the pulse can be driven to the gates of the switches.

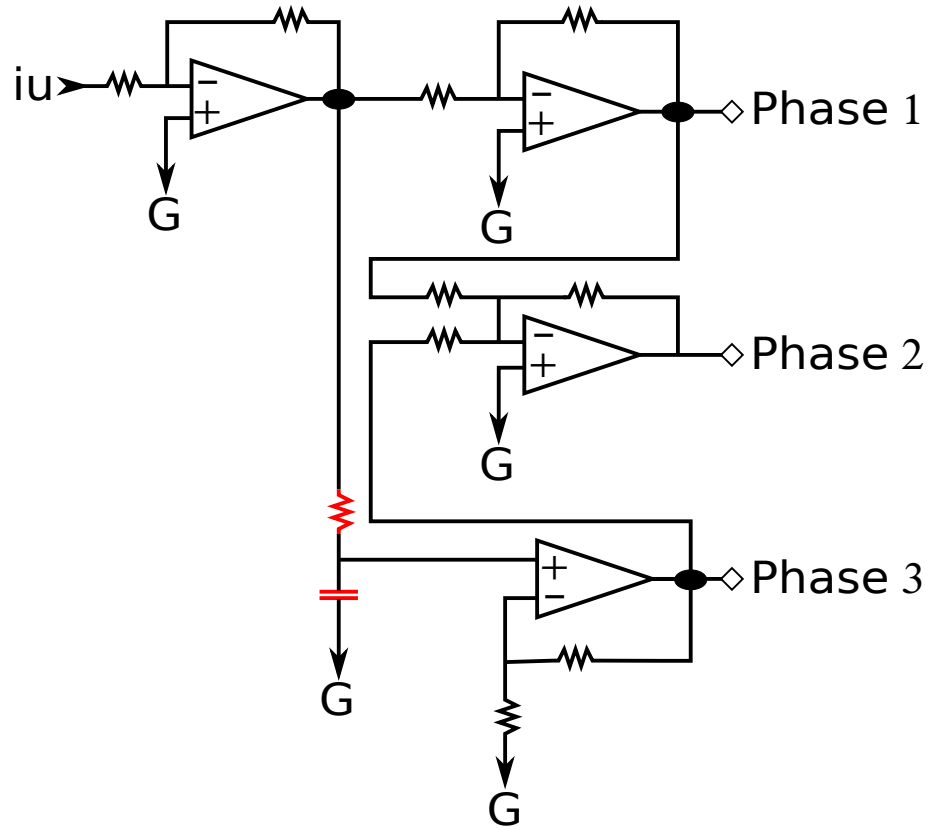


Figure F.1: Low voltage 3-phase source implementation with the use of 4 operational amplifiers.

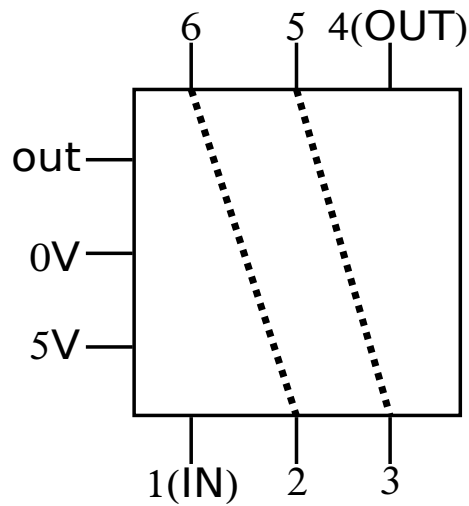


Figure F.2: Current sensor schematic of LA25NP-SP14.

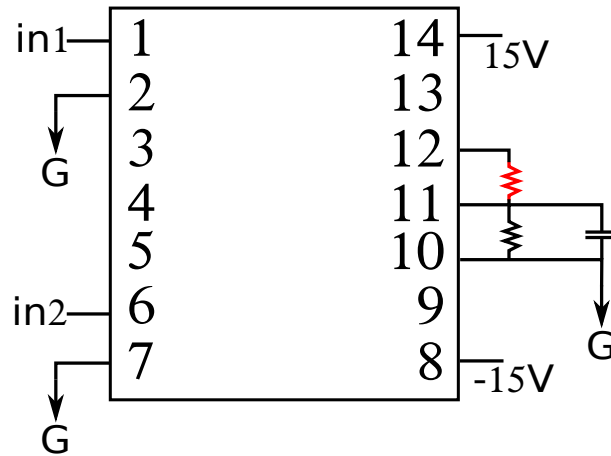


Figure F.3: Signal multiplier schematic of ADS34JDZ.

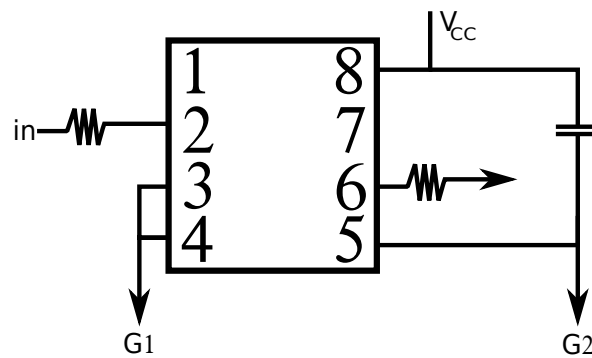


Figure F.4: Optocoupler schematic of TLP250. It is a more simple drive circuit but it can't achieve higher frequencies.

Bibliography

- [1] J. W. Motto, *Introduction to solid state power electronics*. Westinghouse Electric Corporation, 1977.
- [2] H. R. II, “Mercury arc current converters,” *London, England: Pitman*, 1935.
- [3] F. Gutzwiller, “Thyristors and rectifier diodes—the semiconductor workhorses,” *Spectrum, IEEE*, vol. 4, no. 8, pp. 102–111, 1967.
- [4] W. E. Newell, “Power electronics—emerging from limbo,” *IEEE Transactions on Industry Applications*, no. 1, pp. 7–11, 1974.
- [5] D. Czarkowski and M. K. Kazimierczuk, “Energy-conservation approach to modeling PWM DC-DC converters,” *IEEE Transactions on Aerospace and Electronic Systems*, vol. 29, no. 3, pp. 1059–1063, 1993.
- [6] K. Tsang and W. Chan, “Cascade controller for DC/DC buck converter,” in *IEE Proceedings on Electric Power Applications*, vol. 152, no. 4. IET, 2005, pp. 827–831.
- [7] K. Mehran, D. Giaouris, and B. Zahawi, “Modeling and stability analysis of DC-DC buck converter via Takagi-Sugeno fuzzy approach,” in *3rd International Conference on Intelligent System and Knowledge Engineering, ISKE 2008*, vol. 1. IEEE, 2008, pp. 401–406.
- [8] S. Bhowmik and R. Spee, “A guide to the application-oriented selection of AC/AC converter topologies,” in *7th Annual Applied Power Electronics Conference and Exposition, APEC’92. Conference Proceedings 1992*. IEEE, 1992, pp. 571–578.
- [9] A. Fatemi, M. Azizi, K. Rahmani, M. Mohamadian, and A. Yazdian, “A novel reduced switch count multilevel AC/AC converter,” in *19th*

- Iranian Conference on Electrical Engineering (ICEE)*. IEEE, 2011, pp. 1–5.
- [10] T. Wijekoon, C. Klumpner, P. Zanchetta, and P. W. Wheeler, “Implementation of a hybrid AC–AC direct power converter with unity voltage transfer,” *IEEE Transactions on Power Electronics*, vol. 23, no. 4, pp. 1918–1926, 2008.
- [11] P. Sanchis, A. Ursæa, E. Gubia, and L. Marroyo, “Boost DC-AC inverter: a new control strategy,” *IEEE Transactions on Power Electronics*, vol. 20, no. 2, pp. 343–353, 2005.
- [12] J. Kim, J. Choi, and H. Hong, “Output LC filter design of voltage source inverter considering the performance of controller,” in *International Conference on Power System Technology, PowerCon*, vol. 3. IEEE, 2000, pp. 1659–1664.
- [13] M. Lakka, E. Koutroulis, and A. Dollas, “Development of an FPGA-Based SPWM generator for high switching frequency DC/AC inverters,” *IEEE Transactions on Power Electronics*, vol. 29, no. 1, pp. 356–365, 2014.
- [14] B. Bourahla, B. Mazari, S. Moreau, and G. Champenois, “Sensorless AC current control with backstepping design for a PWM AC-DC converter,” in *International Conference on Renewable Energies and Power Quality (ICREPPQ)*, 2010.
- [15] Y. Suh and T. A. Lipo, “A control scheme of improved transient response for PWM AC/DC converter under generalized unbalanced operating conditions,” in *IEEE 35th Annual Power Electronics Specialists Conference, PESC 2004*, vol. 1. IEEE, 2004, pp. 189–195.
- [16] D. M. Mitchell, “AC-DC converter having an improved power factor,” Oct. 25 1983, US Patent 4,412,277.
- [17] N. Mohan and T. M. Undeland, *Power electronics: converters, applications, and design*. John Wiley & Sons, 2007.
- [18] Y. Hayashi, K. Takao, T. Shimizu, and H. Ohashi, “High power density design methodology,” in *Power Conversion Conference-Nagoya, PCC’07*. IEEE, 2007, pp. 569–574.

- [19] P. Friedrichs, "Silicon carbide power devices-status and upcoming challenges," in *2007 European Conference on Power Electronics and Applications*. IEEE, 2007, pp. 1–11.
- [20] A. Ong, J. Carr, J. Balda, and A. Mantooth, "A comparison of silicon and silicon carbide mosfet switching characteristics," in *Region 5 Technical Conference, 2007 IEEE*. IEEE, 2007, pp. 273–277.
- [21] J. Biela, M. Schweizer, S. Waffler, and J. W. Kolar, "SiC versus Si—evaluation of potentials for performance improvement of inverter and DC–DCy converter systems by SiC power semiconductors," *IEEE Transactions on Industrial Electronics*, vol. 58, no. 7, pp. 2872–2882, 2011.
- [22] K. Matocha, "Challenges in SiC power MOSFET design," *Solid-State Electronics*, vol. 52, no. 10, pp. 1631–1635, 2008.
- [23] B. Burger, D. Kranzer, and O. Stalter, "Cost reduction of PV-inverters with SiC-DMOSFETs," in *5th International Conference on Integrated Power Systems (CIPS)*. VDE, 2008, pp. 1–5.
- [24] S. Kaplan, T. Griffin, and S. Bayne, "Silicon vs silicon carbide device characterization," in *14th IEEE International Pulsed Power Conference, PPC-2003*, vol. 2. IEEE, 2003, pp. 1217–1220.
- [25] Y. Chang and J. Kuo, "SiC vs. Si: two-dimensional analysis of quasi-saturation behavior of DMOS devices operating at elevated temperatures," in *4th International Conference on Solid-State and Integrated Circuit Technology*. IEEE, 1995, pp. 298–300.
- [26] S. Dimitrijevic and P. Jamet, "Advances in SiC power MOSFET technology," *Microelectronics reliability*, vol. 43, no. 2, pp. 225–233, 2003.
- [27] M. Treu, R. Rupp, P. Blaschitz, K. Ruschenschmidt, T. Sekinger, P. Friedrichs, R. Elpelt, and D. Peters, "Strategic considerations for unipolar SiC switch options: JFET vs. MOSFET," in *Industry Applications Conference, 2007. 42nd IAS Annual Meeting. Conference Record of the 2007 IEEE*. IEEE, 2007, pp. 324–330.
- [28] A. M. Trzynadlowski, *Introduction to modern power electronics*. John Wiley & Sons, 2010.

- [29] P. Chlebis, P. Simonik, and M. Kabasta, "The comparison of direct and indirect matrix converters," in *Progress In Electromagnetic Research Symposium Proceedings, Cambridge, USA*, 2010, pp. 5–8.
- [30] M. Jussila, "Comparison of space-vector-modulated direct and indirect matrix converters in low-power applications," Ph.D. dissertation, Tampere University of Technology, 2007.
- [31] M. Venturini and A. Alesina, "The generalised transformer—a new bidirectional sinusoidal waveform frequency converter with continuously adjustable input power factor," in *PESC'80; Power Electronics Specialists Conference*, vol. 1, 1980, pp. 242–252.
- [32] X. Yu, C. Cecati, T. Dillon, and M. G. Simoes, "The new frontier of smart grids," *Industrial Electronics Magazine, IEEE*, vol. 5, no. 3, pp. 49–63, 2011.
- [33] T. Sumithira and A. N. Kumar, "An experimental investigation on off-grid solar photovoltaic power system using matrix converter," *Journal of Scientific & Industrial Research*, vol. 73, no. 2, pp. 124–128, 2014.
- [34] R. Cárdenas, R. Peña, G. Tobar, J. Clare, P. Wheeler, and G. Asher, "Stability analysis of a wind energy conversion system based on a doubly fed induction generator fed by a matrix converter," *IEEE Transactions on Industrial Electronics*, vol. 56, no. 10, pp. 4194–4206, 2009.
- [35] J. Rodriguez, M. Rivera, J. W. Kolar, and P. W. Wheeler, "A review of control and modulation methods for matrix converters," *IEEE Transactions on Industrial Electronics*, vol. 59, no. 1, pp. 58–70, 2012.
- [36] M. Imayavaramban, K. Latha, and G. Uma, "Analysis of different schemes of matrix converter with maximum voltage conversion ratio," in *Proceedings of the 12th IEEE Mediterranean Electrotechnical Conference, MELECON 2004*, vol. 3. IEEE, 2004, pp. 1137–1140.
- [37] P. W. Wheeler, J. Rodriguez, J. C. Clare, L. Empringham, and A. Weinstein, "Matrix converters: a technology review," *IEEE Transactions on Industrial Electronics*, vol. 49, no. 2, pp. 276–288, 2002.

- [38] L. Empringham, L. de Lillo, and M. Schulz, "Design challenges in the use of silicon carbide JFETs in matrix converter applications," *IEEE Transactions on Power Electronics*, vol. 29, no. 5, pp. 2563–2573, 2014.
- [39] S. Nagai, Y. Yamada, N. Negoro, H. Handa, Y. Kudoh, H. Ueno, M. Ishida, N. Otuska, and D. Ueda, "30.5 a GaN 3×3 matrix converter chipset with drive-by-microwave technologies," in *2014 IEEE International Solid-State Circuits Conference Digest of Technical Papers (ISSCC)*. IEEE, 2014, pp. 494–495.
- [40] D. Campbell, "Nonlinear science: From paradigms to practicalities," *Los Alamos Science*, vol. 15, no. Special Issue, pp. 218–262, 1987.
- [41] M. A. Trump, "What is chaos," *Ilya Prigogine Center for Studies in Statistical Mechanics and Complex Systems, Univ. of Texas, Austin*, 1998.
- [42] J. H. Deane, "Modeling the dynamics of nonlinear inductor circuits," *IEEE Transactions on Magnetics*, vol. 30, no. 5, pp. 2795–2801, 1994.
- [43] J. R. Wood, "Chaos: a real phenomenon in power electronics," in *4th Annual IEEE Applied Power Electronics Conference and Exposition, APEC'89*. IEEE, 1989, pp. 115–124.
- [44] P. S. Linsay, "Period doubling and chaotic behavior in a driven anharmonic oscillator," *Physical Review Letters*, vol. 47, no. 19, p. 1349, 1981.
- [45] D. C. Hamill and D. J. Jeffries, "Subharmonics and chaos in a controlled switched-mode power converter," *IEEE Transactions on Circuits and Systems*, vol. 35, no. 8, pp. 1059–1061, 1988.
- [46] J. H. Deane and D. C. Hamill, "Analysis, simulation and experimental study of chaos in the buck converter," in *IEEE Power Electronics Specialists Conference*, vol. 2, 1990, pp. 491–498.
- [47] C. Tse, Y. Zhou, F. Lau, and S. Qiu, "Intermittent chaos in switching power supplies due to unintended coupling of spurious signals," in *2003 IEEE 34th Annual Power Electronics Specialist Conference, PESC '03*, vol. 2, 2003, pp. 642–647 vol.2.

- [48] K. Chakrabarty, G. Poddar, and S. Banerjee, "Bifurcation behaviour of the buck converter," *IEEE Transactions on Power Electronics*, vol. 11, no. 3, pp. 439–447, 1996.
- [49] L. O. Chua, *The genesis of Chua's circuit*. Electronics Research Laboratory, College of Engineering, University of California, 1992.
- [50] L. Chua, "Chua's circuit 10 years later," *International Journal of Circuit Theory and Applications*, vol. 22, no. 4, pp. 279–305, 1994.
- [51] Z. Qu, G. Hu, G. Yang, and G. Qin, "Phase effect in taming nonautonomous chaos by weak harmonic perturbations," *Physical review letters*, vol. 74, no. 10, p. 1736, 1995.
- [52] G. Uicich, S. Maestri, M. Benedetti, and D. Carrica, "A nonlinear approach for assessing stability in line-commutated converters with an integrating controller," *IEEE Transactions on Power Electronics*, vol. 29, no. 1, pp. 339–346, 2014.
- [53] H. Chiang, C. Liu, P. P. Varaiya, F. F. Wu, M. G. Lauby, and C. KIENY, "Chaos in a simple power system. discussion," *IEEE Transactions on Power Systems*, vol. 8, no. 4, pp. 1407–1417, 1993.
- [54] D. C. Hamill, "Power electronics: A field rich in nonlinear dynamics," in *Proc. 3rd Int. Specialists Workshop on Nonlinear Dynamics of Electronic Systems NDES' 95*. Citeseer, 1995.
- [55] H. S. Patel and R. G. Hoft, "Generalized techniques of harmonic elimination and voltage control in thyristor inverters: Part I—Harmonic elimination," *IEEE Transactions on Industry Applications*, no. 3, pp. 310–317, 1973.
- [56] Patel, Hasmukh S and Hoft, Richard G, "Generalized techniques of harmonic elimination and voltage control in thyristor inverters: Part II—Voltage control techniques," *IEEE Transactions on Industry Applications*, no. 5, pp. 666–673, 1974.
- [57] G.-H. Choe, A. K. Wallace, and M.-H. Park, "An improved pwm technique for AC choppers," *IEEE Transactions on Power Electronics*, vol. 4, no. 4, pp. 496–505, 1989.

- [58] K. E. Addoweesh and A. L. Mohamadein, "Microprocessor based harmonic elimination in chopper type AC voltage regulators," *IEEE Transactions on Power Electronics*, vol. 5, no. 2, pp. 191–200, 1990.
- [59] J. M. Rivas, D. Jackson, O. Leitermann, A. D. Sagneri, Y. Han, and D. J. Perreault, "Design considerations for very high frequency dc-dc converters," in *37th IEEE Power Electronics Specialists Conference, PESC'06*. IEEE, 2006, pp. 1–11.
- [60] H. Wang, F. Wang, and J. Zhang, "Power semiconductor device figure of merit for high-power-density converter design applications," *IEEE Transactions on Electron Devices*, vol. 55, no. 1, pp. 466–470, 2008.
- [61] J. W. Kolar, T. Friedli, J. Rodriguez, and P. W. Wheeler, "Review of three-phase pwm AC–AC converter topologies," *IEEE Transactions on Industrial Electronics*, vol. 58, no. 11, pp. 4988–5006, 2011.
- [62] I. Flegar, D. Pelin, and D. Zazeck, "Bifurcation diagrams of the buck converter," in *9th International Conference on Electronics, Circuits and Systems*, vol. 3. IEEE, 2002, pp. 975–978.
- [63] Z. Liu, A. Abou-Alfotouh, and M. Wilkowski, "Nonlinear inductor modeling for power converter," in *2012 27th Annual IEEE Applied Power Electronics Conference and Exposition (APEC)*. IEEE, 2012, pp. 1868–1871.
- [64] D. C. Hamill, J. H. Deane, and P. J. Aston, "Some applications of chaos in power converters," in *IEE Colloquium on Update on New Power Electronic Techniques (Digest No: 1997/091)*. IET, 1997, pp. 5–1.
- [65] G. Mazzini, R. Rovatti, and G. Setti, "Chaos-based asynchronous ds-cdma systems and enhanced rake receivers: Measuring the improvements," *IEEE Transactions on Circuits and Systems I: Fundamental Theory and Applications*, vol. 48, no. 12, pp. 1445–1453, 2001.
- [66] Z. Suto, I. Nagy, and E. Masada, "Avoiding chaotic processes in current control of AC drive," in *29th Annual IEEE Power Electronics Specialists Conference, PESC 98 Record*. IEEE, 1998, pp. 255–261.

- [67] T. Takuno, Y. Kitamori, R. Takahashi, and T. Hikihara, "AC power routing system in home based on demand and supply utilizing distributed power sources," *Energies*, vol. 4, no. 5, pp. 717–726, 2011.
- [68] S. M. Amin and B. F. Wollenberg, "Toward a smart grid: power delivery for the 21st century," *Power and Energy Magazine, IEEE*, vol. 3, no. 5, pp. 34–41, 2005.
- [69] R. Takahashi, Y. Kitamori, and T. Hikihara, "AC power local network with multiple power routers," *Energies*, vol. 6, no. 12, pp. 6293–6303, 2013.
- [70] T. Takuno, M. Koyama, and T. Hikihara, "In-home power distribution systems by circuit switching and power packet dispatching," in *2010 1st IEEE International Conference on Smart Grid Communications (SmartGridComm)*. IEEE, 2010, pp. 427–430.
- [71] K. Tashiro, R. Takahashi, and T. Hikihara, "Feasibility of power packet dispatching at in-home dc distribution network," in *2012 3rd IEEE International Conference on Smart Grid Communications (SmartGridComm)*. IEEE, 2012, pp. 401–405.
- [72] M. M. He, E. M. Reutzel, X. Jiang, R. H. Katz, S. R. Sanders, D. E. Culler, and K. Lutz, "An architecture for local energy generation, distribution, and sharing," in *Energy 2030 Conference, 2008*. IEEE, 2008, pp. 1–6.
- [73] G. Lu, D. De, and W.-Z. Song, "Smartgridlab: A laboratory-based smart grid testbed," in *2010 1st IEEE International Conference on Smart Grid Communications (SmartGridComm)*. IEEE, 2010, pp. 143–148.
- [74] H. Iman-Eini, J. Schanen, S. Farhangi, J. Barbaroux, and J. Keradec, "A power electronic based transformer for feeding sensitive loads," in *Power Electronics Specialists Conference, 2008. PESC 2008. IEEE*. IEEE, 2008, pp. 2549–2555.
- [75] K. Basu, R. K. Gupta, S. Nath, G. F. Castelino, K. K. Mohapatra, and N. Mohan, "Research in matrix-converter based three-phase power-electronic transformers," in *2010 International Power Electronics Conference (IPEC)*. IEEE, 2010, pp. 2799–2803.

- [76] M. D. Manjrekar, R. Kieferndorf, and G. Venkataramanan, "Power electronic transformers for utility applications," in *Industry Applications Conference, 2000. Conference Record of the 2000 IEEE*, vol. 4. IEEE, 2000, pp. 2496–2502.
- [77] E. R. Ronan, S. D. Sudhoff, S. F. Glover, and D. L. Galloway, "A power electronic-based distribution transformer," *IEEE Transactions on Power Delivery*, vol. 17, no. 2, pp. 537–543, 2002.
- [78] J. K. Shah, "Dynamic power flow control for a smart micro-grid by a power electronic transformer," Ph.D. dissertation, UNIVERSITY OF MINNESOTA, May 2011.
- [79] S. Zeng, B. Zhang, D. Qiu, and H. Ma, "Four-step switching strategy for bidirectional switches in single-phase AC/AC buck converter," in *2nd IEEE Conference on Industrial Electronics and Applications, ICIEA 2007*. IEEE, 2007, pp. 1692–1695.
- [80] D. Moongilan, "Radiated emissions from proximity coupled oversized heat-sinks," in *IEEE International Symposium on Electromagnetic Compatibility, EMC 2007*. IEEE, 2007, pp. 1–6.
- [81] W. Khamsen, A. Aurasopon, W. Sa-ngiamvibool, and S. Kaittisin, "Designing parameters in pwm buck AC chopper for unity input power factor," *Electrical Engineering*, 2011.
- [82] A. Aurasopon and N. Piladaeng, "Unity input power factor for a PWM boost AC chopper," *Journal of Electrical Engineering: Theory and Application*, vol. 1, no. 3, pp. 135–140, 2010.
- [83] H. Haruta, *The Impedance Measurement Handbook: A Guide to Measurement Technology and Techniques*. Agilent Technologies, 2000.
- [84] M. Huasheng, Z. Liang, Z. Bo, and Z. Jianchao, "AC/AC buck converter instantaneous value control modeling, system analyzing and designing," in *Proceedings of the 8th International Conference on Electrical Machines and Systems, ICEMS 2005*, vol. 2. IEEE, 2005, pp. 1391–1395.
- [85] R. M. May *et al.*, "Simple mathematical models with very complicated dynamics," *Nature*, vol. 261, no. 5560, pp. 459–467, 1976.

- [86] Z. T. Zhusubaliyev, E. Mosekilde, A. I. Andriyanov, and G. Y. Mikhal'chenko, "High-feedback operation of power electronic converters," *Electronics*, vol. 2, no. 2, pp. 113–167, 2013.
- [87] C. K. Tse, *Complex behavior of switching power converters*. CRC press, 2003.
- [88] M. T. Rosenstein, J. J. Collins, and C. J. De Luca, "A practical method for calculating largest Lyapunov exponents from small data sets," *Physica D: Nonlinear Phenomena*, vol. 65, no. 1, pp. 117–134, 1993.
- [89] R. Hegger, H. Kantz, and T. Schreiber, "Practical implementation of nonlinear time series methods: The TISEAN package," *Chaos: An Interdisciplinary Journal of Nonlinear Science*, vol. 9, no. 2, pp. 413–435, 1999.
- [90] T. M. Blooming and D. J. Carnovale, "Application of IEEE STD 519-1992 harmonic limits," in *Conference Record of Annual Pulp and Paper Industry*. IEEE, 2006, pp. 1–9.
- [91] C. Xia, P. Song, T. Shi, and Y. Yan, "Chaotic dynamics characteristic analysis for matrix converter," *IEEE Transactions on Industrial Electronics*, vol. 60, no. 1, pp. 78–87, 2013.
- [92] S. M. Cox and J. C. Clare, "Nonlinear development of matrix-converter instabilities," *Journal of Engineering Mathematics*, vol. 67, no. 3, pp. 241–259, 2010.
- [93] D. Casadei, G. Serra, A. Tani, and L. Zarri, "Matrix converter modulation strategies: a new general approach based on space-vector representation of the switch state," *IEEE Transactions on Industrial Electronics*, vol. 49, no. 2, pp. 370–381, 2002.
- [94] M. Apap, J. Clare, P. Wheeler, and K. Bradley, "Analysis and comparison of AC-AC matrix converter control strategies," in *2003 IEEE 34th Annual Power Electronics Specialist Conference, PESC'03*, vol. 3. IEEE, 2003, pp. 1287–1292.
- [95] P. Szczesniak, *Three-Phase AC-AC Power Converters Based on Matrix Converter Topology*. Springer, 2013.

- [96] S. Barakati, M. Kazerani, and J. Aplevich, "An overall dynamic model for a matrix converter," in *IEEE International Symposium on Industrial Electronics, ISIE 2008*. IEEE, 2008, pp. 13–18.
- [97] F. Gao and M. R. Iravani, "Dynamic model of a space vector modulated matrix converter," *IEEE Transactions on Power Delivery*, vol. 22, no. 3, pp. 1696–1705, 2007.
- [98] H. Nikkhajoei, A. Tabesh, and R. Iravani, "Dynamic model of a matrix converter for controller design and system studies," *IEEE Transactions on Power Delivery*, vol. 21, no. 2, pp. 744–754, 2006.
- [99] J. Lamoree, D. Mueller, P. Vinett, W. Jones, and M. Samotyj, "Voltage sag analysis case studies," *IEEE Transactions on Industry Applications*, vol. 30, no. 4, pp. 1083–1089, 1994.
- [100] B. Ozpineci and L. Tolbert, *Comparison of wide-bandgap semiconductors for power electronics applications*. United States. Department of Energy, 2004.
- [101] M. Minami, "Studies on passivity-based control and phase synchronization in linkage of distributed generation to power system network (in Japanese)," Ph.D. dissertation, Kyoto University, 2013.